On the Attitude Control by Thruster of a Spinning Solar Sail and Bending Moment's Effect Analysis

Aerospace Technology Engineering

Engineering Physics

Roger Bertran Rabat

Osamu Mori
Kawaguchi Jun'ichiro
Jose Francisco Trull Silvestre

May 12, 2019

Abstract

The membrane dynamics of spinning solar sails have a special relevance when considering attitude control of the spacecraft. Because of being non-rigid structures, local deformation occurs, changing the overall effect of the Solar Radiation Pressure, which might lead to attitude disturbances and unexpected behavior. Thus, an accurate model and study of such dynamics is needed. Until this point, several researches on the topic have been conducted, modelling the membrane as a completely flexible body. However, the deformation observed in IKAROS (a spacecraft developed by the Japan Aerospace Exploration Agency (JAXA) to demonstrate solar sail technology) during its low-spin operation suggested a higher rigidity of the sail than the predicted one. The difference between the observed and the predicted deformation of IKAROS is believed to be caused by the bending stiffness present in the membrane.

First, this study shows that the bending moment has strong effects on the attitude of the sail during its spin axis reorientation. Given the difficulty of measuring the actual bending stiffness of the membrane, it is necessary to find a control system capable to perform the same regardless of its value. Therefore, this paper also presents a new control system and its corresponding logic to lower the influence of the bending parameter on this attitude maneuver performance. The sail dynamics are simulated via an adjusted membrane model implemented through the Multi Particle Method, and the characteristics of the sail are those for the OKEANOS mission, JAXA.

This newly proposed system consists on placing reaction devices in the tip-masses present in the vertexes of the sail instead of in the main body of the spacecraft. This also allows limiting the effect of the coupled dynamics between the hub and the sail, and grants a major control over the vibrations since it acts directly over the membrane. The advantages of this control system with respect to the conventional in-body one are discussed through simulations. Finally, a frequency analysis on the vibrations arising in the membrane for both presented methods when considering different bending stiffness values is done. This last analysis shows the shift in the natural frequencies obtained when compared with the non-bending analyses until the date, remarking the importance of the bending stiffness when considering the dynamics of a mast-free sail.

Keywords: Solar Sail; Attitude Control; Bending Stiffness; Flexible Structure; Multi Particle Model; Vibration Mode

Acknowledgements

First of all, I would like to thank the CFIS (Interdisciplinary Higher Education Centre) for all the opportunities given along the five years of Bachelor, as well as for their financial support, without which this thesis would have never been written. Also, I would like to specially extend the thanks to the Director, Professor Miguel Ángel Barja, and the Academic and Mobility Deputy Directors, Professors Marta València and Antonio Pascual, as well as the secretary staff Noemí Dengra and Asunción Tur.

I also owe a debt to JAXA (Japan Aerospace Exploration Agency), for letting me develop the thesis in one of its centers. I particularly want to thank my supervisor, Professor Osamu Mori-sensei, for his guidance and scientific support through all the project. Also, I am indebted to Professor Kawaguchi-sensei for accepting me into his laboratory as well as providing advice on the thesis. I want to thank also Okabe-san and Fukazawa-san for their help during the internship months, as well for the hard bureaucratic work before I came.

I thank my supervisor from the UPC (Barcelona Tech), Professor Jose Francisco Trull, for his follow up on my thesis, as well as for introducing me to solar sailing in the first place and providing me with literature on the topic.

Also, I want to thank Takao-san, Ishida-san, and Kato-san for their advice and suggestions on my research, and for the patience they had with me. Together with the other members of the Kawaguchi Laboratory, I want to thank them all for giving me such a warm welcome and accepting me as one more of them. They made my stay a ton of fun.

Last but, by no means, least, I want to thank my family and friends in Spain for their moral and unconditional support. My parents, Jordi Bertran and Lourdes Rabat, sisters, Thaís and Alexandra Bertran, and grandparents, Jaume Bertran, Nuri Padrós, Rossendo Rabat and Rosa Sabater, deserve a special mention. Their support and their love even when being apart have pushed me forward since as long as I can remember, and have been the back-bone of my successes.

Contents

List of Figures

1   Introduction

1.1   Background

No propellant, just a sail to navigate in a sea of stars, on the wings of solar radiation pressure. As romantic as it may sound, this is the concept behind solar sailing.

Solar sails take advantage of the photons' momenta to be driven by solar radiation pressure (SRP). As a means of fuel-free propulsion, these spacecrafts are actively studied at several institutes around the world. In addition to not requiring any propellant, they also offer other major advantages characteristic of deployable membrane structures, such as their light weight and small stowed volume. That, together with their large area, allow for high launching and transportation efficiency.

Solar sails can be classified accordingly to their deployment method, that can be either mast-extension type or spinning solar sails, which deploy the membrane using centrifugal force. Among these two, the Institute of Space and Astronautical Science (ISAS), Japan Aerospace Exploration Agency (JAXA), is studying the last type which, because of not requiring any supporting structure, is lighter than the former.

JAXA does not only focus on solar sails but also on Solar Power Sails. A Solar Power Sail is a Japanese original concept that gets electricity from thin film solar cells on the membrane in addition to the acceleration by solar radiation. A Solar Power Sail craft can save fuel by using a solar sail at the same time as gaining electric power by using a vast area of thin film solar sails on the membrane even when being far away from the Sun. This technology was demonstrated for the first time in space during the IKAROS mission.

1.1.1   IKAROS

IKAROS (Interplanetary Kite-craft Accelerated by Radiation Of the Sun), launched by JAXA in 2010, was the world's first successful Solar Sail mission. This mission was performed as a precursor for technology verification towards the Solar Power Sail mission to the Trojan Asteroids, that is, the OKEANOS mission.
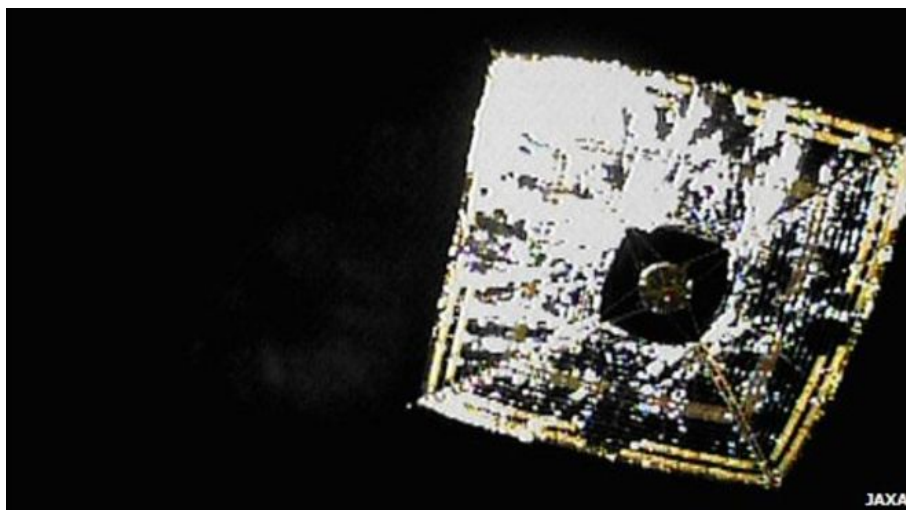
Figure 1: IKAROS, photographed by a deployable camera.

The four key technologies demonstrated by IKAROS during its operation are listed as it follows:

- Deployment and span of a 20 meters in diameter membrane by centrifugal force

- Power generation and current collection by thin-film solar cells

- Demonstration of photon propulsion and orbit control by SRP

- Acquisition of navigation technology for solar sails

According to JAXA, IKAROS finished all planned experiments in December 2010, but the mission continued beyond that date in order to enhance solar sail control. On 30 November 2012, JAXA announced that IKAROS had been recognized by Guinness World Records as the world's first solar sail spacecraft between planets.

1.1.2   OKEANOS: Mission Overview

The mission at JAXA following IKAROS is OKEANOS (Outsized Kite-craft for Exploration and Astro-Nautics in the Outer Solar system) [1], a landing and sample return of Jupiter Trojan asteroids using a solar power sail-craft. The mission has as its main objective a rendezvous and a posterior lander deployment on one of the Jupiter Trojan asteroids. Little is known about their origin and their evolution, as the observations provide limited clues about the source of these asteroids. Currently, these asteroids are completely unexplored, and the study of its composition is expected to enlighten the present understanding of the formation and evolution of the Solar System, since Trojans are the missing link between asteroids and comets. Also, this mission aims to provide several new innovative first-class astronomical science observations during the deep space cruising phase.
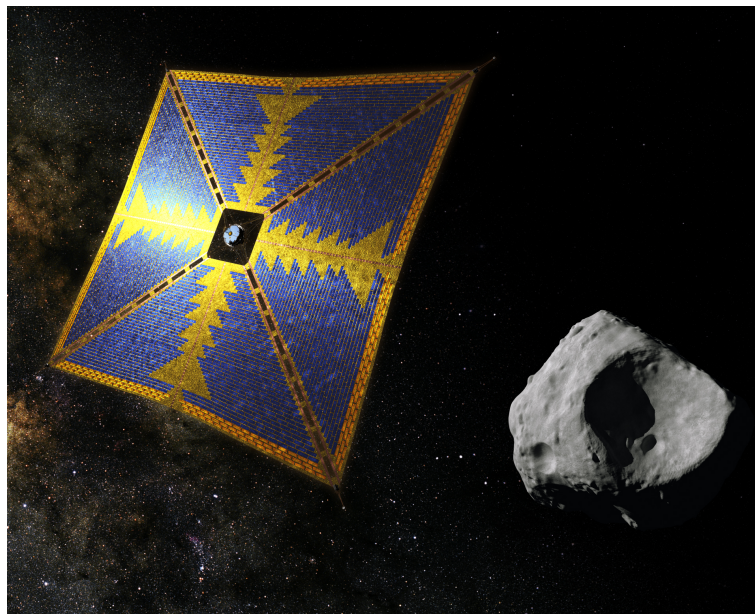
Figure 2: A computer rendering showing what JAXA's solar sail may look like as it approaches the Trojan asteroid.

A space mission to Trojan asteroids faces the challenge of reaching the unexplored far side of our solar system, where large amount of fuel is required and an efficient power supply is difficult. Therefore, JAXA concluded that the solar power sail is the best way to perform such a challenging mission.

The next solar power sail to be used has a large membrane surface of 2000 m^2, 10 time larger than that of IKAROS [2], and has thin film solar cells attached to most of it. The thin film solar cells are a ultra-light power generation system (1 kW/kg) and are able to generate large electric power in the outer planetary region (5 kW at 5.2 AU). Also, the hub is provided with a ion engine, which was demonstrated during the Hayabusa mission, capable of getting a large ΔV in the outer planetary region.

The mission sequence is as presented in Figure 3:
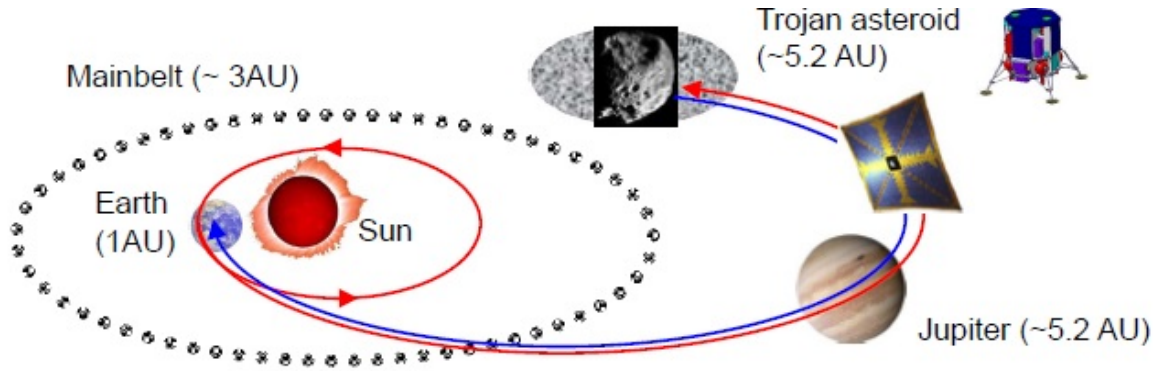
Figure 3: OKEANOS' mission sequence.

The solar power sail-craft is supposed to rendezvous with the Trojan asteroid after using both Earth and Jupiter gravity assists. After arriving at the Trojan asteroid, the lander is separated from sail-craft to collect surface and subsurface samples and perform in-situ analysis. Up until this point, it would be possible to either end the mission or continue with the sample return operation. If the latter is chosen, the lander will deliver the samples to the sail-craft and the solar power sail will return to Earth after a Jupiter swing-by.

1.2   Motivation and Purpose of the Research

Prior to the release of the lander, the solar sailing spacecraft is to hover over the asteroid at an altitude of 40 km, and then descend to 1 m so as to make effective the rendezvous. For both close and far operation cases, attitude control is vital to counteract the perturbations that may appear in the chosen orbits, due to, for instance, the irregular shape of it.

Such attitude control will be studied by thruster application. Control by means of an input in the membrane has already been studied in [3] by means of Reflectivity Control Devices (RCD). In our present case of study, considering the dimensions of OKEANOS' sail and that its operation takes place in a low solar radiation pressure environment, thrusting has been chosen above the former control. Despite thrusters not being fuel-free, they provide a control with the possibility of a much faster response of the system, as well as a higher reliability, as RCD were found to have a short life period in outer space during IKAROS' demonstration.

During IKAROS' operation, the membrane deformation and spacecraft attitude was observed to differ from the simulated one. Such difference is believed to be caused by the bending stiffness present in the membrane, that has been often overlooked in the literature [4]-[5]. Considering the importance of membrane dynamics and deformation when considering attitude control in a flexible body, a model including such rigidity has to be used. Besides, OKEANOS has more elements than IKAROS on its membrane. Therefore, it is expected to have an increased rigidity, so further study on the bending dynamics of the sail is required for the better implementation of attitude-orbit control. Thus, in this document an accurate study of the sail dynamics will be done during the reorientation maneuver, putting special attention on the effects of the bending moment over the motion of the sail. Also, a frequency analysis on the out-of-plane motion of the particles of the sail will also be performed.

Finally, since the bending moment is a non measurable parameter of the membrane that plays an important role on its dynamics, a control method such that the motion of the sail does not get affected up to a great measure by the bending stiffness needs to, and will, be proposed.

3

1.3 Outline of the Thesis

Section 2 consists on explaining the model used to simulate the sail's dynamics numerically, the Multi-Particle Model. First of all, the components of the spin-type solar sail to be modeled are introduced. Then, the construction of the analytical model via Multi-Particle Method is explained thoroughly, deriving the calculation of the parameters and equations that determine the dynamics of the system.

In Section 3, the parameters for the evaluation of the attitude motion are presented, that is, the Euler angles roll, pitch and yaw, as well as the Direction Cosine Matrix linking both the inertial and spacecraft reference frames. Then, the spin-axis reorientation system present in OKEANOS is introduced, and the precession angle is obtained from the change in the angular momentum vector. Also, the Rhumb-Line algorithm used during the axis-reorientation maneuver is described in this section.

Section 4 comprises the first results obtained from the simulations. First, the attitude angles of the sail are shown, with the corresponding discussion on the effects of the bending stiffness. An analysis in the frequency domain for the out-of-plane motion of the particles of the sail follows.

In Section 5, a new attitude control system is proposed over the one in the previous section. Following the same outline as Section 4, an attitude analysis followed by the frequency one are presented. A comparison with the anterior control system is also done.

Section 6 has the same structure as the last two in terms of simulations and analysis, but before that a new control algorithm is introduced. In the end of the section, the results obtained are also compared with the others.

Finally, Section 7 states the conclusions obtained along the rest of the sections of the document.

2 Modelling

The behaviour of the membrane surface is strongly affected by slight forces, so when carrying on in ground experiments it is necessary to have a microgravity and vacuum environment, so as to avoid both gravity and air drag [6]-[7]. However, when the size of the membrane is that of several tens of meters, such experiments become very difficult. Besides, the use of a scaled model leads to important errors, because the thickness of the membrane cannot be reduced even though the span of the membrane is. That causes the influence of the bending rigidity of the small prototype to be far stronger than the real one, limiting the accuracy of the predicted behaviour obtained during such experiments.

Therefore, the study of the dynamics by means of a numerical analysis is needed in advanced design stages. Several numerical models have been proposed for dynamic analysis on flexible structures such as membranes [8], but the formation of wrinkles and the low compression rigidity cause a poor convergence and low numerical stability. In [9], numerically stable analysis codes based on the energy-momentum method are proposed, but the calculation cost remains high for dynamic analysis.

The use of Finite Element Method (FEM) has been proven useful for analysing the dynamics of a spinning solar sail [10]. Nonetheless, it takes a very long time to achieve accurate results about the attitude motion of the solar sail if many parameters are varied. Instead, Multi-Particle Model (MPM) is the numerical method used for this study. The Multi Particle Model consists on substituting the elements of the membrane by particles connected by springs and dampers. Compared with FEM, the Multi Particle Model offers a simplified construction and a lower computational cost, as shown conceptually in Figure 4. Despite the consequent accuracy reduction, the precision of the model is enough for the study of the dynamics described in this document. The Multi-Particle Model has been validated via numerous vibration experiments in vacuum chambers [13]-[15].
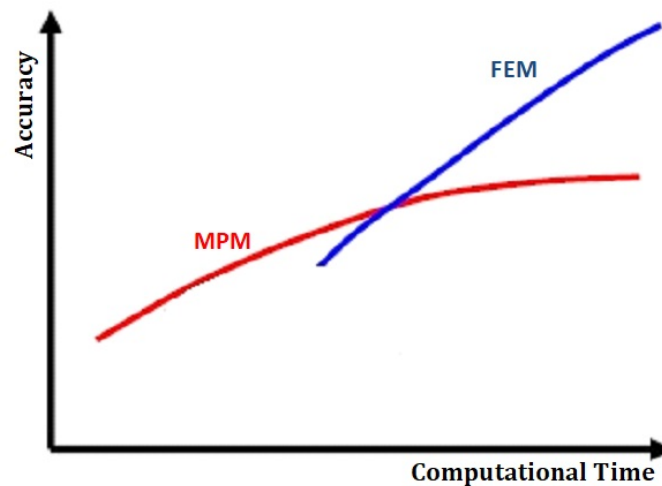
Figure 4: Conceptual diagram of the relationship between computational time and accuracy between both numerical methods.

In this approach, as it will be described in a deeper way later, the mass of each particle is determined based on the membrane configuration, and the spring constants are determined by applying the principle of virtual work on an element [11].

2.1 Target of Analysis

As mentioned before, the object of analysis in this study is a spinning solar sail. This research focuses on the third stage of the solar sail's operation, when the sail is completely deployed.

2.1.1 Components of the Sail

A spinning solar sail consists of the main body of the spacecraft, the membrane and the devices attached on it, and the tip mass; all of the elements being connected by tethers. A schematic diagram of the sail and its components is presented in Figure 5:
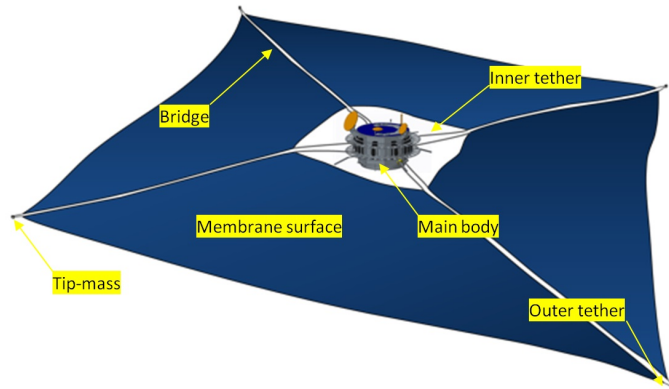
Figure 5: Schematic diagram of the components present in a spinning solar sail.

2.1.1.1 Main body

Regarded as a cylindrical rigid body. It is connected by tethers to the membrane of the sail and receives forces and torque based on both the tension on them or the contact with the membrane. During a spin-axis reorientation maneuver by in-body thrusters, receives the external force directly from the reaction devices.

2.1.1.2 Membrane surface

Divided into four trapezoidal sections called petals, it is composed by ultra-thin polyimide film. Attached to the membrane several devices can be found, such as reinforcing tape, dust counters, thin-film solar cells and reflectivity control devices (RCD), each of them affecting the thickness of the membrane. The four petals are connected by bridges, consisting on spaced membrane film sections along the hypotenuse of the petals. The membrane and its components can be seen in detail in Figure 6:
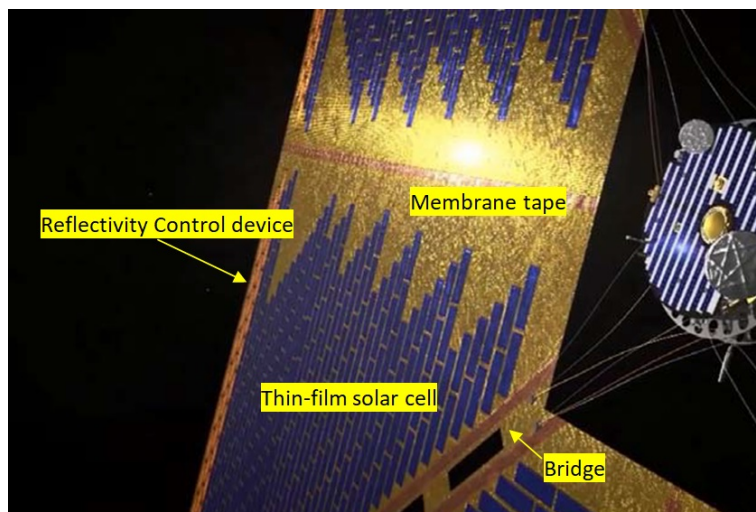
Figure 6: Close view on the surface of the membrane of the sail.

2.1.1.3 Tip mass

Weights attached to the tip of the membrane of the sail by tethers. They play a main role during the deployment of the sail, as they provide the necessary centrifugal force for that to happen. During the third stage on the solar sail's operation, their role is as important, as the centrifugal force is still needed to keep the surface of the membrane stretched.

2.1.1.4 Tether

Inner tethers and outer ones can be distinguished. The former are the connection between the membrane of the sail and the main body, each petal having four of them as it can also be seen in Figure 6. They transmit the force and torque between the main body and the membrane, as well as helping on the dissipation of the vibrations of the film. Outer tethers connect each tip mass with its two respective petals, having two tethers per mass.

2.2 Multi-Particle Model[1]

As mentioned before, the model for the numerical analysis of the sail dynamics that is used in this report is the Multi-Particle Model, as developed by Y. Shirazawa in [12]. Its formulation has been included in the research because of its relevance in the simulations done. In the present study, however, small modifications have been included to readjust the effect of the bending moment, for the first time to be applied in the second stage of the sail's operation.

2.2.1 Membrane surface model

The surface of the membrane, as presented in Figure 7, is modelled by a spring-mass-damper system, with each petal connected to the adjacent ones by means of springs, corresponding to the bridges.
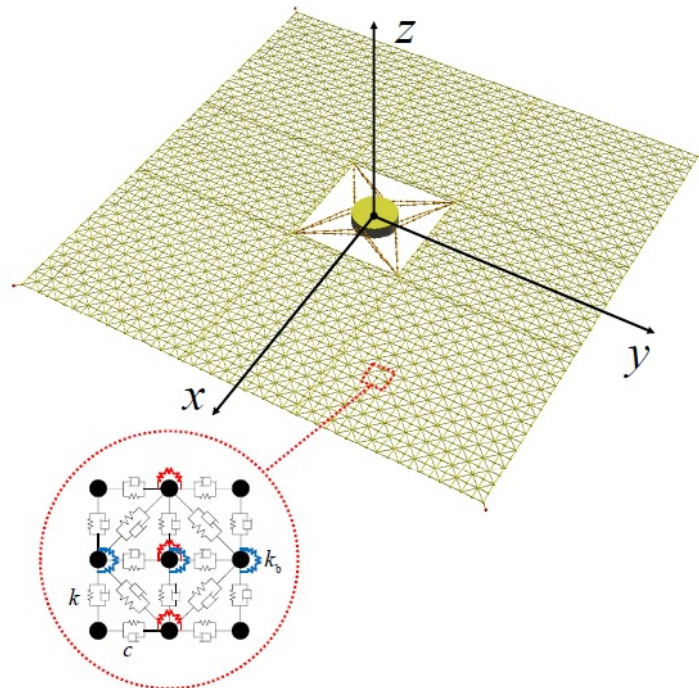
Figure 7: Layout of membrane simulation for Multi Particle Model.

Springs placed on the surface have can act on both compression and elongation regimes, both simulating the tensile and compressive rigidity of the membrane. For each case, the physical properties

---

[1]Developed by Shirazawa, 2015

of the spring are considered to vary. Bending stiffness and contact within the membrane are simulated by means of torsion springs, as it will be explained thoroughly later on in this section.

The hub of the spacecraft is considered to be a cylindrical rigid body, connected to the membrane surface by a spring-mass distribution representing the inner tether system.

The tip masses are treated as point masses that are attached to the membrane by springs, that take the place of the outer tethers.

2.2.1.1 Placement of membrane elements

The arrangement of mass points on the membrane surface is such so the folded shape before deployment can be also simulated. The heigh of each trapezoid that constitutes a petal is divided into elements according to the number of folds. The width between particles in the parallel direction to the base of the petal differs. The particles presented in the green area in Figure 8 present the same spacing in both x and y directions. For the yellow area, however, as its particles are to be wrapped directly in contact with the main probe before the expansion, has its width determined. The spacing between particles in the aforementioned area is done so as the shape of each element is as close as a square as possible. As shown in Figure 7, each quadrilateral element is further divided into two triangles by means of the spring connecting the diagonally opposed particles.
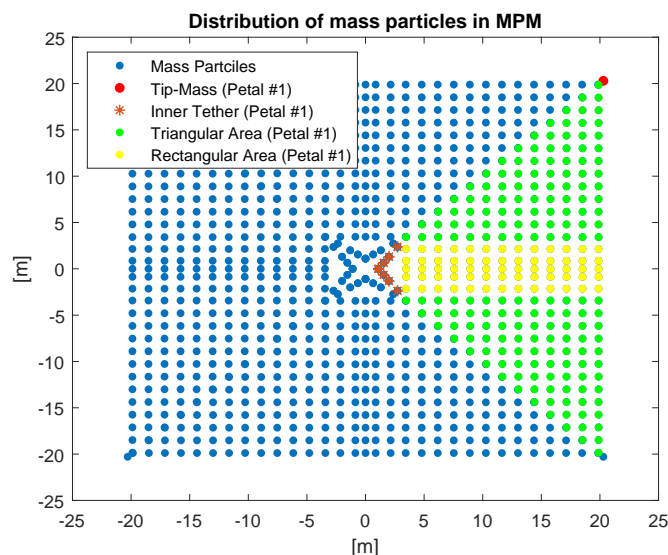
Figure 8: Mass point distribution for Multi-Particle Model.

As said before, each mass point has a value such that the mass distribution reflects the actual surface design of the membrane.

The same way as it happens with the surface particles, the inner tether is also divided so its shape can be expressed before the secondary stage of the operation. Therefore, the part wrapped around the probe is divided in the very same way as the innermost yellow area of Figure 8.

In the simulations done, the number of folds before expansion, which determines the number of elements, has been chosen equal to 12, in consonance with the stipulated number for the OKEANOS mission. The total number of surfaces, particles and springs is shown in Table 1.

Table 1: Number of elements per petal for 12 folds division

Surfaces	432
Mass points	
Membrane surface	247
Tip Mass	1
Inner Tether (2)	8 (2)
Tension/compression Springs	
Membrane surface	708
Outer Tether	1
Inner Tether (2)	8 (2)
Torsion Springs	782

2.2.2 Derivation of the spring constant

In the Multi-Particle Model, the spring constants permit to express the tensile stress of the membrane, and are obtained as presented below [16], through the principle of virtual work.

The shear modulus G is expressed as it follows:

$$G = \frac{E}{2(1 + \nu)} \tag{1}$$

where E is the Young's modulus of the membrane and ν is the Poisson's ratio. So as for Equation 1 to hold when dealing with rectangular elements with a spring in the diagonal, the Poisson's ratio should be close to $1/3$, which is the value that will be considered in this research.

Despite as what can be observed in Figure 7, where it displays a mesh out of triangular elements, the derivation of the spring constant will be done for parallelogram elements as in Figure 9
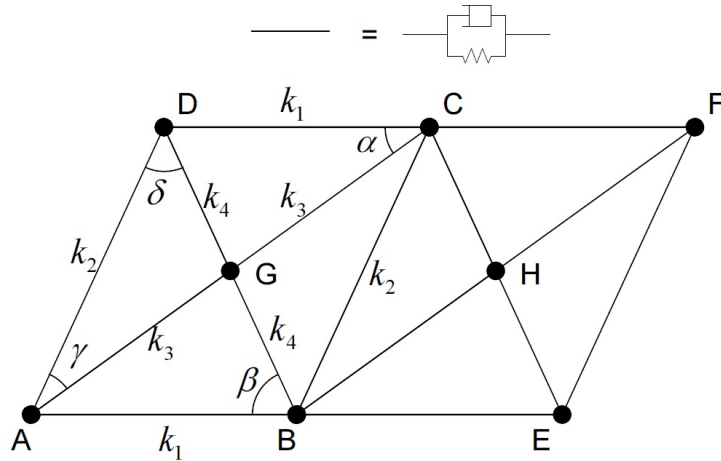
Figure 9: Parallelogram element.

As shown in the diagram, the unknowns are the spring constants connecting the masses of the elements, for which symmetry has been considered throughout the element. In order to obtain the spring constants, the relationship between elastic and strain energy will be used.

To apply the principle of virtual work, let's consider first a force F acting in the $\overline{AB}$ direction. In consequence, as shown in the left hand side of Figure 10, B and C masses are displaced up to B' and C', and the lower side of the parallelogram is elongated by a distance u. Therefore, the elastic energy of

k_1 on the element k is expressed like:

$$U_{k\overline{AB}} = \frac{1}{2}\left(\frac{k_1}{2}\right)u^2 \tag{2}$$

As the side $\overline{AB}$ is shared between two elements, the spring constant has been set to be $\frac{k_1}{2}$.

The elastic energy corresponding to the $\overline{DC}$ side is expressed by using the same Equation 2 because of symmetry considerations on the spring constants, as mentioned above.

Considering the displacement u small enough compared to the length of $\overline{AB}$, the elongation of the springs $\overline{AC}$ and $\overline{DB}$ can be expressed as:

$$u_{\overline{AC}} = u\,cos\alpha \tag{3}$$
$$u_{\overline{DB}} = u\,cos\beta \tag{4}$$

If we assume that the elongation of the spring $\overline{AC}$ is equally distributed to the springs $\overline{AG}$ and $\overline{GC}$ and the one of the spring $\overline{DB}$ is equally distributed to the springs $\overline{DG}$ and $\overline{GB}$, the elastic energy stored in the springs $\overline{AC}$ and $\overline{DB}$ is expressed by the following:

$$U_{k\overline{AC}} = \frac{k_3}{2}\left(\frac{1}{2}u\,cos\alpha\right)^2 + \frac{k_3}{2}\left(\frac{1}{2}u\,cos\alpha\right)^2 \tag{5}$$

$$U_{k\overline{DB}} = \frac{k_4}{2}\left(\frac{1}{2}u\,cos\beta\right)^2 + \frac{k_4}{2}\left(\frac{1}{2}u\,cos\beta\right)^2 \tag{6}$$

Adding up from k_1 to k_4, the total elastic energy stored in the parallelogram element $\overline{ABCD}$ when applying a force F in the $\overline{AB}$ direction is given by:

$$U_{k\overline{ABCD}} = \frac{1}{2}k_1u^2 + \frac{1}{4}k_3u^2cos^2\alpha + \frac{1}{4}k_4u^2cos^2\beta \tag{7}$$
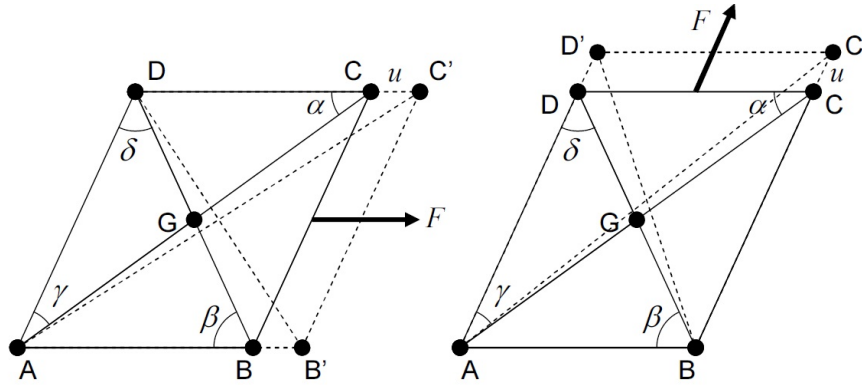
Figure 10: Uniaxial strain condition of the element.

Considering that the strain ϵ_0 is uniformly generated, the stress σ_0 acting in the strain direction can be obtained from:

$$\sigma_0 = \frac{E}{1-\nu^2}\epsilon_0 \tag{8}$$

The strain energy in the situation on the left of Figure 10 is given by:

$$U_s = \frac{1}{2}F\,u = \frac{1}{2}(\sigma_0 bh) \tag{9}$$

where b is the width of the element in the perpendicular direction with respect to the applied force and h is its thickness. Taking Equation 8 into account:

$$U_s = \frac{Ebh}{2(1-\nu^2)}\epsilon_0 u \tag{10}$$

Remembering the definition of strain

$$\epsilon = \frac{\Delta L}{L} \tag{11}$$

with L being the length of the side of an element parallel to the applied force; and substituting it into Equation 10, the following is obtained:

$$U_s = \frac{Eh}{2(1-\nu^2)}\frac{b}{L}u^2 \tag{12}$$

By applying the sine rule to the triangle $\widehat{ABC}$:

$$\frac{b}{L} = \frac{\overline{AC}\sin\alpha}{\overline{AC}\sin\gamma/\sin(\delta+\beta)} = \frac{\sin\alpha}{\sin\gamma}\sin(\delta+\beta) \tag{13}$$

Equating both Equations 12 and 7 by taking into account Equation 13, one gets:

$$\frac{1}{2}k_1 + \frac{1}{4}k_3\cos^2\alpha + \frac{1}{4}k_4\cos^2\beta = \frac{Eh}{2(1-\nu^2)}\frac{\sin\alpha}{\sin\gamma}\sin(\delta+\beta) \tag{14}$$

Proceeding in the same way for the case shown in the right hand side of Figure 10:

$$\frac{1}{2}k_2 + \frac{1}{4}k_3\cos^2\gamma + \frac{1}{4}k_4\cos^2\delta = \frac{Eh}{2(1-\nu^2)}\frac{\sin\delta}{\sin\beta}\sin(\alpha+\gamma) \tag{15}$$

Now, the parallelogram element $\overline{BHCG}$ shall be considered:
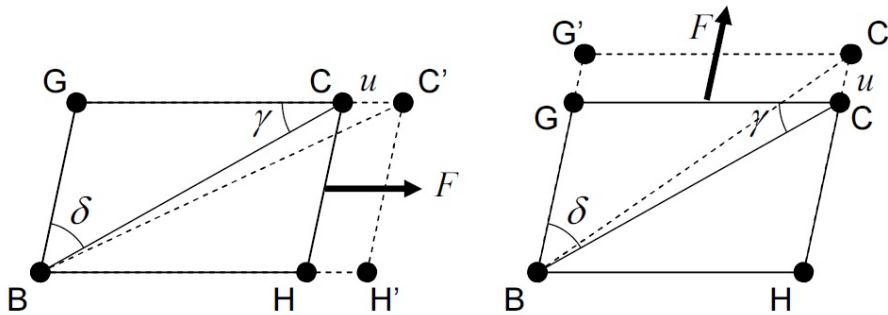
Figure 11: Uniaxial strain condition of the parallelogram element $\overline{BHCG}$.

Starting, as before, with the case shown in the left side of the image, where the force F is given in the $\overline{BH}$ direction, the elastic energy stored in the spring $\overline{BH}$ is:

$$U_{k\overline{BH}} = \frac{1}{2}\left(\frac{k_3}{2}\right)u^2 \tag{16}$$

Again, the spring constant considered has been halved because of the presence of adjacent elements. Also, the elastic energy in $\overline{GC}$ is the same as $U_{\overline{BH}}$.

If the displacement u is deemed as small enough, the elongation of the spring $\overline{BC}$ is:

$$u_{\overline{BC}} = u \, cos\gamma \tag{17}$$

Therefore, the elastic energy in $\overline{BC}$ is:

$$U_{k\overline{BC}} = \frac{k_2}{2}\left(u \, cos\gamma\right)^2 \tag{18}$$

Adding up for all the parallelogram element:

$$U_{k\overline{GBHC}} = \frac{1}{2}k_3 u^2 + \frac{1}{2}k_2 u^2 cos^2\gamma \tag{19}$$

Equating again with the strain energy given by Equation 12:

$$\frac{1}{2}k_3 + \frac{1}{2}k_2 cos^2\gamma = \frac{Eh}{2(1-\nu^2)}\frac{sin\gamma}{sin\delta}sin(\alpha+\beta) \tag{20}$$

Similarly, this time considering a displacement in the $\overline{BG}$ direction, the following holds:

$$\frac{1}{2}k_3 + \frac{1}{2}k_2 cos^2\delta = \frac{Eh}{2(1-\nu^2)}\frac{sin\beta}{sin\alpha}sin(\gamma+\delta) \tag{21}$$

By expressing the Equation 14, 15, 20, 21 in matrix formulation:

$$
\begin{bmatrix}
\frac{1}{2} & 0 & \frac{1}{4}cos^2\alpha & \frac{1}{4}cos^2\beta \\
0 & \frac{1}{2} & \frac{1}{4}cos^2\gamma & \frac{1}{4}cos^2\delta \\
0 & \frac{1}{2}cos^2\gamma & \frac{1}{2} & 0 \\
0 & \frac{1}{2}cos^2\delta & 0 & \frac{1}{2}
\end{bmatrix}
\begin{bmatrix}
k_1 \\ k_2 \\ k_3 \\ k_4
\end{bmatrix}
=
\begin{bmatrix}
\frac{Eh}{2(1-\nu^2)}\frac{sin\alpha}{sin\gamma}sin(\delta+\beta) \\
\frac{Eh}{2(1-\nu^2)}\frac{sin\delta}{sin\beta}sin(\alpha+\gamma) \\
\frac{Eh}{2(1-\nu^2)}\frac{sin\gamma}{sin\delta}sin(\beta+\alpha) \\
\frac{Eh}{2(1-\nu^2)}\frac{sin\beta}{sin\alpha}sin(\gamma+\delta)
\end{bmatrix}
\tag{22}
$$

Equation 22 can, then, be easily solved for the spring constants:

$$
\begin{bmatrix}
k_1 \\ k_2 \\ k_3 \\ k_4
\end{bmatrix}
=
\begin{bmatrix}
\frac{1}{2} & 0 & \frac{1}{4}cos^2\alpha & \frac{1}{4}cos^2\beta \\
0 & \frac{1}{2} & \frac{1}{4}cos^2\gamma & \frac{1}{4}cos^2\delta \\
0 & \frac{1}{2}cos^2\gamma & \frac{1}{2} & 0 \\
0 & \frac{1}{2}cos^2\delta & 0 & \frac{1}{2}
\end{bmatrix}^{-1}
\begin{bmatrix}
\frac{Eh}{2(1-\nu^2)}\frac{sin\alpha}{sin\gamma}sin(\delta+\beta) \\
\frac{Eh}{2(1-\nu^2)}\frac{sin\delta}{sin\beta}sin(\alpha+\gamma) \\
\frac{Eh}{2(1-\nu^2)}\frac{sin\gamma}{sin\delta}sin(\beta+\alpha) \\
\frac{Eh}{2(1-\nu^2)}\frac{sin\beta}{sin\alpha}sin(\gamma+\delta)
\end{bmatrix}
\tag{23}
$$

For the outer tether connecting both the membrane and the tip mass, its spring constant is determined by:

$$k_t = \frac{E_t \pi r_t^2}{L_0} \tag{24}$$

where E_t, r_t and L_0 are the tether's Young's modulus, radius and length, respectively. The inner tether is modelled by concatenating several springs and masses, the constants of which are also calculated by means of Equation 24.

2.2.3 Model for compression stiffness

In the motion analysis of a large membrane surface by Multi Particle Model, the compression stiffness of the membrane surface can be almost ignored or treated as sufficiently small with respect to the tension one [16]. This happens because the membrane itself is not easily compressed and the second moment of area is extremely small. Buckling, however, occurs relatively frequently due to the compressive forces acting on the membrane. The stiffness against buckling receives the name of apparent compression stiffness, and will be presented as introduced in the Multi Particle Model in [17].
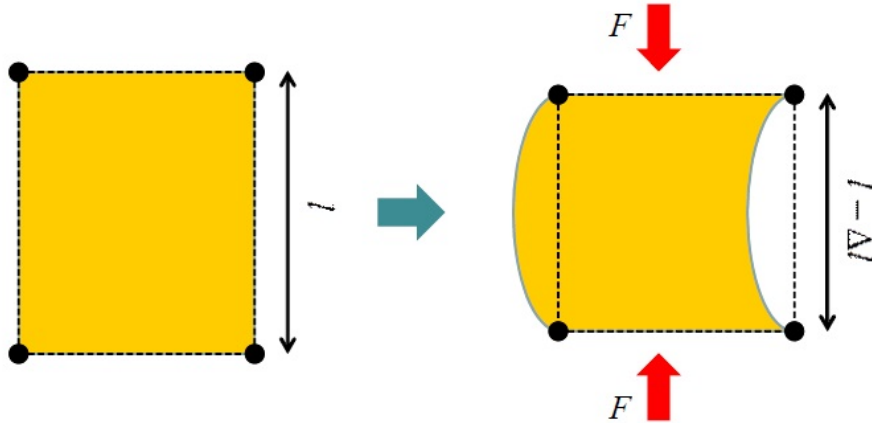
Figure 12: Buckling in membrane as simulated by compression springs in the Multi Particle Model.

Despite at fist it was modelled by means of a sufficiently small compressive spring constant, which lead to the smooth deformation shown in Figure 12, such a model cannot simulate the deformation of the membrane occurring on the folds that form when it is stored before its deployment. Therefore, local buckling in the folds is simulated by torsion springs instead, and is regarded together with bending stiffness. That way, deformation due to compressive forces adopts the form shown in Figure 13, which takes into account the presence of creases due to the folding.
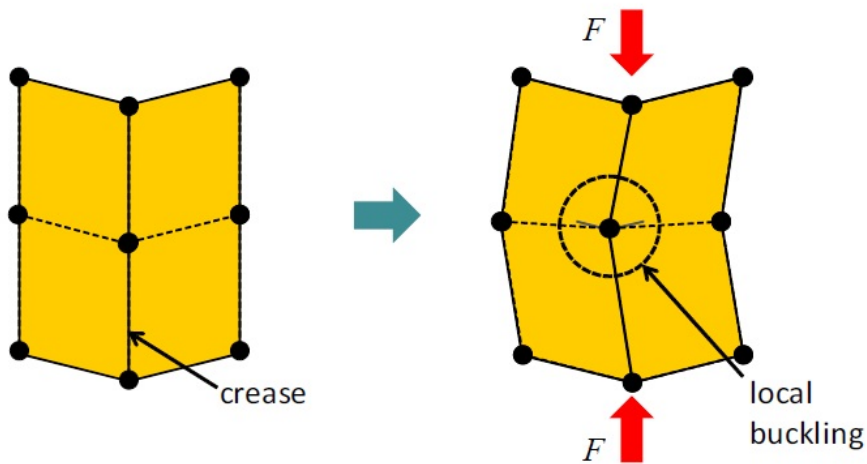
Figure 13: Buckling in membrane as simulated by compression and torsion springs in the Multi Particle Model.

The model assumed in the analysis for the compression stiffness consists on the application of a stress proportional to the tensile strain, as presented in Figure 14. The compression stiffness coefficient α is the ratio between both compression and tension stresses, and its calculation will be carried on differently depending on whether the spring is placed over a crease.
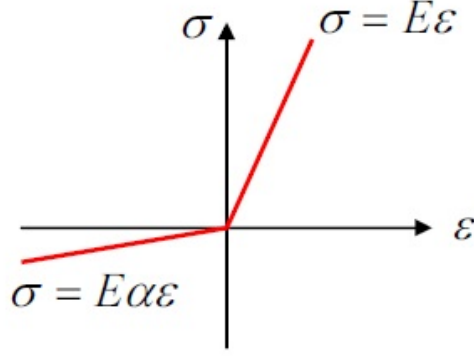
Figure 14: Compression stiffness model.

Let α_{s0} be the compression stiffness coefficient outside a crease. In that case, it is considered that the membrane buckles to a smooth shape as it is shown in Figure 12. By applying the Elastica Theory to the present case of analysis, the coefficient can be expressed as:

$$\alpha_{s0} = \eta \frac{h^2 \pi^2}{12 l^2} \tag{25}$$

where h is the thickness of the membrane's film and l is the buckling length. In this analysis, l will be considered equal to the natural length of the spring, L_s. η is a coefficient that was determined empirically in [18], with a value equal to 1.18, that will be used in this research.

For the compression stiffness coefficient on a crease, α_{sc}, as its value is difficult to obtain theoretically, the same model as in α_{s0} was considered, although a compression stiffness correction coefficient κ_s was added:

$$\alpha_{sc} = 1.18 \kappa_s \frac{h^2 \pi^2}{12 L_0^2} \tag{26}$$

The determination of κ_s was also done experimentally, in [17], where a value of 1×10^4 was obtained.

To sum up, the compression stiffness coefficient is expressed as it follows:

$$\alpha = \begin{cases} \alpha_{s0} & \text{on creases} \\ \kappa_s \alpha_{s0} & \text{otherwise} \end{cases} \tag{27}$$

2.2.3.1 Force on the membrane

Considering both the tension and compression stiffness simulated by means of springs, the inter-particle force can be expressed as the following, by adding up what has been introduced in the last two sections:

$$F = \begin{cases} k_t(L - L_0) + \beta k_t \dot{L} & \text{if } L \geq L_0 \\ \alpha k_t(L - L_0) + \beta \alpha k_t \dot{L} & \text{if } L < L_0 \end{cases} \tag{28}$$

where L is the inter-particle distance. In Equation 28, the effect of the damper has also been added, being β the structural damping coefficient that depends on the material of the surface.

2.2.4 Model for bending stiffness

In general, the bending stiffness of the film surface can be neglected as being sufficiently small. However, the bending stiffness of thin film solar cells and liquid crystal devices attached to the membrane can not be neglected.

Therefore, to more accurately model the membrane dynamics one has to consider out-of-plane stiffness, also known as bending stiffness. As mentioned above, bending stiffness is modelled my means of torsion springs, placed so as to connect two adjacent surface elements as shown in Figure 15.
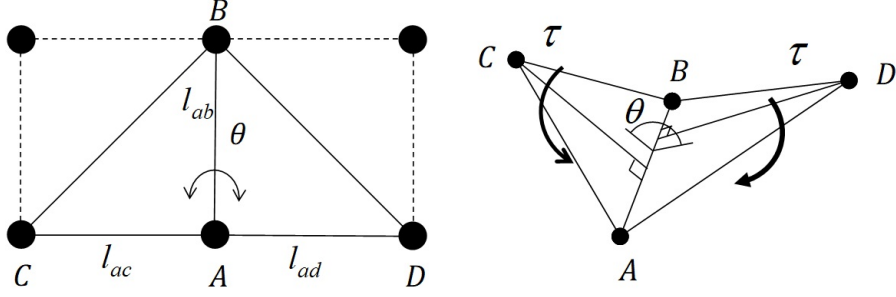
Figure 15: Bending stiffness model in MPM.

According to [19], a system of three consecutive particles can be regarded as a beam structure. The forces generated over the outermost particles are obtained from the torsion spring constant as it follows:

$$F_i = k_{\theta_i} \cdot \frac{l_{AB}(\theta - \theta_0)}{l_i^2} \tag{29}$$

where θ and θ_0 are the bending and natural bending angles, and k_i is the corresponding torsion spring constant.

From the cantilever equation, the deflection ω_i is:

$$\omega_i = \frac{F_i l_i^3}{3EI} \tag{30}$$

if the deflection ω_i is small enough, its slope can be approximated like

$$\theta_i = \frac{\omega_i}{l_i} \tag{31}$$

Using equations Equation 30 and Equation 31, k_i is then derived as:

$$k_{\theta_i} = \frac{3EI}{l_i} \equiv k_{\theta_0} \tag{32}$$

being E the Young's modulus and I the second moment of area:

$$I = \frac{l_i h^3}{36} \tag{33}$$

where h is the thickness of the membrane.

The torsion τ obtained would be then:

$$\tau = k_{\theta_i}(\theta - \theta_0) \tag{34}$$

Despite the cantilever model allows us to approximate the effect of the bending moment on the sail, according to [20] the deformation observed in IKAROS during low-spin operation did not match the simulations, but was that expected from a more rigid membrane model, that is, presenting a greater bending stiffness.

Only a small percentage of IKAROS membrane was covered by RCD or thin-film solar cells. However, in the case of OKEANOS, almost all the surface of the sail is covered by such devices, so the differences between the predicted and the actual deformation would differ even more if the model were not to be adjusted.

Both in IKAROS and OKEANOS cases, before its deployment the membrane was folded. The creases formed on the membrane during the folding process are believed to present a higher bending stiffness, which might have led to the divergence between the model and the real deformation. Therefore, the surface elements placed in a crease have to be treated accordingly.
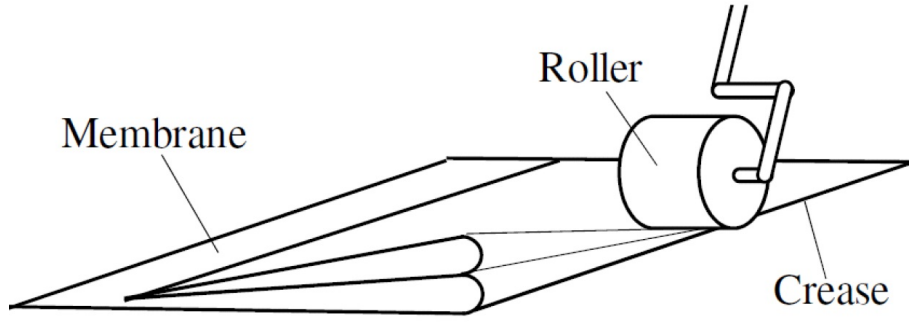
Figure 16: Folding process.

For a system of surface elements in which the particle A exists over a crease, the torsion spring constant is obtained by a correction factor κ_θ:

$$k_{\theta_i}^* = \kappa_\theta k_{\theta_0} \tag{35}$$

The parameter κ_θ is difficult to be obtained in ground, so in this paper several values will be considered so as to simulate different possible situations of membrane deformation.
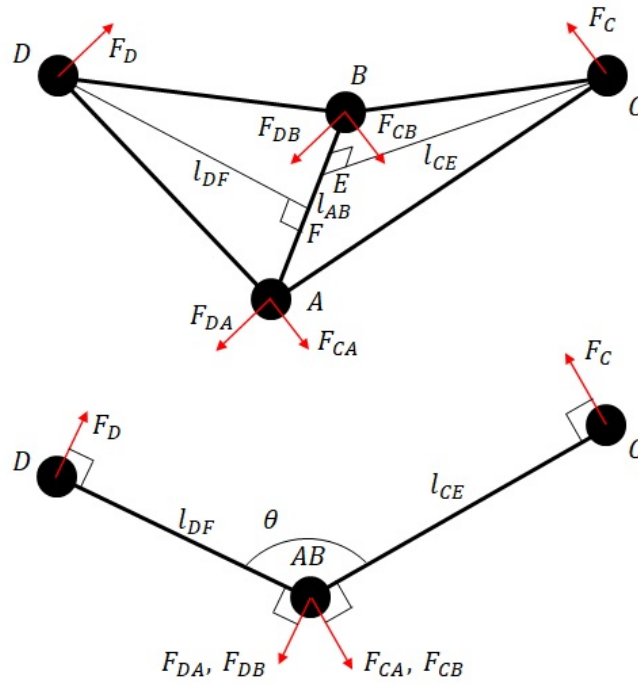
Figure 17: Bending force model scheme.

The forces acting on each particle as described in Figure 17 are, by substituting k_i in Equation 29 for its corresponding value, as it follows [21]:

$$F_C = \tau \frac{l_{AB}}{l_{CE}^2} \tag{36}$$

$$F_D = \tau \frac{l_{AB}}{l_{DF}^2} \tag{37}$$

The forces acting on the masses A, B (Equations 38 - 41) are set to cancel the rigid-body motion of the triangular elements:

$$F_{DA} = - F_D \cdot \frac{l_{FB}}{l_{AB}} \tag{38}$$

$$F_{DB} = - F_D \cdot \frac{l_{FA}}{l_{AB}} \tag{39}$$

$$F_{CA} = - F_C \cdot \frac{l_{EB}}{l_{AB}} \tag{40}$$

$$F_{CB} = - F_C \cdot \frac{l_{EA}}{l_{AB}} \tag{41}$$

Also, in the case that membrane contact occurred, a penalty torque should be added to the torque τ. That is, when the dihedral angle is lower than zero degrees or higher than 360 degrees, a penalty torsion spring constant is supposed to act on the surfaces as it follows:

$$\tau_{pen} = \begin{cases} k_{\theta_{pen}}(0 - \theta) & \theta < 0 \text{ rad} \\ k_{\theta_{pen}}(\theta - 2\pi) & \theta > 2\pi \text{ rad} \end{cases} \tag{42}$$

2.2.5   Governing equations in kinetic analysis

The kinetics of the whole spacecraft are to be simulated by stating the equations governing both the translational and rotational motion. Prior to stating the governing equations, though, a coordinate system has to be specified.

2.2.5.1   Coordinate system

In order to properly analyse the attitude motion of the satellite, both an inertial reference frame and a body-fixed coordinate system should be defined. The former will be denoted as E_I while the last will be expressed by E_B.

In the initial position of the probe, both systems are set to coincide. By considering the main body as a cylinder, the z-axis is taken to be in the same direction as the axis of the cylinder, considering a zero value in its geometric centre. The positive direction of the z-axis is taken vertically upwards, such that the counter-clockwise spin is defined as positive. The x-axis and the y-axis are chosen accordingly to complete a right handed coordinate system, both origins of the axis placed in the mounting position of the inner tether.
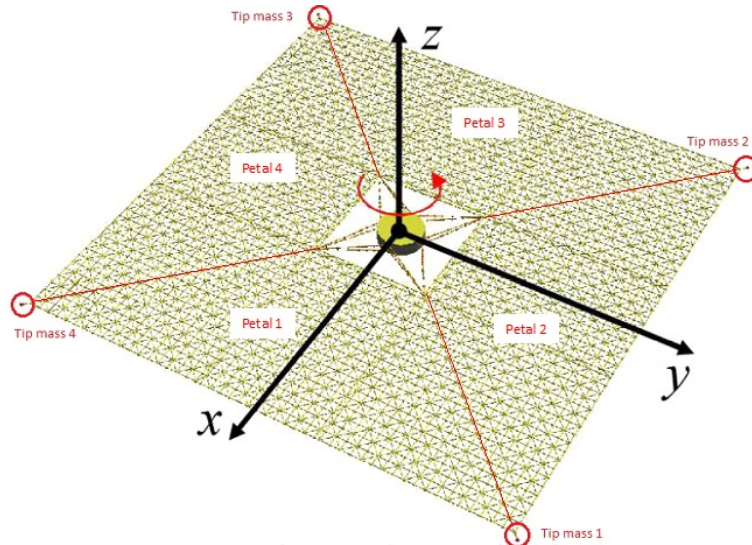
Figure 18: Axis, petal and tip mass distribution.

The numeration of the petals is done so as the one deployed in the positive x-axis direction gets the number one and the rest are ordered sequentially following the spin direction. The tip mass between the first two petals is defined as number one, the rest being arranged in the very same way as the petals. The axis and the numeration of both petals and tip masses can be seen in Figure 18.

The relationship between both coordinate systems can be expressed by a rotation of an angle Θ around a rotation axis $\hat{\boldsymbol{u}} = [u_1 \ u_2 \ u_3]$, with which a quaternion $\boldsymbol{q} = [e_0 \ e_1 \ e_2 \ e_3]$ can be defined, where

$$e_0 = cos\frac{\Theta}{2}; \quad e_i = u_i sin\frac{\Theta}{2} \tag{43}$$

From its definition, the norm of the quaternion equals one.

By using the quaternion, it is possible to define the rotation matrix from the inertial system to the body-fixed one:

$$R_{IB} = \begin{pmatrix} (e_1^2 - e_2^2 - e_3^2 + e_0^2) & 2(e_1e_2 + e_3e_0) & 2(e_1e_3 - e_2e_0) \\ 2(e_1e_2 - e_3e_0) & (-e_1^2 + e_2^2 - e_3^2 + e_0^2) & 2(e_2e_3 + e_1e_0) \\ 2(e_1e_3 + e_2e_0) & 2(e_2e_3 - e_1e_0) & (-e_1^2 - e_2^2 + e_3^2 + e_0^2) \end{pmatrix} \tag{44}$$

2.2.5.2 Equations for the translational motion

As described above, the body-fixed coordinate system takes its origin so that the connecting coordinates of the tether with the main body are symmetrical. The centre of gravity of the spacecraft will be also considered coincident with the origin of coordinates.

The equation of motion of every particle is simply obtained from the Newton's second law:

$$m_i\ddot{\boldsymbol{r}_i} = \boldsymbol{F_i} \tag{45}$$

where i goes from one to n, being n the number of particles.

The very same equation is applied to the hub, considered a rigid body.

$$m_B\ddot{\boldsymbol{r}_B} = \boldsymbol{F_B} \tag{46}$$

where $\boldsymbol{r_B}$ is the position vector of the centre of gravity of the probe. In both Equations 45 and 46 the vectors are expressed in the E_I system.

2.2.5.3 Equations for the rotational motion

In order to express the rotational motion of the hub, the following equation is considered:

$$\boldsymbol{I_B}\dot{\boldsymbol{\omega}} + \boldsymbol{\omega} \times (\boldsymbol{I_B}\boldsymbol{\omega}) = \boldsymbol{\tau_B} \tag{47}$$

where $\boldsymbol{\omega}$ is the angular velocity vector of the body, $\boldsymbol{I_B}$ its inertia tensor and $\boldsymbol{\tau_B}$ the sum of torques applied to it.

All vectors in the equation are represented in the body-fixed coordinate system E_B. Finally, the relationship between the quaternion and the angular velocity vector is expressed by:

$$\dot{\boldsymbol{e}} = \frac{1}{2}(e_0\boldsymbol{I} - \tilde{\boldsymbol{e}})\boldsymbol{\omega} \tag{48}$$

$$\dot{e}_0 = -\frac{1}{2}\boldsymbol{e}^T\boldsymbol{\omega} \tag{49}$$

with $\boldsymbol{e} = [e_1 \ e_2 \ e_3]^T$ of the quaternion.

2.2.5.4 State vector

In order to express the equations of the system in matrix notation, the state vector $\boldsymbol{Z}$ is defined:

$$\boldsymbol{Z} \equiv \begin{bmatrix} \boldsymbol{r}_1^T & \dots & \boldsymbol{r}_n^T & \boldsymbol{v}_1^T & \dots & \boldsymbol{v}_n^T & \boldsymbol{r}_B^T & \boldsymbol{v}_B^T & \boldsymbol{e}^T & e_0 & \boldsymbol{\omega}^T \end{bmatrix}^T \tag{50}$$

The state vector $\boldsymbol{Z}$ has a total of $6n + 13$ elements, with $\boldsymbol{r}_i$ and $\boldsymbol{v}_i$ being the position and velocity of every particle in the membrane in inertial coordinates and the last 13 columns corresponding to the position, velocity, attitude and angular position of the main body.

By using the state vector $\boldsymbol{Z}$ and Equations from 45 to 49, the system of first order nonlinear ordinary differential equations is obtained.

$$\frac{d\boldsymbol{Z}}{dt} = \begin{bmatrix} \boldsymbol{v}_1 \\ \vdots \\ \boldsymbol{v}_n \\ \boldsymbol{F}_1/m_1 \\ \vdots \\ \boldsymbol{F}_n/m_n \\ \boldsymbol{v}_B \\ \boldsymbol{F}_B/m_B \\ (e_0\boldsymbol{I} - \tilde{\boldsymbol{e}})\boldsymbol{\omega}/2 \\ -\boldsymbol{e}^T\boldsymbol{\omega}/2 \\ \boldsymbol{I}_B^{-1}(\boldsymbol{\tau}_B - \boldsymbol{\omega} \times (\boldsymbol{I}_B\boldsymbol{\omega})) \end{bmatrix} \tag{51}$$

To solve Equation 51, the Runge-Kutta-Gil method is used.

3 Attitude Control System

In this document, the spin axis reorientation for the OKEANOS solar sail will be studied by means of thrusting input.

3.1 Parameters for the evaluation of the attitude motion

Despite the quaternion can be used to describe the attitude of the spacecraft with respect to the inertial frame, and it will indeed be used to calculate the spacecraft's attitude at each iteration, the Euler angles roll ϕ, pitch θ and yaw ψ have been considered to be more intuitive when analysing the attitude of the sail. Therefore, this document will work with them when representing the attitude of both the membrane and the central probe. In particular, the Tait-Bryan angles' definition for the $z - x' - y''$ sequence will be considered, as shown in Figure 19
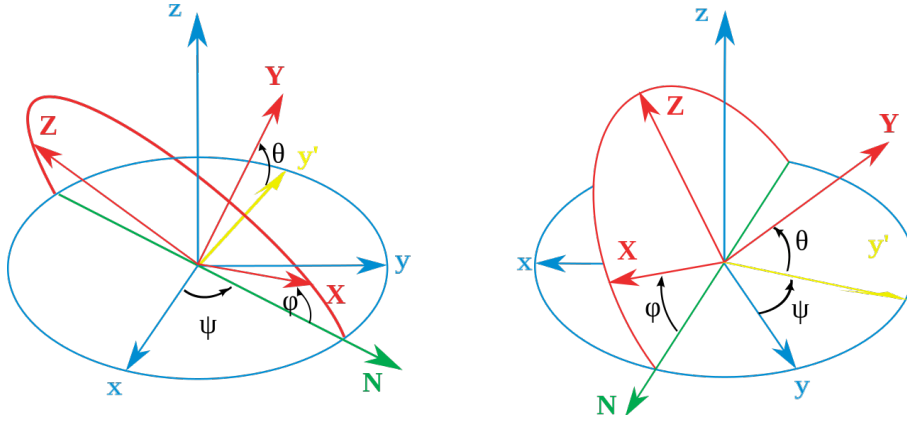
Figure 19: Tait–Bryan angles. $z-x'-y''$ (intrinsic rotations, N coincides with x').

where ψ corresponds to the rotation about the z axis, θ is the rotation over the newly obtained x axis or x', and finally, ϕ consists on the rotation about y''.

By the use of the Euler angles, the relation between body-fixed coordinates and an inertial coordinates system can be expressed by means of the Direction Cosine Matrix in Equation 52:

$$DCM = \begin{pmatrix} cos\theta cos\psi - sin\phi sin\theta sin\psi & cos\theta sin\psi & cos\psi sin\phi + cos\phi + sin\psi sin\theta \\ cos\phi sin\psi + cos\psi sin\theta sin\phi & cos\psi cos\theta & sin\phi sin\psi - cos\psi cos\phi sin\theta \\ -sin\phi cos\theta & sin\theta & cos\phi cos\theta \end{pmatrix} \quad (52)$$

The angles describing the attitude of the hub of the spacecraft are obtained from the trigonometric relationship between the definition of the quaternion and the Euler angles. The attitude of the membrane, however, is obtained from an average quaternion that comes from the orientation of every sail element.
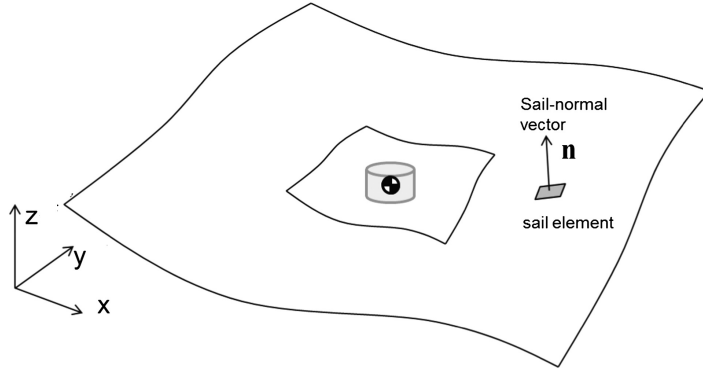
Figure 20: Diagram showing the orientation of a sail element.

Also, the angle between the averaged normal vector of the sail and the inertial Z_I axis will also be considered in the analysis.

3.2 Spin-Axis reorientation

The attitude control of the sail is done mainly by the impulsive torque originated from the thrusters present in the spacecraft. OKEANOS has a total number of eight thrusters on the main body to perform spin up, spin down and reorientation, as it can be seen in the Figure 21:
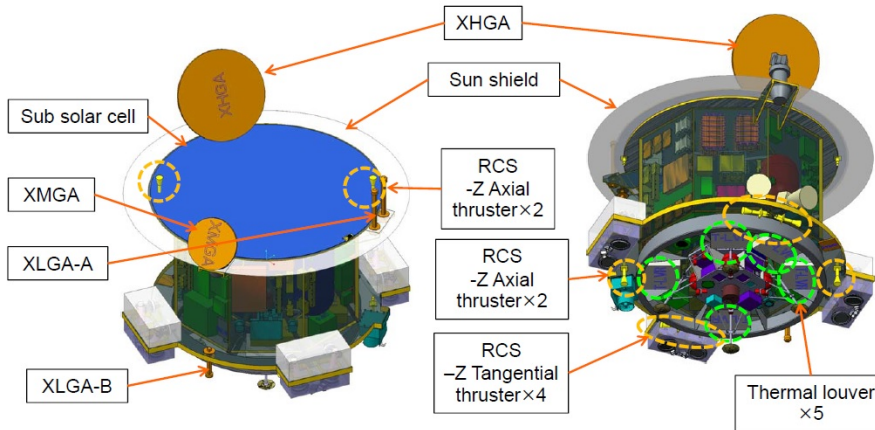
Figure 21: Systems in OKEANOS' main body as presented in [2].

This report will focus on the membrane dynamics when applying attitude control for the reorientation of the sail, so only the Z-axial thrusters will be considered. Such thrusters provide a force of 20 N and are displayed symmetrically along the main body, at a radial distance of 1.8 m from the centre of the probe.

There are four axial thrusters in the hub, whose thrusting force and torque are added to the $\boldsymbol{F_B}$ and $\boldsymbol{\tau_B}$ of Equation 46 and 47 in the corresponding E_I or E_B system, respectively. The firing of the thrusters will be considered to be in the z_B direction at all times.

Applying Newton's second law to rigid-body motion provides the inertial rate of change of the angular momentum H under a perpendicular torque vector $\boldsymbol{T}(t)$ [22]:

$$\boldsymbol{T}(t) = \frac{d\mathbf{H}}{dt} \tag{53}$$

The torque causes the angular momentum vector $\boldsymbol{H}$ to precess along the vector $\Delta\boldsymbol{H}$ that, considering an infinitesimal interval Δt and that the torque $\boldsymbol{T}$ remains constant during that interval, gives:

$$\Delta\mathbf{H} = \mathbf{H}(t + \Delta t) - \mathbf{H}(t) \approx \boldsymbol{T}\Delta t \tag{54}$$

From the scheme presented in Figure 22, one can derive:

$$tan(\delta\theta) = \frac{\Delta H}{H} \tag{55}$$
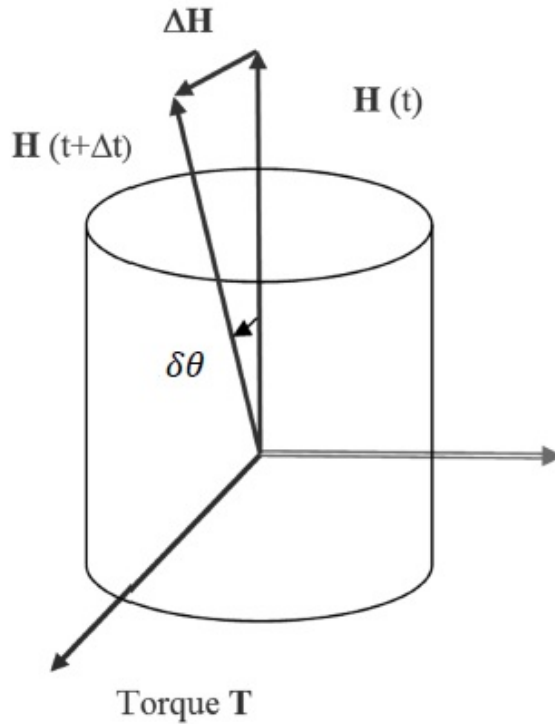
Figure 22: Inertial precession of angular momentum vector.

From Equation 54 and recalling, in absence of nutation:

$$H = I_{zz}\omega_z \tag{56}$$

one obtains the precession angle $\delta\theta$:

$$tan(\delta\theta) \approx \frac{\tau\Delta t}{I_{zz}\omega_z} \tag{57}$$

3.3 Rhumb-Line Maneuver

For a single-spin satellite, the Rhumb-Line maneuver is one of the most effective and easier ways to change the orientation of the spinning axis up to a certain value. The maneuver simply consists on giving an angular impulse on detection of a certain inertial reference such as the Sun, approximately once every revolution around the major spinning axis. The resulting motion is characterized by the fact that when plotted in a Mercator plot with the inertial reference at the pole, the trajectory of the angular momentum vector would yield a straight line, that means, a constant heading angle [23].

In OKEANOS, the references used for the Rhumb-Line Maneuver are both the Sun-angle and a Sun-pulse given by a Sun-sensor present in the main body. The pseudo-algorithm used for implementing the maneuver is as in Algorithm 1:

Algorithm 1: Rhumb-Line Maneuver

Input: inertial sun vector, initial attitude
Output: final attitude
  Initialisation :
  while $t <$*simulation time* **do**
    Calculate sun vector in satellite coordinates:
    if (*y-coord sun vector switches sign*) **and** (*x-coord < 0*) **then**
      Sun-pulse occurs $\implies$ *Pulse Flag* ON, $cnt = 0$
    end if
    LOOP Process
    if (*Pulse Flag*) **and** ($cnt < \Delta t$) **then**
      Thruster On, $cnt = cnt + \delta t$
    end if
    Dynamics Calculation
    return New Attitude
    if ($cnt \geq \Delta t$) **then**
      Thruster Off, *Pulse Flag* OFF
    end if
    $t = t + \delta t$
  end while

The starting point is calculating the sun-vector given in the inertial frame to the satellite frame by means of the Direction Cosine Matrix. When the y-coordinate of the sun direction vector in the satellite coordinate system switches between plus and minus, and the x coordinate at that time is negative, it is assumed that a sun pulse occurs. Thus, the thrusters are considered on for the computation of the dynamics of the whole system during a set activation time Δt. When Δt is over, the thrusters are set off until the next sun pulse occurs, where the Direction Cosine Matrix is updated at every time iteration with the new attitude of the main body of the spacecraft.

4   In-Body Thrust Simulations

Having already described the simulation method used in this research, in this section the results corresponding to the spin axis reorientation maneuver of the spacecraft will be presented. The objective of the maneuver is to bring the pitch angle of the sail from zero to 45° while keeping the roll angle equal to zero, as it was considered to be relevant for the objectives of the mission.

4.1   Simulation Conditions

For the simulations done, the following parameters and conditions were considered:

Table 2: Simulation Conditions

Numerical Conditions		
Time Discretization		
Step Width	5.00E-05	[s]
Space Discretization		
Number of Particles	1056	
Number of Elements	1728	
Dimensions and Physical Properties		
Central Probe		
Radius	1.8	[m]
Mass	1159	[kg]
Ixx	481.9	[kgm$\hat{2}$]
Iyy	481.9	[kgm$\hat{2}$]
Izz	647.8	[kgm$\hat{2}$]
Initial Attitude (quaternion)	[1 0 0 0]	
Spin Rate	6	[deg/s]
Film Surface		
Inner Radius	3.245	[m]
Outer Radius	19.85	[m]
Tip Mass	5	[kg]
Damping coefficient β	3.90E-05	[s]
Young's Modulus E	3.20E+09	[Pa]
Poisson's Ratio	0.33	
Thickness	5.50E-05	[m]
Density	1.42E+03	[kg/m$\hat{3}$]
Thin film solar cell		
Damping coefficient β	3.90E-05	[s]
Compression coefficient α	1.0E-06	[s]
Young's Modulus E	3.20E+09	[Pa]
Poisson's Ratio	0.33	
Thickness	8.25E-05	[m]
Density	6.83E+02	[kg/m$\hat{3}$]
Reflectivity Control Device		
Damping coefficient β	3.90E-05	[s]
Compression coefficient α	1.0E-06	[s]
Young's Modulus E	3.20E+09	[Pa]
Poisson's Ratio	0.33	
Thickness	5.00E-05	[m]
Density	1.42E+03	[kg/m$\hat{3}$]

Tether		
Damping coefficient β	3.90E-05	[s]
Young's Modulus E	1.00E+11	[Pa]
Radius	7.30E-04	[m]
Density	1.81E+03	[kg/m$\hat{3}$]

Thruster Settings		
Number	4.00E+00	
Position (radial)	1.80E+00	[m]
Position (angular)	45 + 90*i	[deg]
Thrust	±20	[N]
Thrusting time	0.25	[s]

SRP		
Not set		

The values contained in Table 2 have been taken accordingly to the OKEANOS mission configuration as per now.

4.2 Bending Moment Analysis during Rhumb-Line Maneuver

As mentioned in section 2.2.4, the current bending stiffness model, which is used to simulate the membrane rigidity, does not provide the behaviour observed during IKAROS operation.

In the model, the rotational spring constant is obtained from the cantilever equation 32, depending on the distance between particles, the Young's Modulus and the height of the membrane. However, its value in the creases formed from the folding of the membrane prior to its launching is believed to present values far above the ones obtained by the cantilever approximation. That is the reason why a a correction factor κ_θ is added in the elements placed along such creases accordingly with Equation 35. In the current section, its value will be varied so as to get closer to the rigid-membrane behaviour. Considering that OKEANOS has more elements than IKAROS in its membrane, such as a layer of thin film solar cells, it is believed that it will present even an increased rigidity, so as to correctly simulate the dynamics during operation is necessary to find first the value of the bending constant at which a change of behaviour is observed.

The correction factor was varied so as to obtain an effective k_θ^* in creases going from zero (no bending stiffness considered) up to 1×10^{-2}, increasing its value by a factor of 10 from $k_\theta^* = 1 \times 10^{-8}$ onwards. In the following figure, Figure 23, the evolution of the pitch angle of the sail for the effective torsion spring constant of zero, $K = K_{beam}$, $K = 1 \times 10^{-3}$ and $K = 1 \times 10^{-2}$ is presented. $K = K_{beam}$ is the one obtained by a $\kappa_\theta = 1$, that is, the same value as the one given by Equation 32, and its value is approximately 1×10^{-5}. The value indicated is just to give the order of magnitude in most part of the sail, since it changes accordingly with the distribution of the membrane devices. No further results have been included in Figure 23 for a matter of clarity. Also, the the value of the pitch is that corresponding to the mean of the angle variation during an interval of 50 seconds, for a better visualization.

In Figure 23 it has been also represented in yellow the theoretical attitude of the sail from what was obtained in Equation 57.

It can be seen that the angular evolution of the sail's attitude, although presenting some differences between the no-bending case and the rest, presents almost the same behaviour up until the $K = 1 \times 10^{-3}$ case. It is worth mentioning that between $K = K_{beam}$ and $K = 1 \times 10^{-3}$ there are two orders of magnitude. When being in this value's range, the sail does not get close to the theoretically expected value, which would be obtained if it was a rigid system.
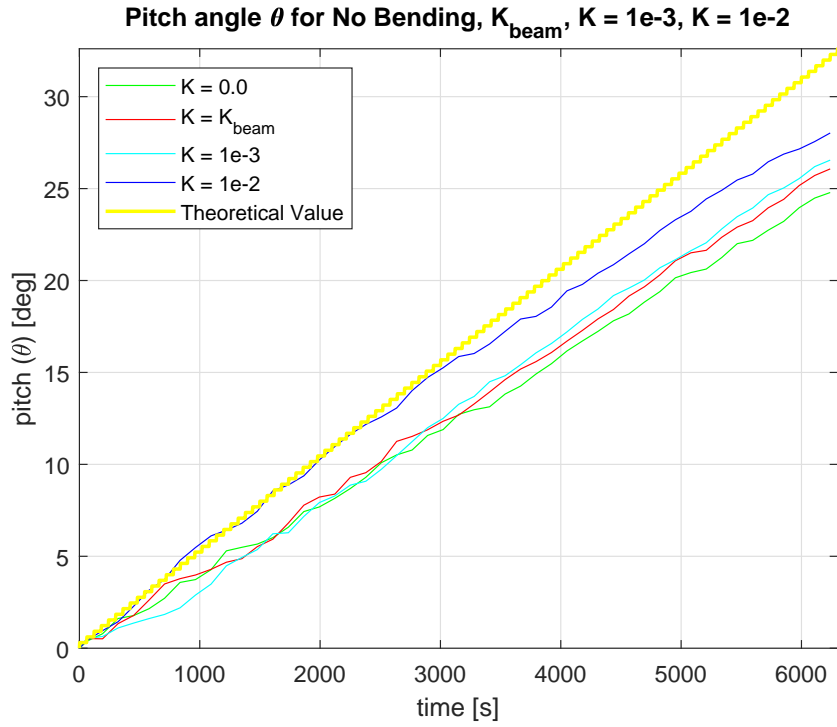
Figure 23: Pitch of the full sail system over time for different values of K.

Nonetheless, for $K = 1 \times 10^{-2}$ that trend changes, and the sail presents dynamics similar to that of a rigid body, although it diverges on late states of the simulation. These differences are not only visible when representing the pitch angle, but are also noticeable when observing directly the aspect of the surface of the sail when rendering it from the MPM data:

(a) $K = K_{beam}$.
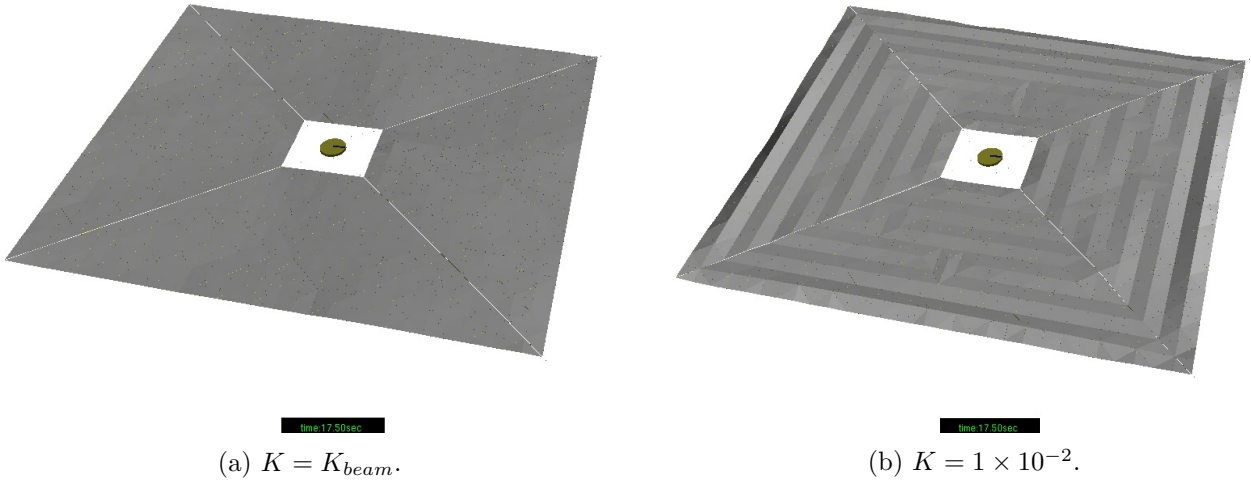
(b) $K = 1 \times 10^{-2}$.

Figure 24: Sail display for $K = 1 \times 10^{-3}$ and $K = 1 \times 10^{-2}$ at a simulation time $t = 17.5$ s.

In Figure 24, the membrane aspect of the simulated sail for $K = 1 \times 10^{-2}$ shows a surface full of creases corresponding to the ones formed during the folding, aspect that is not obtained for lower correction factors κ_θ for the bending constant on creases.

The images taken during IKAROS low-spin operation by a deployable camera, as shown in Figure 25, suggest the presence of creases in the membrane, similar to the ones in the right of Figure 24.

26

Although not appearing as prominent as in Figure 24, that fact suggests an increased bending stiffness when compared to the predicted one being the main cause behind the differences between the actual and simulated deformation.
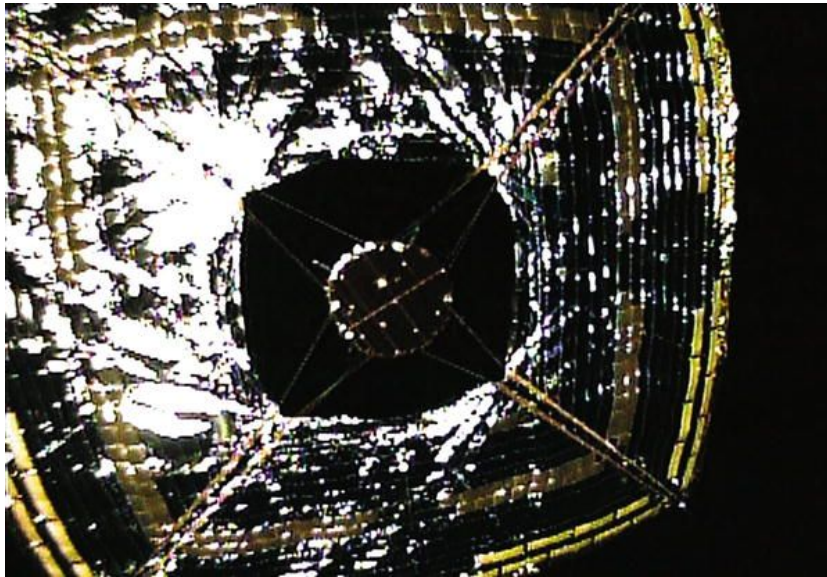
Figure 25: IKAROS pictured by a deployable camera during its low spin operation.

Because of the difference of behaviour arising at $K = 1 \times 10^{-2}$, so as to avoid redundancy, only the simulations for that bending constant and the one corresponding to the cantilever approximation K_{beam} will be analysed thoroughly in this document, as they both are the most representative ones out of the cases here considered.

4.2.1 $K = K_{beam}$ and $K = 1 \times 10^{-2}$ cases analysis

The following figures present the pitch angle for both the sail system and the hub, as well as the roll angle.
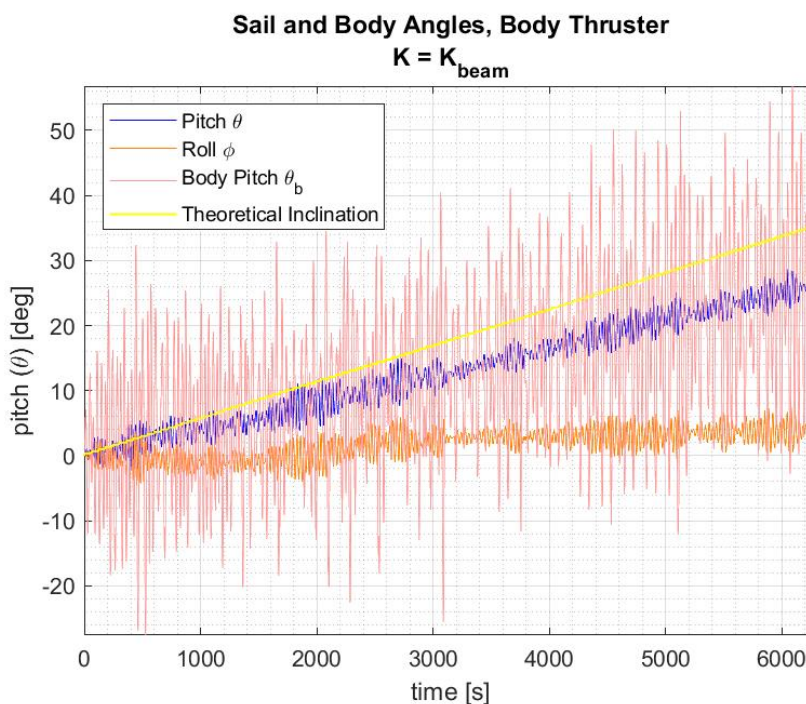
Figure 26: Pitch and roll angles for K_{beam} over time.
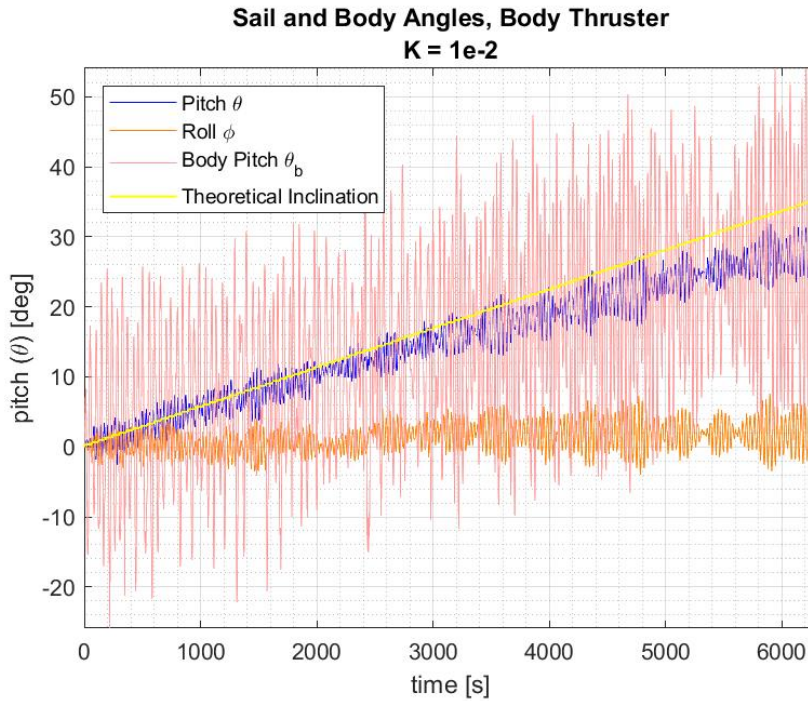
Figure 27: Pitch and roll angles for $K = 1 \times 10^{-2}$ over time.

Here, the oscillation in the angular values can be appreciated. While the pitch angle for the sail system does not present strong oscillations, for the hub its value changes over a range of about 40°. Regarding the relative difference between the pitch angle of the sail and the hub and the expected theoretical angle, the following is obtained:
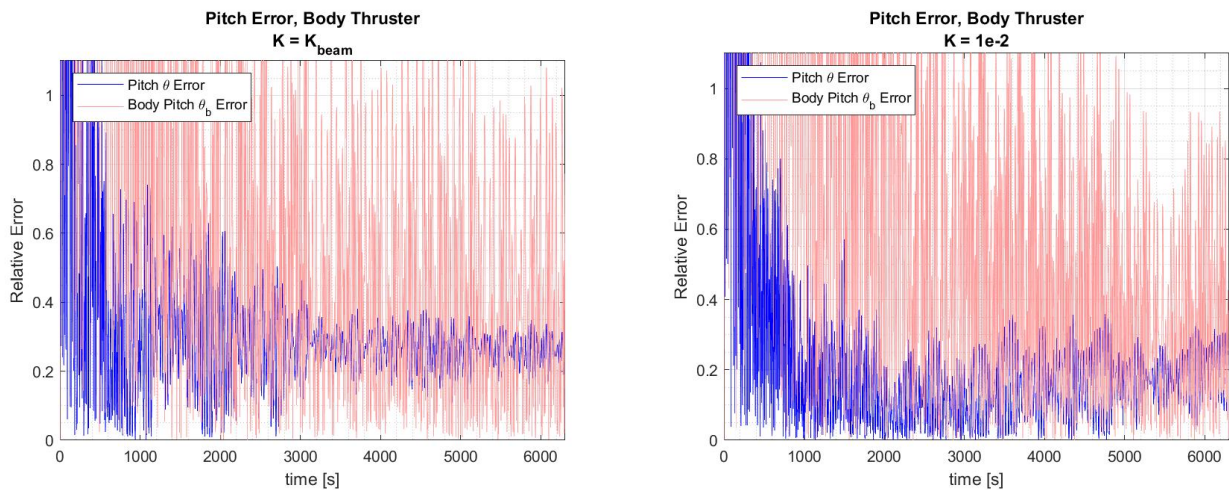
(a) $K = K_{beam}$.

(b) $K = 1 \times 10^{-2}$.

Figure 28: Relative error between theoretical and expected pitch angle.

For the left side of Figure 28, the error obtained after 6000 seconds of simulation is around 30% for the sail's pitch angle, while in the case placed on the right, it oscillates between $10 - 30\%$. However, for both cases the error concerning the pitch angle of the hub remains at about 100%.

The difference in both the pitch and roll angles of the sail due to the effect of the bending stiffness is presented below:
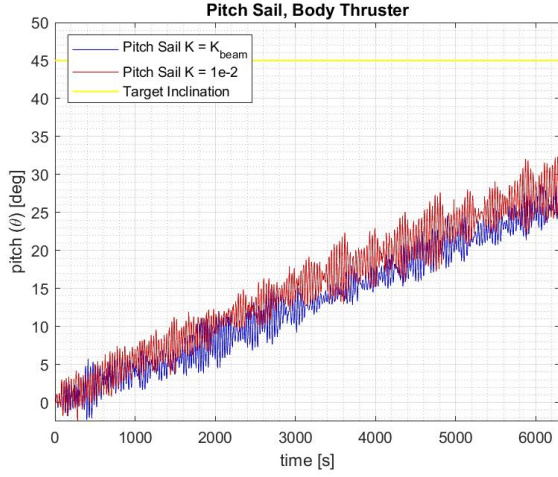
(a) Pitch Angles.
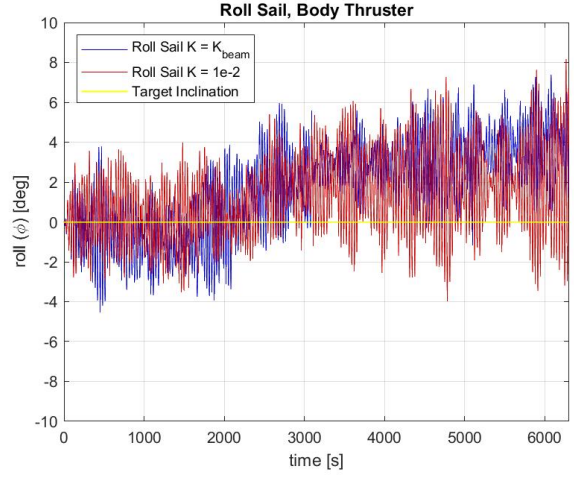
(b) Roll Angles.

Figure 29: Difference between sail's pitch and roll angle for $K = K_{beam}$ and $K = 1 \times 10^{-2}$.

Overall, as commented before, the higher bending stiffness case behaves closer to what would be expected from a rigid body, presenting a low error as shown in Figure 28, that is, a higher performance in the reorientation maneuver. As it can be seen in Figure 29 ot inferred from comparing both subplots in Figure 28, the difference between both cases considered is of about 10%. Considering the roll angle, the one corresponding to the $K = 1 \times 10^{-2}$ case is kept closer to zero, which would be the ideal value for a rigid body.

In Figures 26 and 27, the pitch angle of the hub was seen to present a large variation. In the following plots, the attitude of the hub of the spacecraft is presented for the case of $K = K_{beam}$, so as to avoid repetition.

Figure 30: Pitch, yaw and roll angles for the main body of the sail, $K = K_{beam}$.

Both pitch and roll angles are seen to diverge in addition to their variation. Such variation is due to the nutation motion arising in the hub, that can be easily seen when plotting the components of its angular velocity that do not belong to the spin axis:

Figure 31: Nutational motion of the main body of the sail, $K = K_{beam}$.
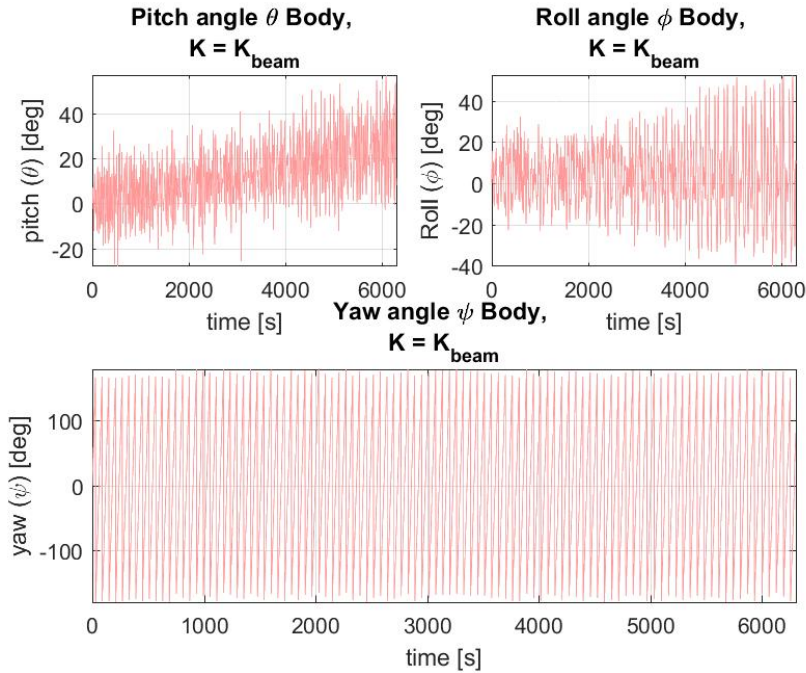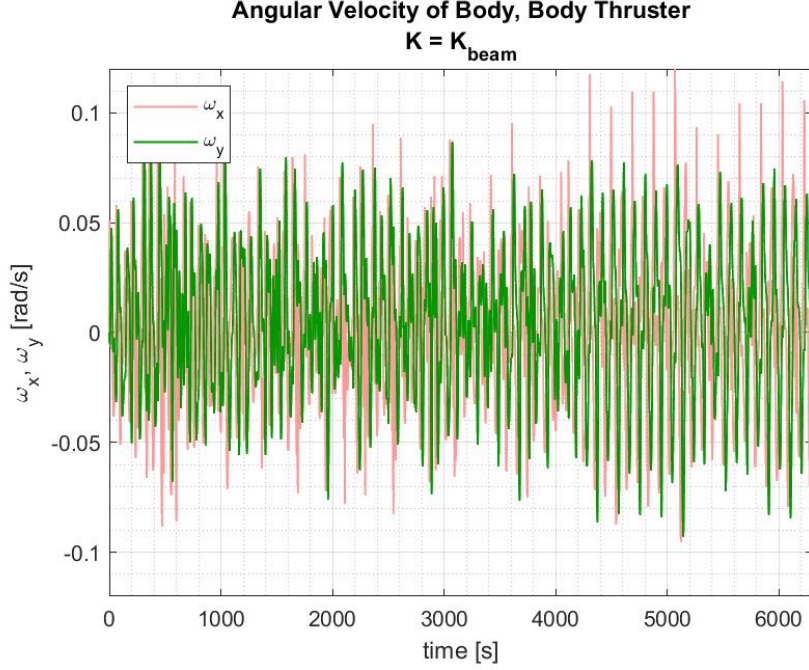
Despite being a spacecraft spinning around its major inertia axis, the nutation of the probe is seen to diverge.

When Rhumb-Line Control is applied to the solar sail, the flexibility of the membrane must be taken into account, as it will introduce disturbances with respect to the behavior of a rigid body. In [5], parting from the membrane dynamics as derived from Newton's equations by using the continuum model, the oscillation of a circular membrane is derived by excluding both high-order modes and the effect of the bending stiffness of the sail. However, their results will be used to explain the results of the simulations above.

The coupling between the sail deformation and the hub dynamics neglecting the bending moment effect is described in the following equations, the derivation of which is developed in [5] by Nakano.

$$\bar{I}_M \ddot{\zeta} + I_M \Omega^2 \zeta + I_M(\Omega \omega_y + \dot{\omega}_x) = 0 \tag{58}$$

$$\bar{I}_M \ddot{\varphi} + I_M \Omega^2 \varphi + I_M(-\Omega \omega_x + \dot{\omega}_y) = 0 \tag{59}$$

with $I_M = 2\pi h \int_{r_a}^{r_b} \mu r^3 dr$ and $\bar{I}_M = 2\pi h \int_{r_a}^{r_b} \mu r^2 (r - r_a) dr$ being the moment of inertia of the membrane with respect to the spin axis, with $\bar{I}_M$ considering the radial oscillation mode. Here, μ, h, r_a and r_b are the area density, thickness, inner radius and outer radius of the sail, respectively; and ω_x, ω_y, Ω are the spin and the angular velocity of the hub. Both ζ and φ stand for first-order mode of the out-of-plane deformation.

The total angular momentum is expressed in Equation 59:

$$\hat{L} = I\omega + \oint \hat{\rho} \times (\dot{\hat{\rho}} + \omega_M \times \hat{\rho}) dm \tag{60}$$

And, from the law of conservation of angular momentum, one can write for the coupling membrane-hub [5]:

$$I\dot{\omega}_x + (J - I)\Omega \omega_y + \frac{1}{2}\bar{I}_M(\ddot{\zeta} + \Omega^2 \zeta) = 0 \tag{61}$$

$$I\dot{\omega}_y - (J - I)\Omega \omega_x + \frac{1}{2}\bar{I}_M(\ddot{\varphi} + \Omega^2 \varphi) = 0 \tag{62}$$

30

In these equations, J and I are the moment of inertia of the whole sail and the hub.

When applying an external torque [3], Equations 58-59, 61-62 become:

$$\bar{I}_M\ddot{\zeta} + I_M\Omega^2\zeta + I_M(\Omega\omega_y + \dot{\omega}_x) = -c\bar{I}_M\dot{\zeta} \tag{63}$$

$$\bar{I}_M\ddot{\varphi} + I_M\Omega^2\varphi + I_M(-\Omega\omega_x + \dot{\omega}_y) = -c\bar{I}_M\dot{\varphi} \tag{64}$$

$$I\dot{\omega}_x + (J-I)\Omega\omega_y + \frac{1}{2}\bar{I}_M(\ddot{\zeta} + \Omega^2\zeta) = -k\omega_x \tag{65}$$

$$I\dot{\omega}_y - (J-I)\Omega\omega_x + \frac{1}{2}\bar{I}_M(\ddot{\varphi} + \Omega^2\varphi) = -k\omega_y \tag{66}$$

where c and k are the dumping of the connections in both the sail and between sail and hub, respectively, normally having really small values.

As in Nakano et. alt, by doing the Laplace transform of Equations 63-66 and substituting ζ and φ into the last two ones, one gets:

$$IsW_x + (J-I)\Omega W_y - \frac{1}{2}\bar{I}_M\frac{(1+Q)(s^2+\Omega^2)}{s^2+cs+(1+Q)\Omega^2}(sW_x + \Omega W_y) = -kW_x \tag{67}$$

$$IsW_y - (J-I)\Omega W_x - \frac{1}{2}\bar{I}_M\frac{(1+Q)(s^2+\Omega^2)}{s^2+cs+(1+Q)\Omega^2}(sW_y - \Omega W_x) = -kW_y \tag{68}$$

where

$$Q \equiv \frac{I_M}{\bar{I}_M} - 1 \tag{69}$$

Assuming $Q \approx 0$, the following characteristic equation is obtained:

$$
\begin{aligned}
&(I - \frac{1}{2}\bar{I}_M)^2 s^6 + 2(k+cI)(I - \frac{1}{2}\bar{I}_M)s^5 \\
&+ (k^2 + c^2I^2 + 2ck(2I - \frac{1}{2}\bar{I}_M) + \Omega^2((J-I-\frac{1}{2}\bar{I}_M)^2 + 2(I-\frac{1}{2}\bar{I}_M)^2))s^4 \\
&+ (2ck(cI+k) + \Omega^2(4k(I-\frac{1}{2}\bar{I}_M) + 2c((J-I)^2 + I^2 - J\frac{1}{2}\bar{I}_M)))s^3 \\
&+ (c^2k^2 + \Omega^2(2k^2 + c^2(J-I)^2 + 2ck(2I-\frac{1}{2}\bar{I}_M)) + \Omega^4(2(J-I-\frac{1}{2}\bar{I}_M)^2 + (I-\frac{1}{2}\bar{I}_M)^2))s^2 \\
&+ (2ck^2\Omega^2 + 2\Omega^4(2k(I-\frac{1}{2}\bar{I}_M) + 2c(J-I)(J-I-\frac{1}{2}\bar{I}_M)))s \\
&+ k^2\Omega^4 + \Omega^6(J-I-\frac{1}{2}\bar{I}_M)^2 = 0
\end{aligned}
\tag{70}
$$

In equation **??**, all the coefficients except those of s^3 and s are positive. These last two are positive if k is large enough so as to compensate c, that is, if the damping on the spacecraft is larger than in the membrane. That is not true for the OKEANOS mission as it is now, so a feed-forward logic like Rhumb-Line Maneuver cannot stably change the spin axis when applied directly to the hub. To increase its stability, a larger dumping coefficient k would be needed. However, such parameter is difficult to increase, so an alternative control method is needed.

4.3 Frequency analysis on the response of the membrane due to in-body thrusting

It is believed that the differences in the spin-axis reorientation maneuver performance might be caused by higher vibration modes excitation in the flexible-most membrane. Therefore, in this section, the vibrations arising in the membrane will be studied.

4.3.1 Equation of motion of the membrane and vibration modes for the non-bending case

Considering a uniform and circular membrane in a linear region, where in-plane and out-of-plane vibrations can be treated independently, the latter will be considered under the plane stress assumption.

Assuming the spin rate of the system Ω to be constant and that the inner radius of the membrane to be far smaller than the external one $r_b \gg r_a$, the force in the out-of-plane (z) direction acting on a membrane infinitesimal element $dM = \rho h r dr d\theta$, with ρ and h being the density and thickness of the membrane, can be derived using the principles on the von Karman thin plate theory [24]:

$$dF_z = \left(\frac{\partial}{\partial r}\left(r\sigma_{rr}\frac{\partial w}{\partial r} \right) + \frac{1}{r}\frac{\partial}{\partial \theta}\left(\sigma_{\theta\theta}\frac{\partial w}{\partial \theta} \right) - \frac{Eh^2 r}{3(1-\nu^2)}\nabla^4 w \right) h dr d\theta \tag{71}$$

where E is the Young's modulus of the membrane, ν the Poisson's ratio, w the displacement in the z direction, and σ_{rr} and $\sigma_{\theta\theta}$ the planar tensile stresses in the radial and circumferential directions, which read as it follows [25]:

$$\sigma_{rr} = \frac{3+\nu}{8}\rho\Omega^2 r_b{}^2\left(1 - \frac{r^2}{r_b{}^2} \right) \tag{72}$$

$$\sigma_{\theta\theta} = \frac{3+\nu}{8}\rho\Omega^2 r_b{}^2\left(1 - \frac{1+3\nu}{3+\nu}\frac{r^2}{r_b{}^2} \right) \tag{73}$$
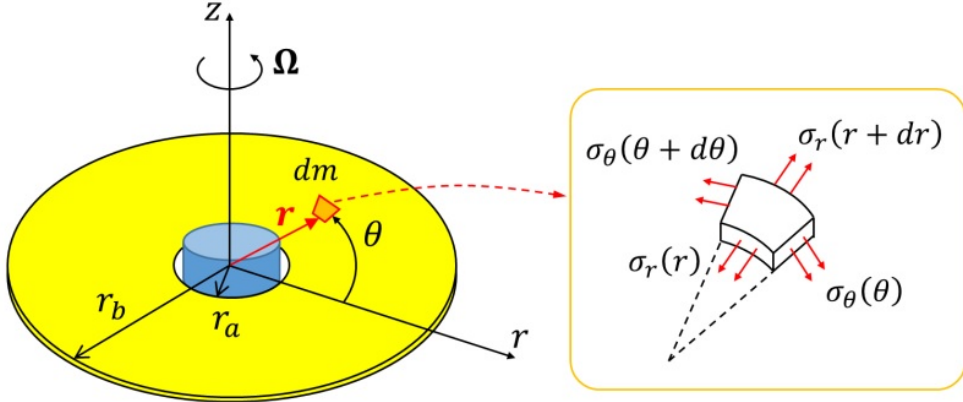
Figure 32: Analysis model of spinning membrane structure vibration.

Considering

$$dF_z = \frac{\partial^2 w}{\partial t^2} dM \tag{74}$$

the equation of motion is finally obtained:

$$\rho\frac{\partial^2 w}{\partial t^2} = \frac{1}{r}\frac{\partial}{\partial r}\left(r\sigma_{rr}\frac{\partial w}{\partial r} \right) + \frac{1}{r^2}\frac{\partial}{\partial \theta}\left(\sigma_{\theta\theta}\frac{\partial w}{\partial \theta} \right) - \frac{Eh^2}{3(1-\nu^2)}\nabla^4 w \tag{75}$$

This equation is the same as for a flexible membrane with exception for the term

$$\frac{Eh^2}{3(1-\nu^2)}\nabla^4 w \tag{76}$$

32

which accounts for the bending stiffness.

Ignoring the bending stiffness contribution in the equation of motion presented in Equation 75, one obtains:

$$\rho \frac{\partial^2 w}{\partial t^2} = \frac{1}{r} \frac{\partial}{\partial r}\left(r \sigma_{rr} \frac{\partial w}{\partial r}\right) + \frac{1}{r^2} \frac{\partial}{\partial \theta}\left(\sigma_{\theta\theta} \frac{\partial w}{\partial \theta}\right) \tag{77}$$

This last Equation 77 can be solved analytically, from which the derivation of the natural frequencies can be obtained the same way as Y. Takao did in [4]. The natural frequency of the vibrations in a flexible membrane made dimensionless by the spin rate $\tilde{\omega} = \omega/\Omega$ obtained in [4] is presented below:

$$\hat{\omega}_{n\nu'} = \sqrt{\frac{3+\nu}{8}(\nu' + n - 1)(\nu' + n + 1) - \frac{1+3\nu}{8}\nu'^2} \tag{78}$$

where ν' and n correspond to the circumferential and radial orders of vibration.

However, differently from the case in which bending stiffness is ignored, the equation of motion Equation 75 consists on a fourth order PDE. There have been different solving approaches to this equation, as that of [26], which rely on strong assumptions for the deformation function w and lead to a lower limit eigenvalue.

In our case of study, the force due to the thruster input should be added into the equation, as well as the coupling between the hub and membrane. Thus, the analytical approach to be solved gets its complication increased. Therefore, a numerical approach is chosen. The out-of-plane vibration of the particles along the simulations presented in the previous section 4.2 will be analysed in the frequency domain by using a Fast Fourier Transform (FFT) to search for the excited frequencies as well as the differences in front of a force input depending on the bending parameter K.

4.3.2 Fast Fourier Transform

Before the analysis, a few comments should be done.This study only considers particles belonging to the membrane, ignoring both the hub and the tethers and bridges connecting the two main parts of the spacecraft. Also, the out-of-plane displacement of the particles is obtained from calculating the orthogonal distance of each node to the mean plane of inclination of the sail, that is, a plane calculated from averaging the normal vectors to the surfaces of each of the elements constituting the membrane and that includes the spacecraft-frame origin of coordinates. As this virtual plane is subject to fluctuations at each time step, the presence of noise is expected. The z-axis position of the nodes in the spacecraft frame has not been taken as the out-of-place displacement, as if done so, we would also be accounting for the oscillations of the hub.

In the following figures, the single sided amplitude spectrum for the FFT of all the particles' out-of-plane displacement has been represented for simulations considering the no-bending case $K = 0$, $K = K_{beam}$ and $K = 1 \times 10^{-2}$.

In addition, the number of nodes in all the sail that have their maximum in a particular amplitude has been collected and represented in an histogram, as it is displayed in the right plot of Figures 33-35:
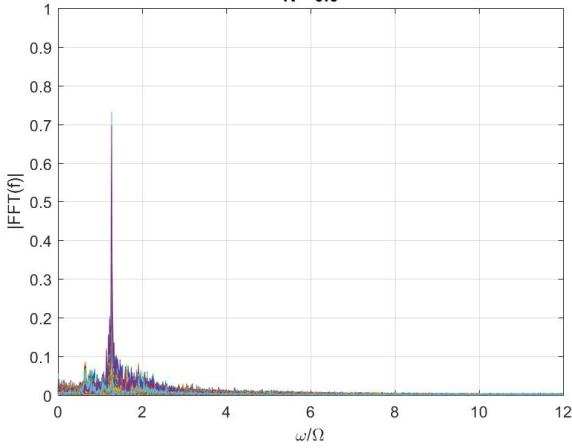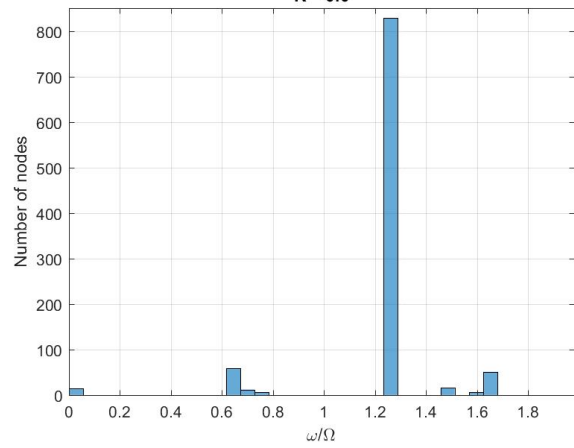
(a) Amplitude spectrum for particle displacement, $K = 0$.

(b) Frequency distribution in nodes along the sail, $K = 0$.

Figure 33: Frequency analysis by means of FFT for $K = 0$.
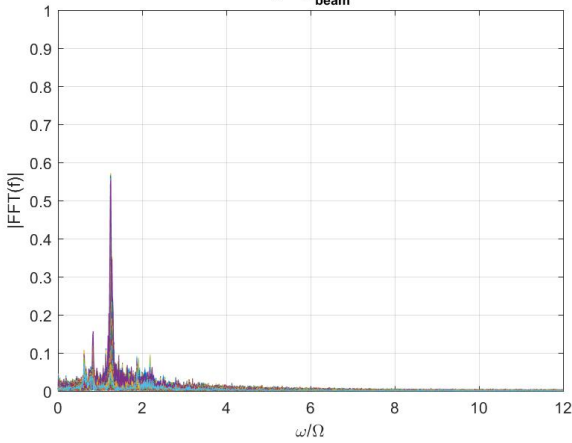
(a) Amplitude spectrum for particle displacement, $K = K_{beam}$.

(b) Frequency distribution in nodes along the sail, $K = K_{beam}$.

Figure 34: Frequency analysis by means of FFT for $K = K_{beam}$.
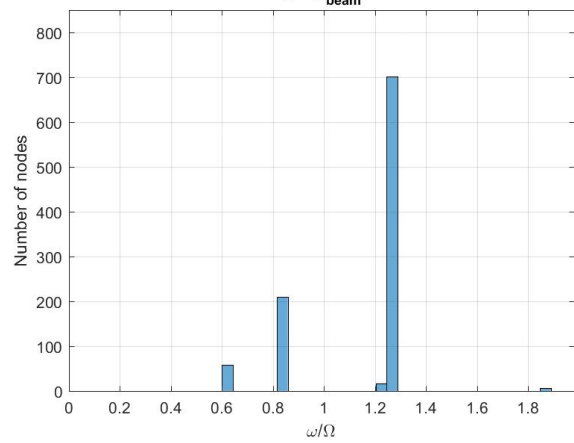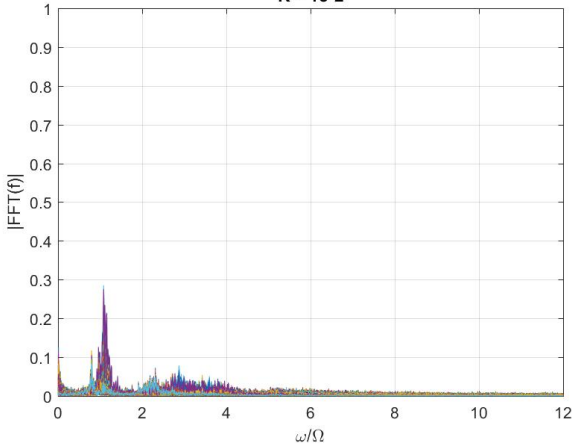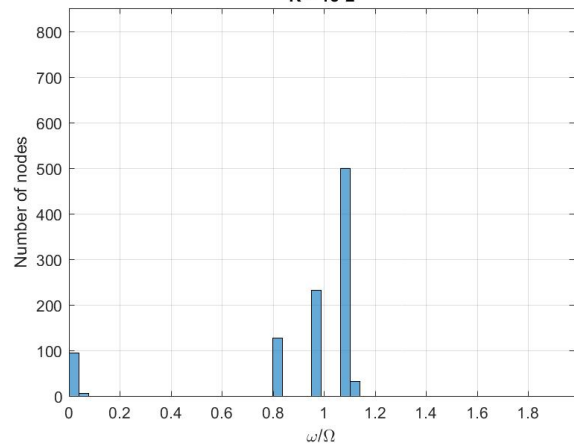

(a) Amplitude spectrum for particle displacement, $K = 1 \times 10^{-2}$.

(b) Frequency distribution in nodes along the sail, $K = 1 \times 10^{-2}$.

The cases for K values going from $K = 1 \times 10^{-8}$ to 1×10^{-3} have not been included here, as their spectrum presents the same behaviour as in Figure 33 and Figure 34. For both spectrum, a relevant peak is found at a frequency of around $\tilde{\omega} = 1.25$. A smaller peak also exists at a frequency of approximately $\tilde{\omega} = 0.85$.

For the case of $K = 1 \times 10^{-2}$, the amplitude of the dominant peak is reduced, as well as displaced to lower frequencies. Besides, a wider range of frequencies around the main peak are also excited. That change of behaviour goes in consonance with the results obtained in Section 4.2, which showed that the $K = 1 \times 10^{-2}$ is the threshold from which non-flexible dynamics of the membrane can be seen.

Considering Equation 78, the natural frequencies obtained at $n = 1$ are presented in the figure below. Apart from the analytical value, the values corresponding to a circular and square sail models have also been plotted, as obtained in [27]:
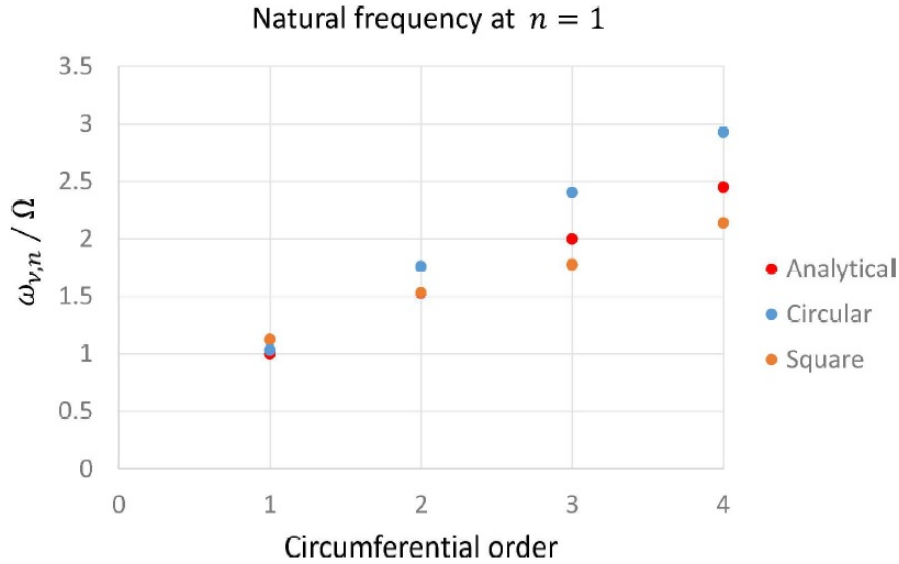
Figure 36: Natural frequencies obtained for $n = 1$ depending on the circumferential order ν'.

When comparing Figures 33-35 with Figure 36, it can be seen that except for the $K = 1 \times 10^{-2}$ case, the frequency associated with $\nu' = 1$ for a square membrane is clearly excited. As a trend, the higher the bending parameter and, therefore, its significance in the equation of motion, the more nodes appear to be excited around a $\tilde{\omega} = 1$, that is, a lower frequency than the expected one. However, it is not until a more rigid behaviour is reached that an actual peak occurs at that frequency. Recalling the control method used in the simulations, the forced input occurs once in a spin, that is, at a $\tilde{\omega} = 1$. The higher the bending moment, the more nodes are excited at that forced frequency and the lower become the amplitude of the modes associated with a completely flexible behaviour.

Finally, in the following figures Figure 37 and 38, the whole sail has been mapped in both maximum amplitude and frequency of the maximum amplitude. The particular nodal points that present the maximum amplitude at one of the frequencies observed are also highlighted.
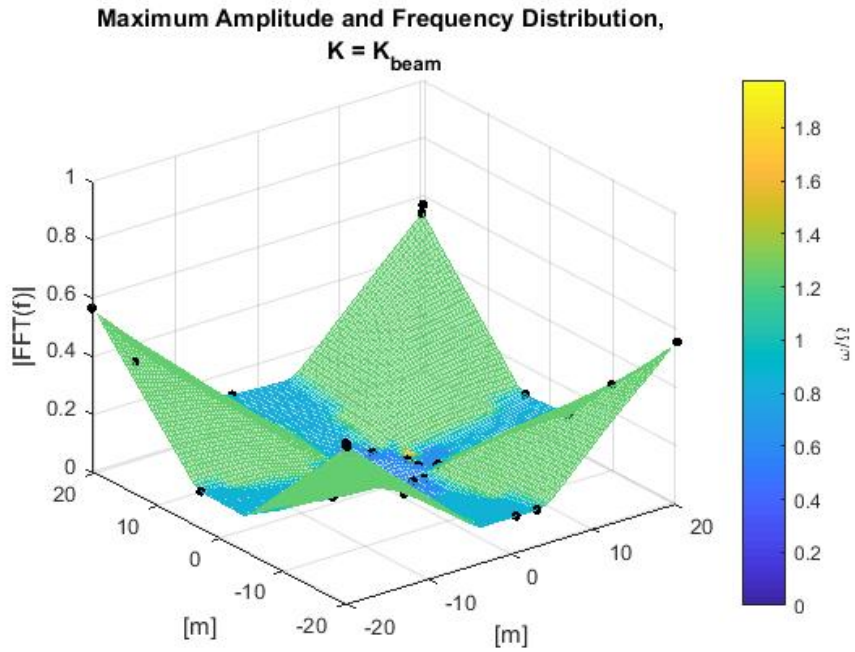
Figure 37: FFT amplitude spectrum distribution, $K = K_{beam}$.
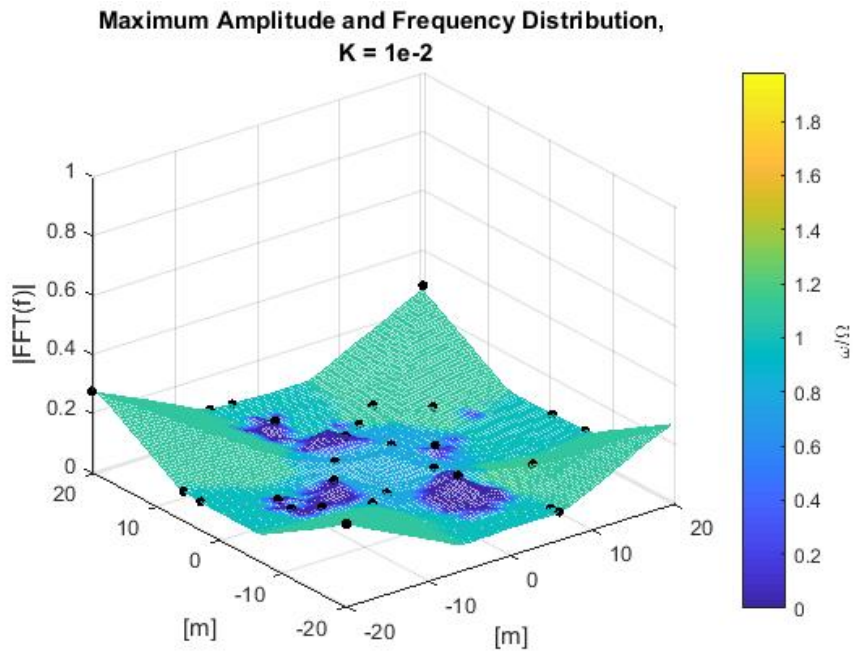
Figure 38: FFT amplitude spectrum distribution, $K = 1 \times 10^{-2}$.

It can be seen that the nodes presenting higher amplitudes are those placed around the diagonal of the petal, which is where the tethers are connected. Those nodes normally present a peak at the same frequency as the tip mass (node 248), which is the one in the furthest position in the radial direction. and, according to the displacement function derived for a flexible membrane [4], the displacement gets higher in magnitude. On the other hand, the nodes placed in the centre of the petal present a lower response in both magnitude and frequency, which also goes accordingly with [4].

All in all, in Figures 37 and 38 it is clearly seen that mode vibrations vary along the circumferential direction while resonance magnitude changes in the radial direction.

4.4 Insights

After the first simulations, the Rhumb-Line Maneuver's effectiveness is proved capable of changing the spin-axis orientation. However, due to the coupling between the hub and the sail, and the flexibility of the last, it is seen that the maneuver cannot be performed stably, and that the nutation arising diverges.

Regarding the bending stiffness model, it is observed that the torsion spring constant considered as the bending parameter, if calculated from a cantilever approximation of a particle system, cannot give the rigidity to the membrane that characterized IKAROS' low spin operation. The transition between flexible behaviour and plate-like behaviour is found, after several simulations, at a value of $K = 1 \times 10^{-2}$, value at which the membrane dynamics change and it no longer behaves as a completely flexible structure. The higher the bending stiffness, the the better the attitude adjustment due to the control input.

In regards to the frequency domain analysis, for the completely flexible and K_{bend} cases, a excitation of the natural modes of the sail is found, accordingly to the model of a sail without the presence of bending stiffness as presented in [4].

For the higher bending stiffness case, however, the behaviour changes. The peak before placed in the natural frequency is displaced to the left of the spectra, as well as being halved in magnitude. Furthermore, other significant peaks appear at the same frequency as the control input.

Therefore, the difference in performance observed during the axis-reorientation maneuver is most probably affected by the vibrations arising in the sail: the higher the vibrations, the lower the response.

5   Tip-mass Thrust Simulations

In the previous section, Section 4, a control method based on thrusters present in the hub of the OKEANOS spacecraft was proposed, as well as a frequency analysis of the out-of-plane displacement of the particles as a response to such input. Different magnitudes of bending moment were considered, as it was found that the behaviour of the sail is affected by this parameter, for which a correct approximation to its value has proven to be difficult, specially considering the higher amount of in-membrane devices when compared to IKAROS.

5.1   Setting

Due to thruster firings, the main body of the spacecraft presented an undesired nutation motion, and given that the connection hub-membrane is done by tethers and thus, is not that of a rigid body, disturbances arose. Therefore, in the present report, a new control setting is proposed. The thruster input is to take place at the tip-masses, that is, four thrusters placed respectively in each of the tip masses of the spacecraft are considered. That way, the thrusting will act on the membrane instead of in the hub, being the former the dominant part of the moment of inertia of the whole spacecraft.
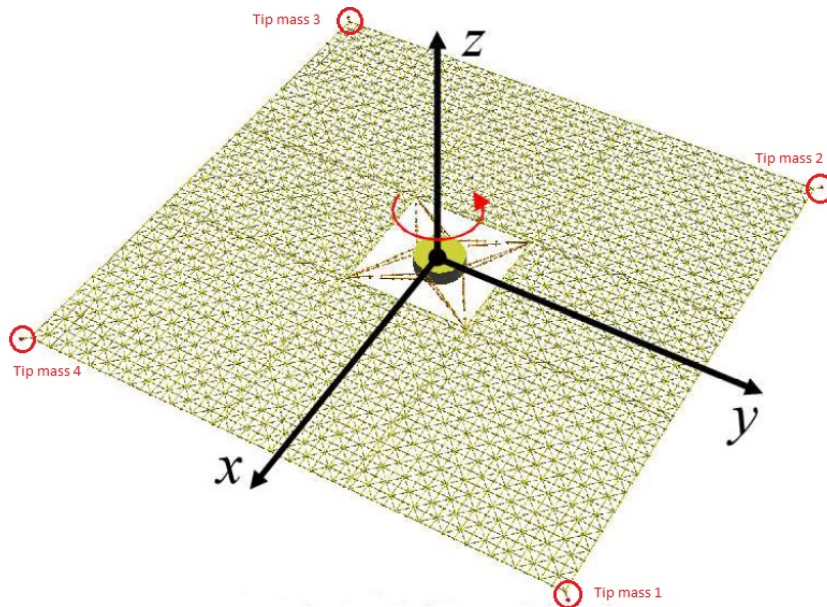

Figure 39: Tip mass placement along the axis (note that the sail dimensions are that of IKAROS for a better display of the figure).

The control algorithm, however, will remain as the Rhumb-Line Maneuver as presented in Algorithm 1, in other words, every time the sun sensor activates, a thruster firing will occur. The activation of the sun sensor happens in the event of a sun-pulse, when the y-coordinate of the sun direction vector in the satellite coordinate system switches between plus and minus, and the x coordinate at that time is negative. This takes place once per spin, when the projection on the inertial xy-plane of the local x-axis coincides with the inertial one. This way, a torque M_x should be generated.

Having an external force acting directly over the membrane instead of the hub will result in a reduction of the nutation motion of the last one, as well as lowering the influence of the connection hub-sail on the dynamics of the system. Also, it will allow a higher control over the vibration modes excited in the membrane, as tip-masses presented the most significant response to oscillations as seen in 4.3. In addition, as the thrusting force will be applied in the furthermost possible point from the centre of gravity, a higher torque-fuel ratio is obtained.

Control by means of an input in the membrane has already been studied in [3] by means of Reflectivity Control Devices, which proven better results than feed-forward logic control in the hub. In our present

case of study, considering the dimensions of OKEANOS' sail and that its operation takes place in a low solar radiation pressure environment, thrusting has been chosen above the former control. Despite thrusters not being fuel-free, they provide a control with the possibility of a much faster response of the system, as well as a higher reliability, as RCD were found to have a short life period in outer space during IKAROS demonstration.

During this study, it will be also analysed the impact of the bending moment on the dynamics of the sail. A control method that does not get affected up to a great measure by that parameter is desirable, as the actual value of the bending stiffness of the sail is unknown.

The simulation parameters are the same as in 2, excepting the torque-related ones, which are displayed below:

Table 3: Thrusting Parameters

Thruster Settings		
Number	4	
X Position	[20.3, -20.3, -20.3, 20.3]	[m]
Y Position	[20.3, 20.3, -20.3, -20.3]	[m]
Thrust F	5; 10; 20	[N]
Thrusting sign	[1, 1, -1, -1]	
$\Delta\theta$	0.5; 1.5; 3	[deg]

The value of 5 N of the thrusting force has been taken according to design conditions. The values of 10 and 20 N, however, obey academic reasons, since they are high enough as not to be feasible but the dynamics arising in the sail when such input is applied are considered of interest.

The thrusting time Δt is calculated from the following expression before every firing:

$$\Delta t = \Delta\theta \frac{I_{ZZ}\Omega}{4F\bar{X}_b} \tag{79}$$

where $\bar{X}_b$ is the relative position between the tip mass and the centre of mass of the main body in local coordinates.

In order to get a more realistic simulation, the direction of the force is chosen to be that of the positive normal vector formed by the plane compressed between each of the tip masses and the two elements of the membrane to which it is attached.

5.2 Bending Moment Analysis during Rhumb-Line Maneuver

5.2.1 $\Delta\theta = 0.5$ deg and $|F| = 5$ N Simulation Results

According to Equation 79, and substituting the sail parameters, it gives a value of $\Delta t = 0.11026$ s, the smallest considered in the present document.

The results for both cases $K = K_{beam}$ and $K = 1 \times 10^{-2}$ are displayed in Figure 40 and Figure 41, respectively.
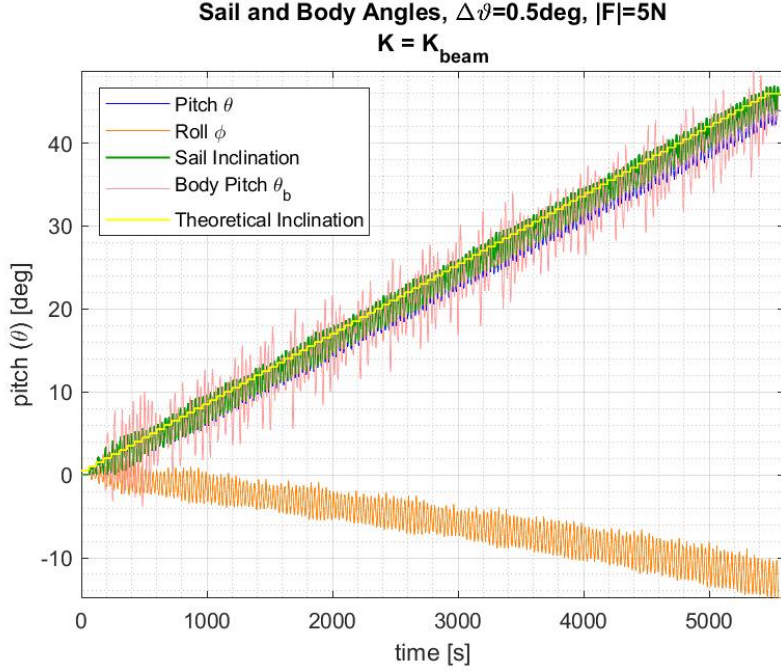
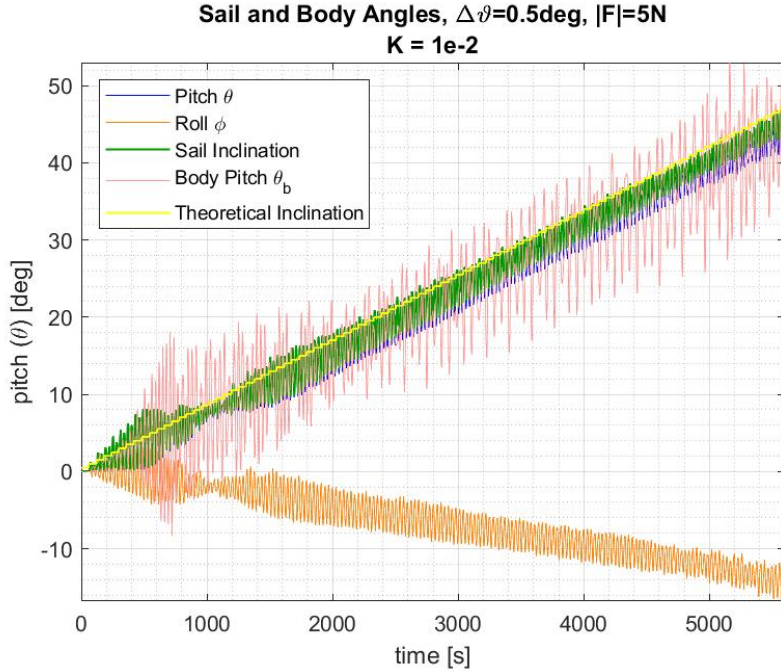Figure 40: Body Pitch, Sail Inclination, Pitch and Roll for $K = K_{beam}$.

Figure 41: Body Pitch, Sail Inclination, Pitch and Roll for $K = 1 \times 10^{-2}$.

Here, body pitch θ_b stands for the Pitch angle from the Tait-Bryan angles definition of the hub of the sail. Pitch θ and roll ϕ are the ones obtained considering the averaged normal vector to all the elements of the sail and the inertial coordinate system, and the inclination of the sail is the angle between the inertial z-axis and the aforementioned vector.

Both cases seem to present a similar behaviour, with both pitch and sail inclination overlapping themselves, although pitch is kept slightly below due to the presence of a roll angle. Ideally, if the thrusters fired perpendicularly to the sail plane, the roll angle should have been kept zero. However, the firing direction depends on the position of the tip masses in the moment of the injection and, thus, a little divergence from the ideal firing position gets to the apparition of undesired attitude. Besides, Δt, although being little, is not infinitesimal, so pure torque along the x-axis is not obtained.

40

Also, the pitch angle of the hub presents a stronger oscillation in Figure 41, as being a highly rigid membrane, the motion is better transmitted from the outermost part of the sail to the inner body.

It is worth mentioning that the sail inclination and pitch angle change their values accordingly to the expected values from Equation 79, where the following relative errors are observed:
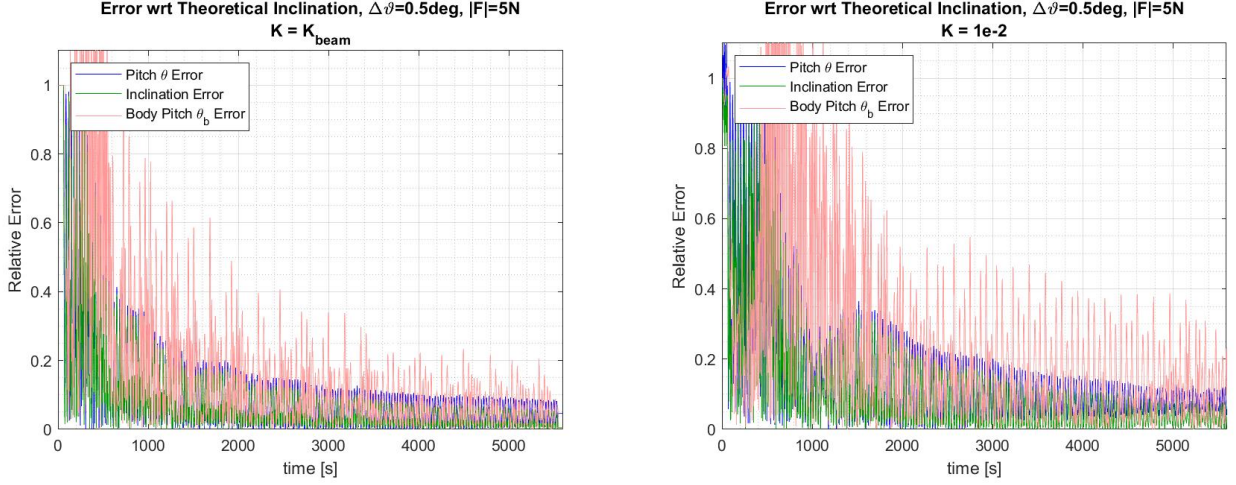

(a) $K = K_{beam}$.   (b) $K = 1 \times 10^{-2}$.

Figure 42: Relative error between theoretical and expected pitch angle, and inclination of the sail.

It can be seen that for both graphs the error is kept below 10% for both the inclination angle and the pitch angle, although the first one being lower. When comparing with the error observed in Figure 28, corresponding to the in-body thrusting, it is noticeable that it has been reduced more than a third of its value. Then, applying the thrust directly on the membrane eliminates the losses of the hub-sail connection, and the performance of the method is almost the theoretically obtained one regardless of the flexibility of the membrane.

For the case presented in this subsection, the difference in both the pitch angles of the sail due to the effect of the bending stiffness are presented for a wide range of bending constants:
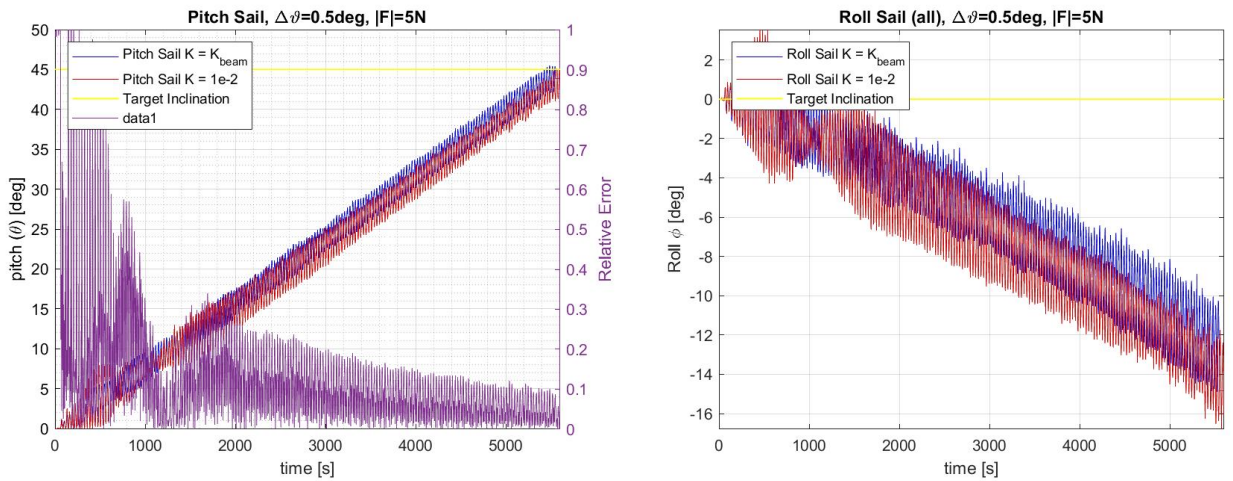
(a) Pitch angle.   (b) Roll angle.

Figure 43: Comparison between the pitch and roll angles for the $K = K_{beam}$ and $K = 1 \times 10^{-2}$ cases.

The difference between the pitch angles of both sails is kept below 10% during the last stages of the maneuver, which is far lower than in the in-body thrusting case. As for the roll angle, a higher difference

arises. That difference is generated by the actual direction of the thrusting force in every one of the cases studied. Different bending moments affect the layout and particle position of the sail, as seen in Figure **??**. Higher angular differences are translated into different thrusting vector orientations, which, at its turn, leads to different torque contributions and, therefore, different values of the undesired roll angle in detriment of the pitch.

As for the inclination of the sail, unaffected by the roll angle, all the simulations for the different values of the bending stiffness are presented:
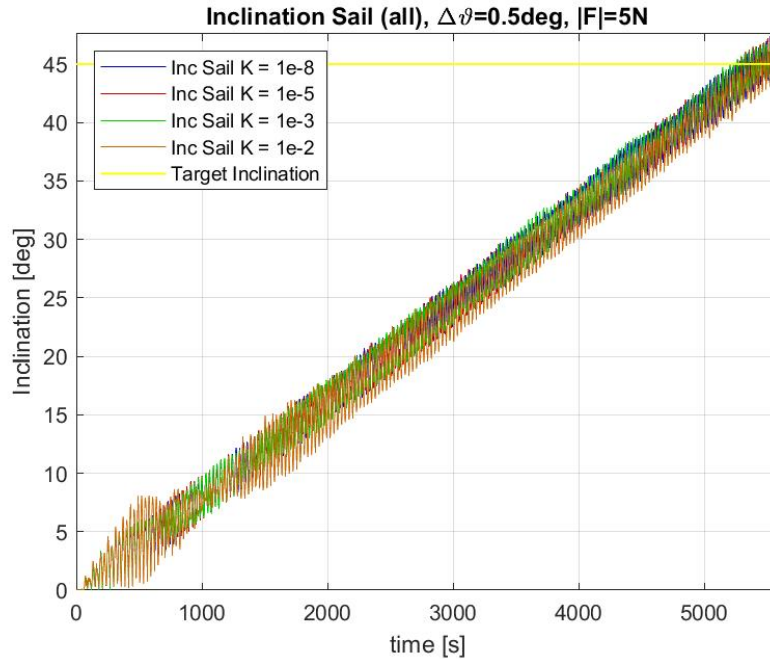

Figure 44: Sail Inclination, for all bending cases considered.

The attitude motion of the sail remains almost unaffected by the bending stiffness when using the tip-mass thrusting control system, as seen in Figure 44, important advantage of the tip-thrusting control with respect to the in-body control due to the fact that the actual bending parameter of the sail remains as an unknown and, therefore, a control method which can make the sail behave the same independently of its bending constant is needed. It is necessary to point out that the inclination angle presents a major hegemony than the pitch one. That is because of differences arising in regards to the roll angle affect the value of the pitch, but not the overall inclination of the sail.

5.2.1.1 Nutation

Regarding the oscillations of the hub, the following plots concerning the nutation of the probe are also added.

As it could be inferred from comparing Figures 40 and 41, the angular velocity of the body of the spacecraft gets up to higher values for the case of a higher bending stiffness. As commented previously, it happens most probably because a higher rigidity helps to transmit the vibrations to the hub. However, in both cases the values are far lower the ones got from the in-body thrusting. That had a direct effect in the reduction on the error of the pitch angle of the hub shown in Figure 42, where high oscillations are specially unwanted due to the fact that the sensors of the satellite are placed there.
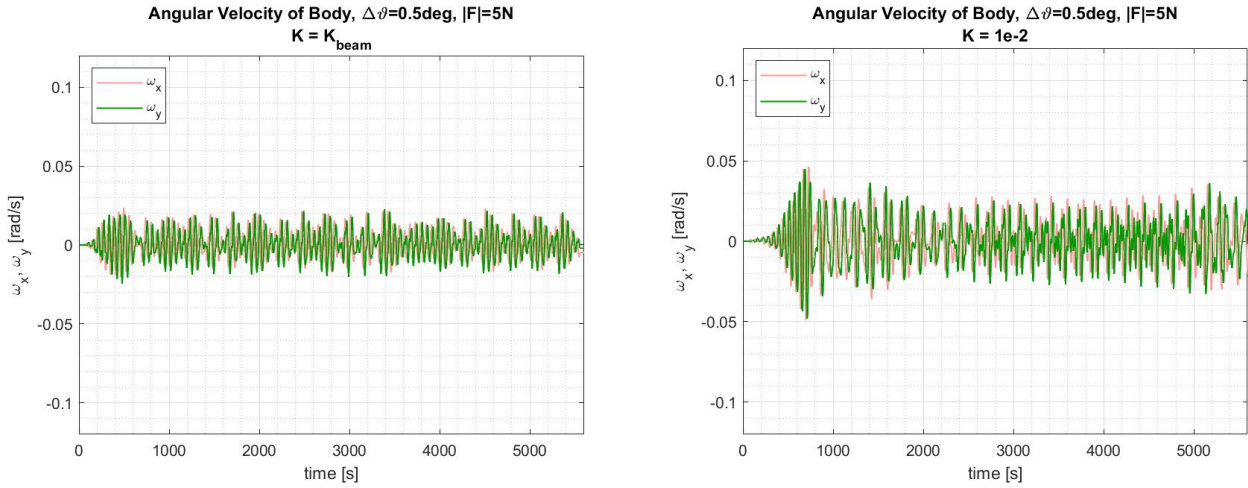
(a) $K = K_{beam}$.   (b) $K = 1 \times 10^{-2}$.

Figure 45: ω_x and ω_y of the hub for $\Delta\theta = 0.5$ deg, $|F| = 5$ N.

In the following subsections, the thrusting force and the firing time values are to be increased so as to see whether a faster maneuver has a toll in its performance.

5.2.2 $\Delta\theta = 1.5$ deg and $|F| = 10$ N Simulation Results

For the $\Delta\theta$ and thrust magnitude here considered, $\Delta t = 0.16539$ s is obtained for the non-perturbed sail configuration, which is approximately 1.5 times higher than the one in the previous simulations.

Again, cases $K = K_{beam}$ and $K = 1 \times 10^{-2}$ are to be shown in separate plots because of the relevance of the values that the bending parameter takes. These plots can be seen below:
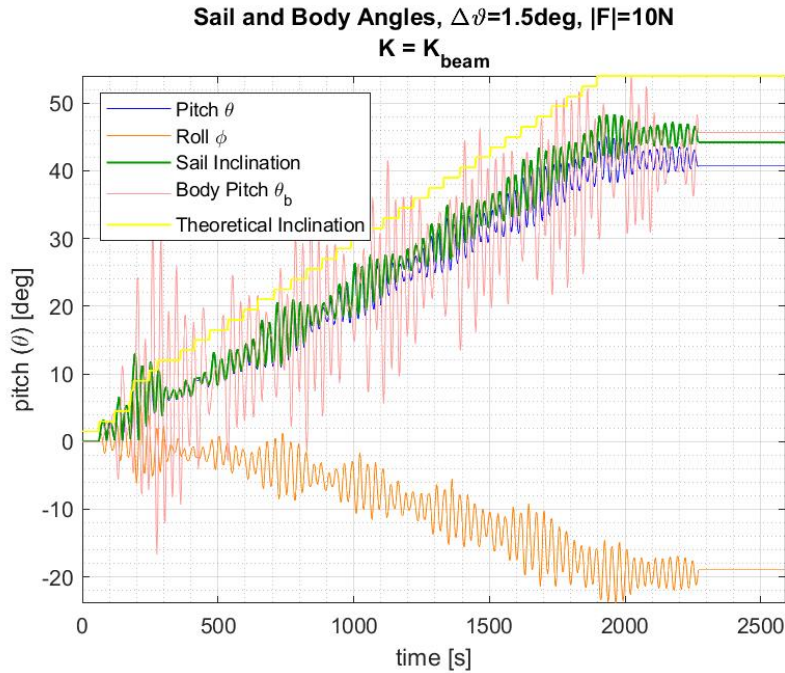

Figure 46: Body Pitch, Sail Inclination, Pitch and Roll for $K = K_{beam}$.
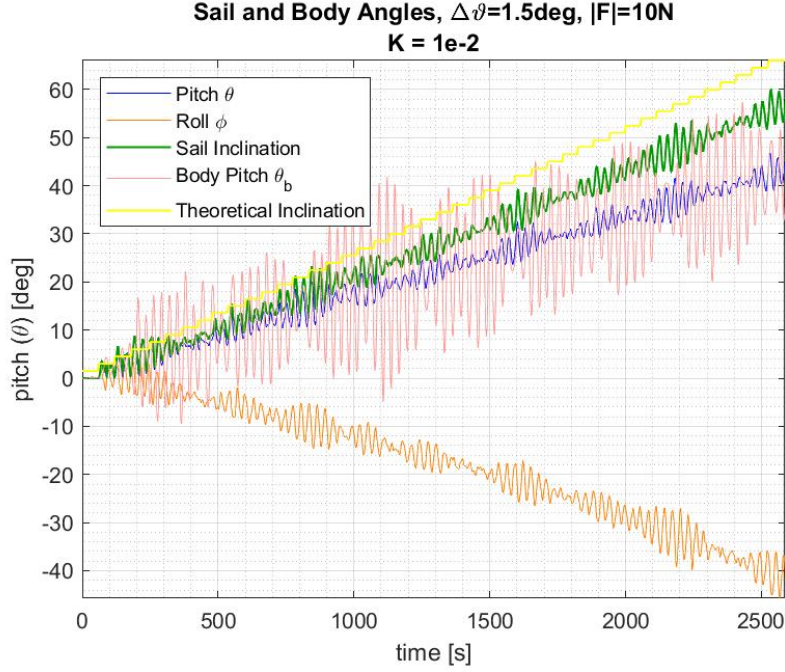
Figure 47: Body Pitch, Sail Inclination, Pitch and Roll for $K = 1 \times 10^{-2}$.

The increase on Δt and the thrusting force have proven to have negative effects over the performance of the spin axis reorientation maneuver. A longer Δt is translated to getting higher undesired torque components, which result in larger roll angles. The lowered change on both sail inclination and pitch angles when compared to the theoretical expectations, can be both explained from the fact that part of the momentum given is used on giving a change to the roll angle of the sail and that a higher thrusting force applied to the tip-masses makes their movement rougher, and provided that the direction of the force depends directly on the position of the masses, the desired torque that would be obtained from a firing in the same direction sees its value lowered from the differences between positions.

The error, consequently, has been increased, although the one corresponding to the inclination of the sail remains at acceptable values because is not affected by the higher roll.
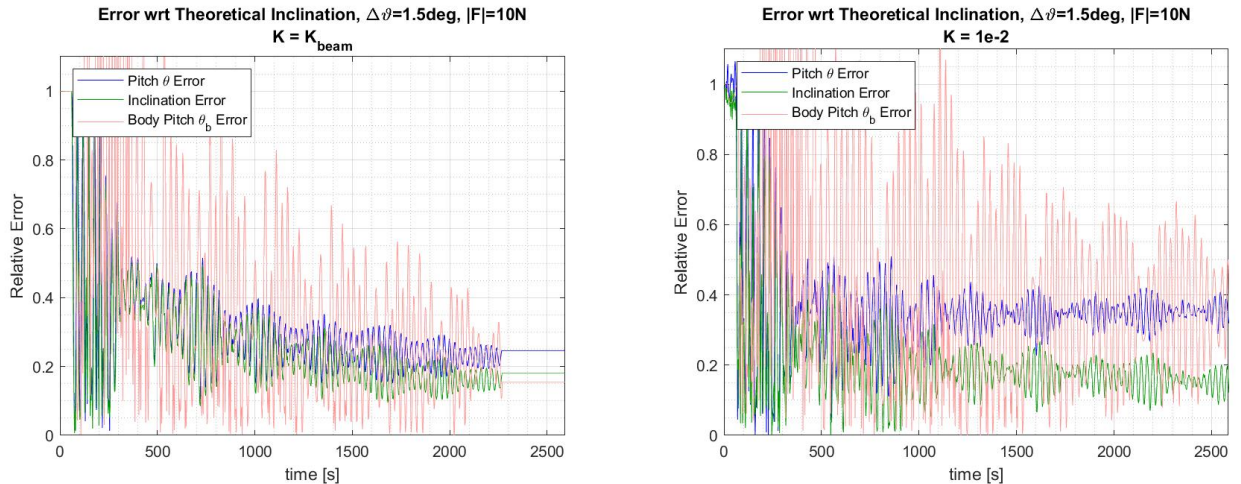
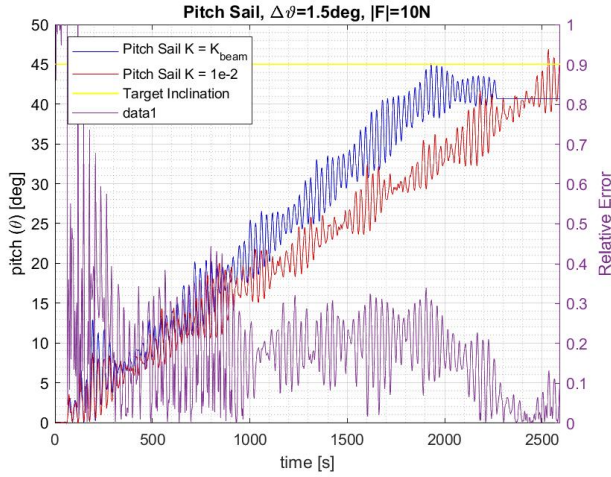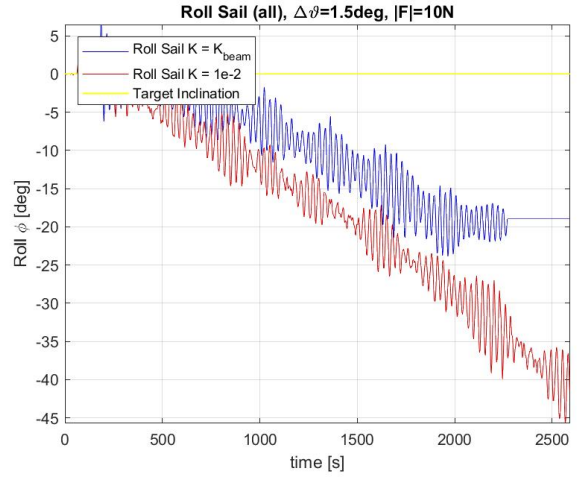(a) $K = K_{beam}$.

(b) $K = 1 \times 10^{-2}$.

Figure 48: Relative error between theoretical and expected pitch angle, and inclination of the sail.

While the pitch error differs greatly between both cases, the inclination one does remain the same regardless of the bending stiffness. That phenomenon is easily explained when comparing both the pitch and roll angles of the two cases above:

44

(a) Pitch angle.

(b) Roll angle.

Figure 49: Comparison between the pitch and roll angles for the $K = K_{beam}$ and $K = 1 \times 10^{-2}$ cases.

As it happened in the $\Delta\theta = 0.5$ deg and $|F| = 5$ N simulations, the roll angle gets higher in magnitude for the higher bending stiffness case, as the rigidity of the membrane causes the apparition of marked creases and valleys that affect in a greater magnitude the direction of the thrust make undesired torque components to appear more frequently. That induces a higher roll angle at expenses of the pitch one. Of course, the maneuver does not stop until the pitch angle reaches the objective value, so the roll angle keeps increasing in consequence in the $K = 1 \times 10^{-2}$ case even after the maneuver for the $K = K_{beam}$ has ended.

The plots containing all the bending cases studied are shown in the following figures:
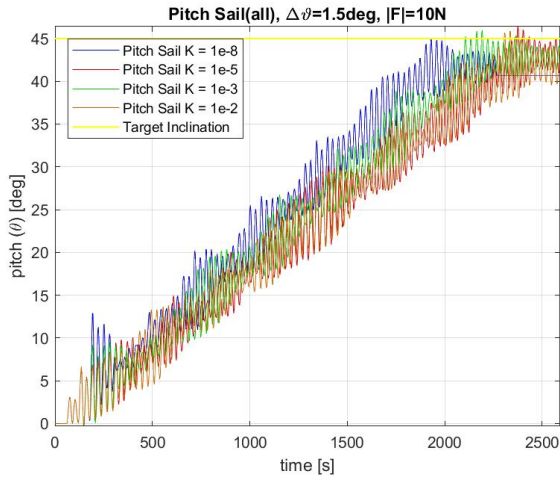
(a) Sail Pitch, for all bending cases considered.
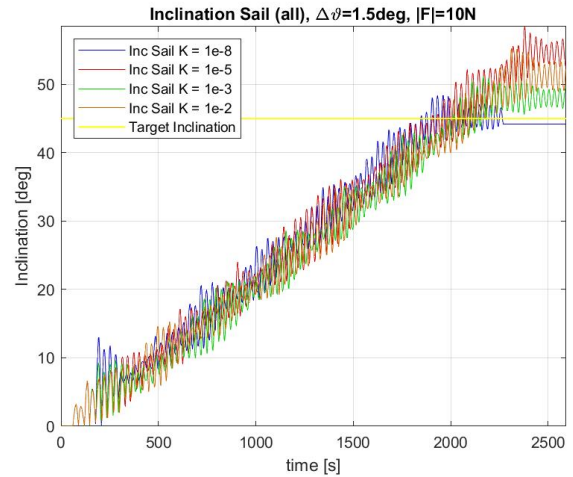
(b) Sail Inclination, for all bending cases considered.

Figure 50: Comparison between the pitch and inclination angles for all bending cases considered.

As expected from the previous simulations, the inclination of the sail reaches the desired value before the pitch angle, as the former accounts also for a component that comes from the roll angle, which in these last cases was seen to be high. Considering the differences between the responses depending on the bending constant, there are none when focusing on the inclination. For the pitch angle, a higher bending moment results in a slightly lower increment rate, due to the fact that a higher roll angle is obtained. However, the difference is not significant and is almost negligible considering that the differences between the bending constants comprise six orders of magnitude.

45

5.2.2.1 Nutation

The nutation arising in the hub is as follows:

(a) $K = K_{beam}$. (b) $K = 1 \times 10^{-2}$.
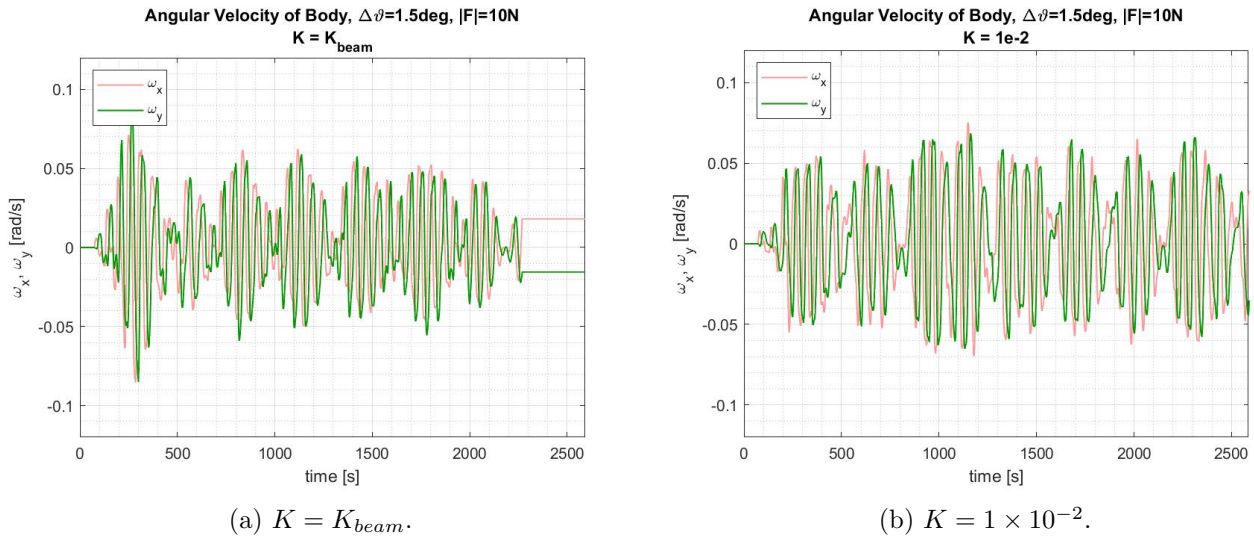
Figure 51: ω_x and ω_y of the hub for $\Delta\theta = 1.5$ deg, $|F| = 10$ N.

Here the same that happened in Figure 45 is observed, only that this time the magnitude of the oscillations are higher, as the input force has doubled. However, the oscillations are still lower than in the in-body thrusting case, although the torque generated is far higher.

5.2.3 $\Delta\theta = 3.0$ deg and $|F| = 30$ N Simulation Results

In this case, Δt is kept the same as in the previous simulations, but both the $\Delta\theta$ and the magnitude of the thrusting input have been doubled.

The results obtained are the ones here presented:

Figure 52: Body Pitch, Sail Inclination, Pitch and Roll for $K = K_{beam}$.

Figure 53: Body Pitch, Sail Inclination, Pitch and Roll for $K = 1 \times 10^{-2}$.

As it happened before, the inclination change is below the theoretical ratio, and a high roll angle makes again its apparition. Howeve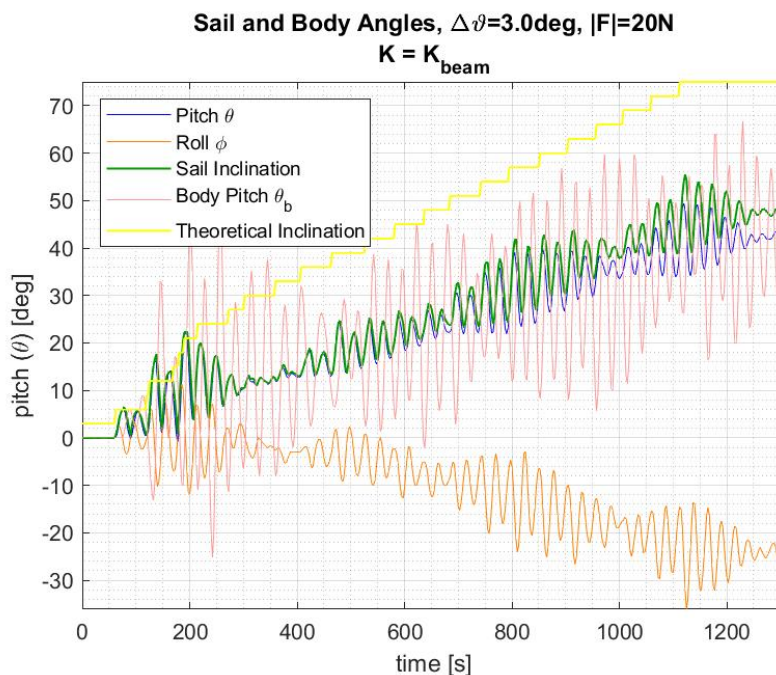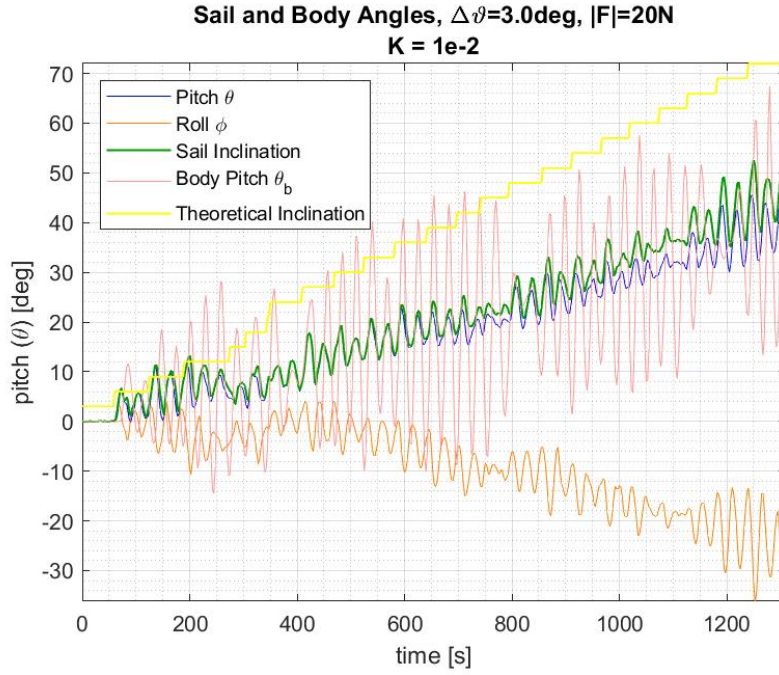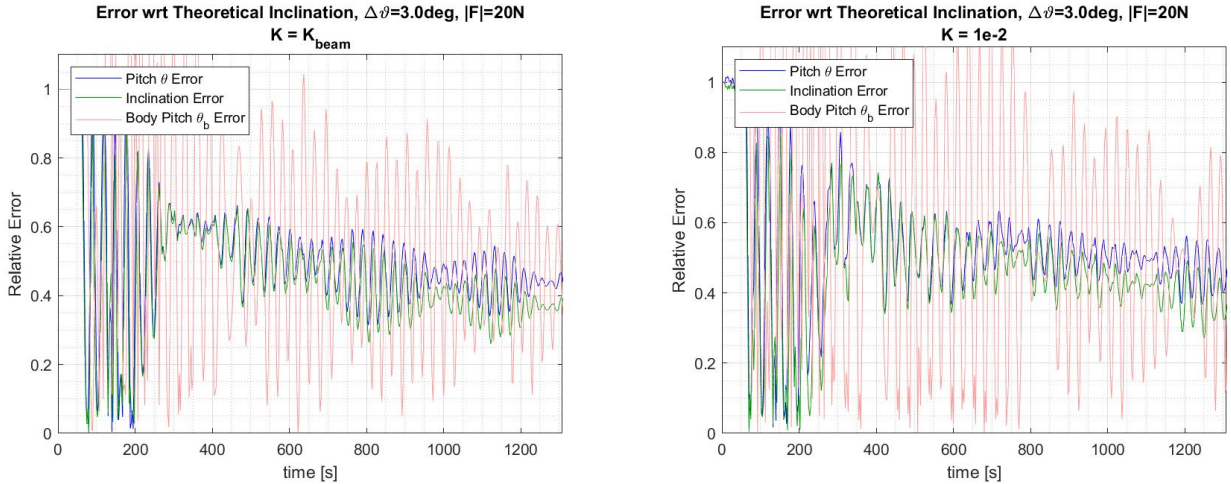r, despite Δt has not changed, the performance lowered. As said above, the higher the thrusting force, the more the tip-masses oscillate, and brusque changes in their position might result in orientations of the force vector that generate counteracting torques, obtaining then a lower angular change than predicted.

Taking a closer look to the relative error:

(a) $K = K_{beam}$.

(b) $K = 1 \times 10^{-2}$.

Figure 54: Relative error between theoretical and expected pitch angle, and inclination of the sail.

The performance of the maneuver has plummeted, leading to errors of around $40 - 45\%$ for both the inclination and the pitch angles. The oscillation of the membrane angles as well as the hub ones has also increased, although the ones for the hub remain a bit lower than for the in-body thrust. The similarity between the pitch and inclination angle values happens because this time the roll angle obtained is lower, as the main performance problem of this case is not the generation of undesired torque components anymore, but the generation of opposing forces and torques due to the high oscillation of the tip-masses because of the magnitude of the force applied.

47

For the graph superposing the different results, in this case only the $K = K_{beam}$ and $K = 1 \times 10^{-2}$ have been considered, as only these simulations were performed.
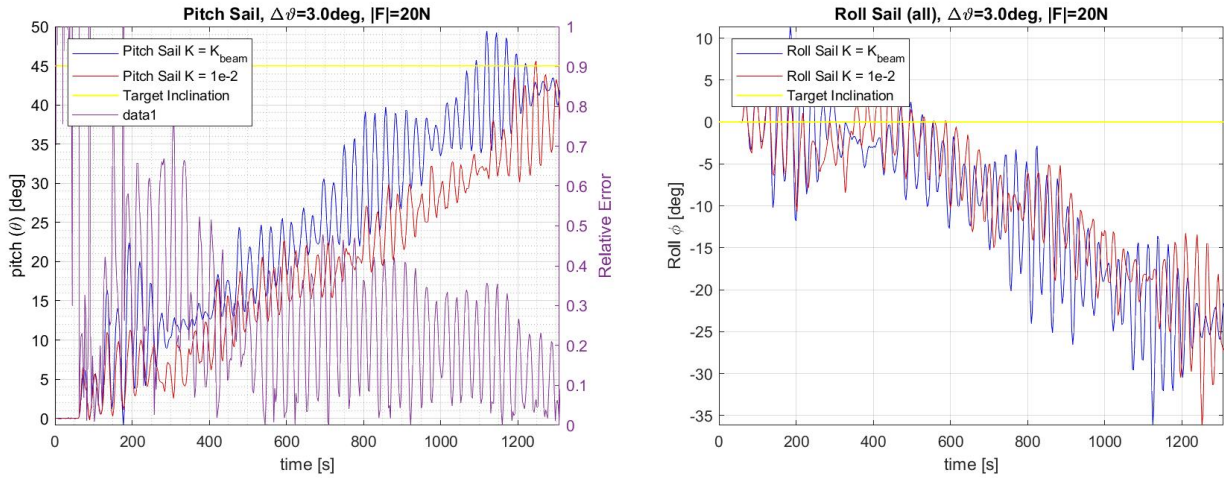
(a) Sail Pitch, for all bending cases considered.

(b) Sail Inclination, for all bending cases considered.

Figure 55: Comparison between the pitch and inclination angles for all bending cases considered.

This time, the difference from considering various bending stiffnesses is more remarkable, getting a better response for the more flexible membrane, although bad nonetheless.

5.2.3.1 Nutation

Even though the hub is connected to the main body of the sail by tethers and its position is the furthest from the thrusters, its nutation motion gets highly affected from a change in magnitude of the input force. The changes in the oscillation of its pitch value observed during the previous subsections goes in consonance with the results here present, showing an increment on the magnitude of the angular velocity in X and Y axis (non-inertial frame) of about four times between the first and last simulations.
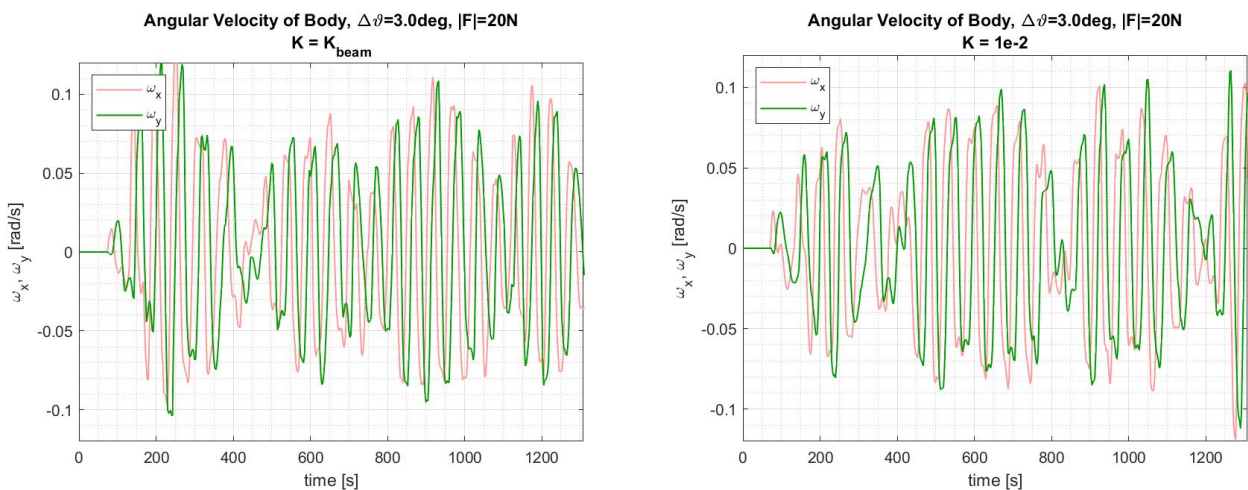
(a) $K = K_{beam}$.

(b) $K = 1 \times 10^{-2}$.

Figure 56: ω_x and ω_y of the hub for $\Delta\theta = 3.0$ deg, $|F| = 20$ N.

Therefore, it has been observed that not only is better in terms of performance, but also that the smaller the torque and the injection time, the better the stability.

5.3 Frequency analysis on the response of the membrane due to tip-mass thrusting

As it was done in Section 4.3, the response of the sail to the control input will be studied on the frequency domain via Fast Fourier Transform (FFT). During the analysis, a dimensionless frequency $\hat{\omega} = \omega/\Omega$ is considered, being Ω the spin rate.

Only the results for the $K = K_{beam}$ and $K = 1 \times 10^{-2}$ bending stiffness parameter values will be shown, being the first representative for the flexible case, that being from $K = 1 \times 10^{-8}$ to $K = 1 \times 10^{-3}$.

5.3.1 $\Delta\theta = 0.5$ deg and $|F| = 5$ N Frequency Response

In the figures below, the single-sided amplitude spectrum for the FFT of the out-of-plane displacement of the nodes is displayed. As in the previous analysis, the plane of the sail has been considered to be the plane whose normal vector is that obtaining from adding up all the normal vectors of each triangular element that comprises the sail in the Multi-Particle Model, and that comprises the non-inertial origin of coordinates, that is, the center of the hub.
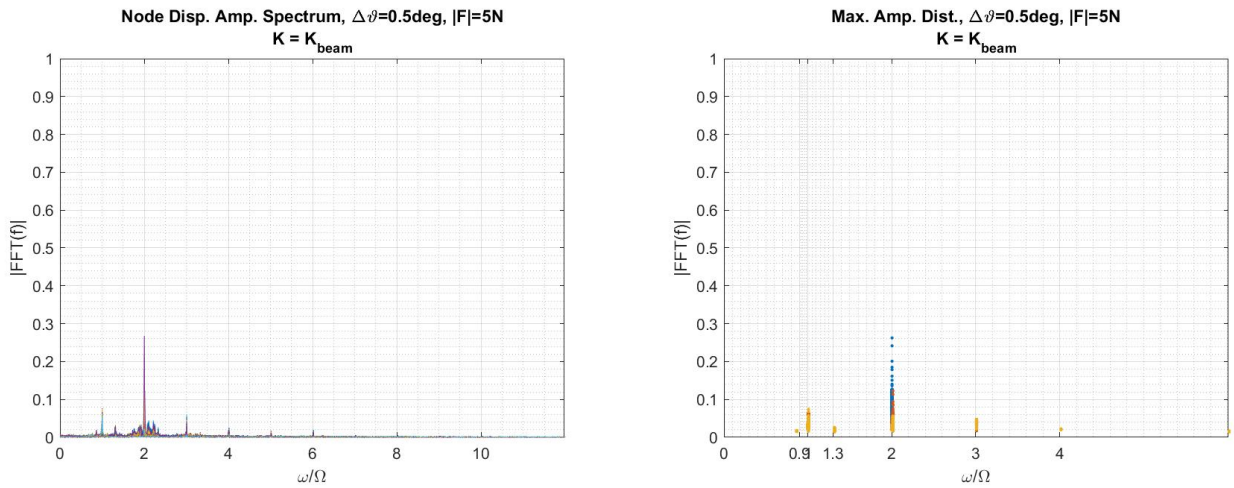
(a) Amplitude spectrum for particle displacement, $K = K_{beam}$.

(b) Frequency distribution in nodes along the sail, $K = K_{beam}$.

Figure 57: Frequency analysis by means of FFT for $K = K_{beam}$.
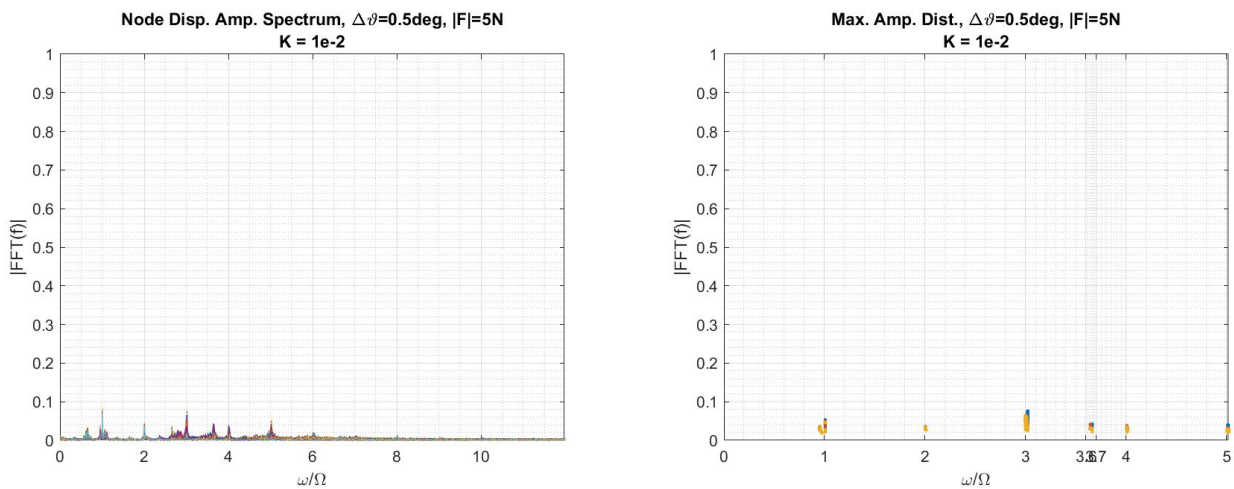
(a) Amplitude spectrum for particle displacement, $K = 1 \times 10^{-2}$.

(b) Frequency distribution in nodes along the sail, $K = 1 \times 10^{-2}$.

Figure 58: Frequency analysis by means of FFT for $K = 1 \times 10^{-2}$.

It is clearly seen in Figure 57 how there is a clear peak in $\hat{\omega} = 2$. Smaller peaks seem to be found also in $\hat{\omega} = 1$ and $\hat{\omega} = 3$, although their amplitude is far smaller.

In Figure 58, those very same peaks could be inferred, but the low amplitude could make one mistake them as mere noise fluctuations. Also, when comparing with the left hand graph in Figure **??**, the peak placed in $\hat{\omega} = 2$ has lost its dominance above the rest.

In the right hand side plot, the frequencies at which a maximum of amplitude has been observed in every node has been plotted for the three most prominent ones, in blue, red and yellow from higher magnitudes to lower, respectively for each node. The higher the density of points, the greater the number of nodes which present an excitation at such frequency.

Taking back Equation 78, the natural frequencies for a membrane without taking bending stiffness into account obtained:

Representing them in Figure **??**:
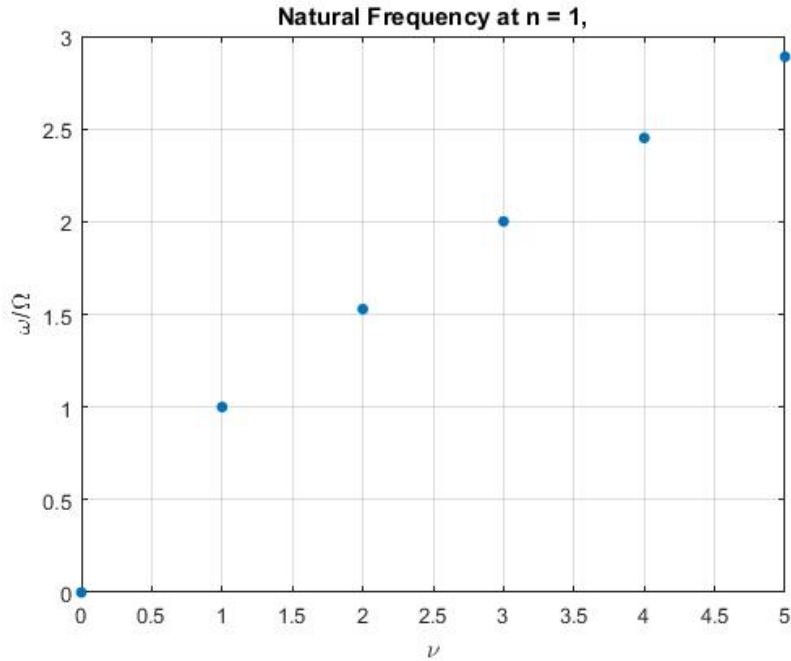
Figure 59: $\hat{\omega}$ at $n = 1$.

Comparing with Section 4.3, when applying the forces directly over the membrane higher circumferential modes are excited for the $K = K_{beam}$ case, whereas the intensity of the torque impulse for the case $K = 1 \times 10^{-2}$ seems not to be enough to cause a bigger amplitude excitation, probably due to the less flexible nature of the membrane.

5.3.2 $\Delta\theta = 1.5$ **deg and** $|F| = 10$ **N Simulation Results**

The same as in the previous subsection has been done for this case. The thrusting input is also applied once per spin rate, which would mean a $\hat{\omega}_{thrust} = 1$. The difference with the previous simulation is the magnitude of the thrust and the thrusting time, both higher.

The single-sided FFT obtained is as follows:
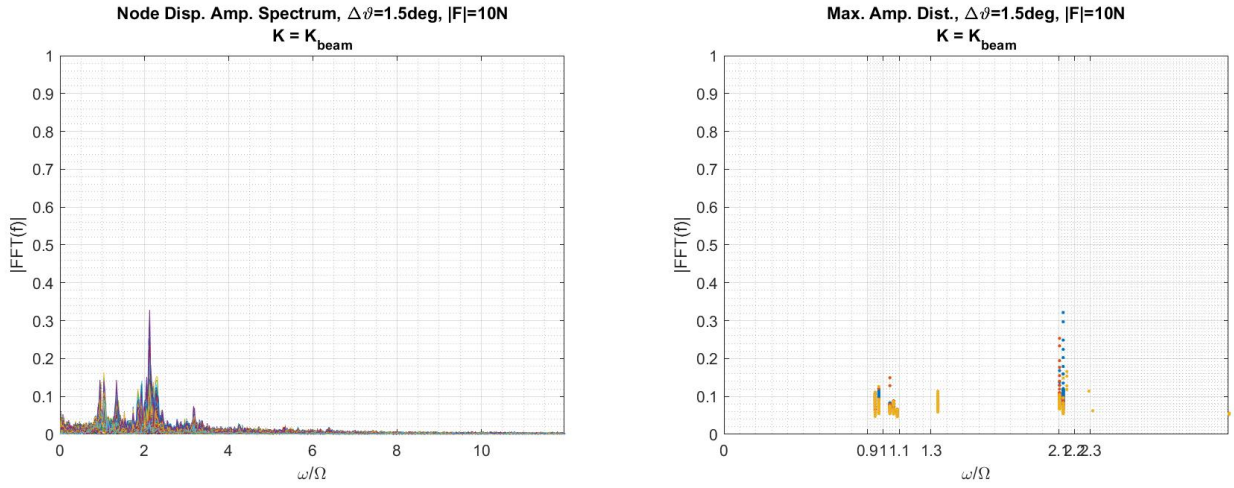
(a) Amplitude spectrum for particle displacement, $K =$ (b) Frequency distribution in nodes along the sail, $K = K_{beam}$.
K_{beam}.

Figure 60: Frequency analysis by means of FFT for $K = K_{beam}$.

(a) Amplitude spectrum for particle displacement, $K =$ (b) Frequency distribution in nodes along the sail, $K = 1 \times 10^{-2}$.
1×10^{-2}.

Figure 61: Frequency analysis by means of FFT for $K = 1 \times 10^{-2}$.
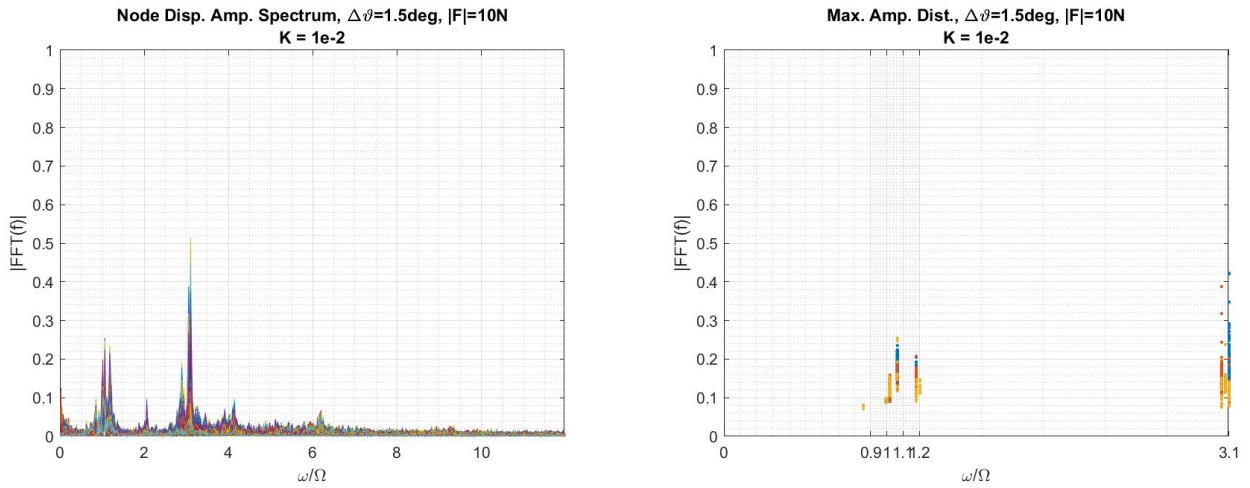
In Figure 60, the peak in $\hat{\omega} = 2$ is still dominant, and both that one and peaks around $\hat{\omega} = 1$ have gained intensity when applying a higher force over the membrane.

For the $K = 1 \times 10^{-2}$ case, it seems that the higher force applied over the membrane is enough to make the nodes excited. Here, however, the dominant peak is placed in $\hat{\omega} = 3$ and, although peaks around $\hat{\omega} = 1$ do also appear, there is no excitation in $\hat{\omega} = 2$.

The increment in nodes vibrating around the input force frequency happens because of its increase in magnitude. Is important to observe the different spectrum based on the bending stiffness of the membrane. In Figure 61, higher circumferential orders get excited at the same time that some lower frequencies are skipped.

5.3.3 $\Delta\theta = 3.0$ deg and $|F| = 20$ N Simulation Results

Finally, the spectrum in frequency for the last of the control system configurations is presented. With respect to the previous subsection, the thrusting force has been doubled, but the input time has not been modified. The FFT results in the plots presented in Figures 62 and 63.

(a) Amplitude spectrum for particle displacement, $K = K_{beam}$.

(b) Frequency distribution in nodes along the sail, $K = K_{beam}$.

Figure 62: Frequency analysis by means of FFT for $K = K_{beam}$.

(a) Amplitude spectrum for particle displacement, $K = 1 \times 10^{-2}$.

(b) Frequency distribution in nodes along the sail, $K = 1 \times 10^{-2}$.

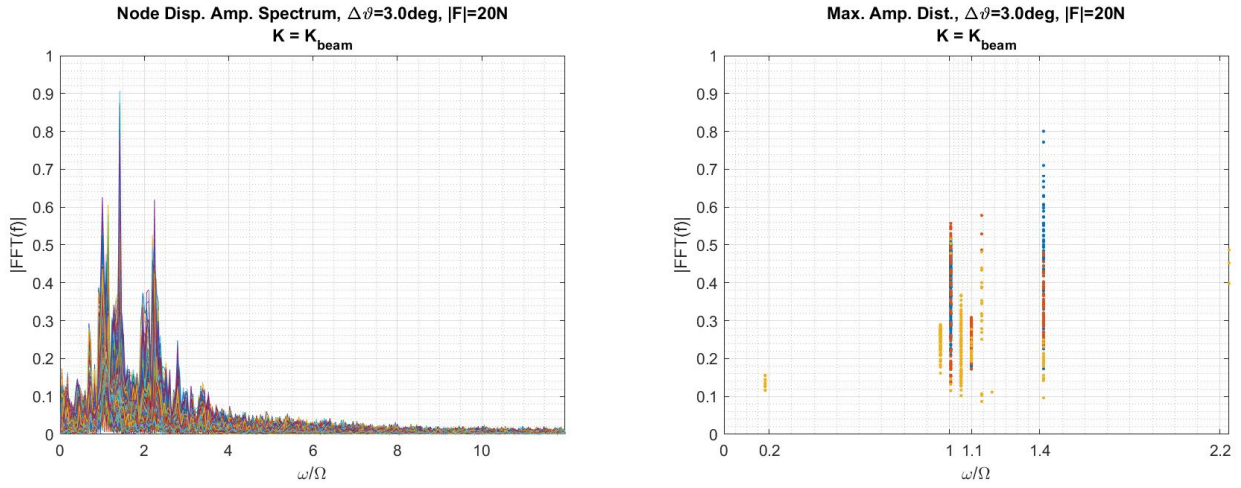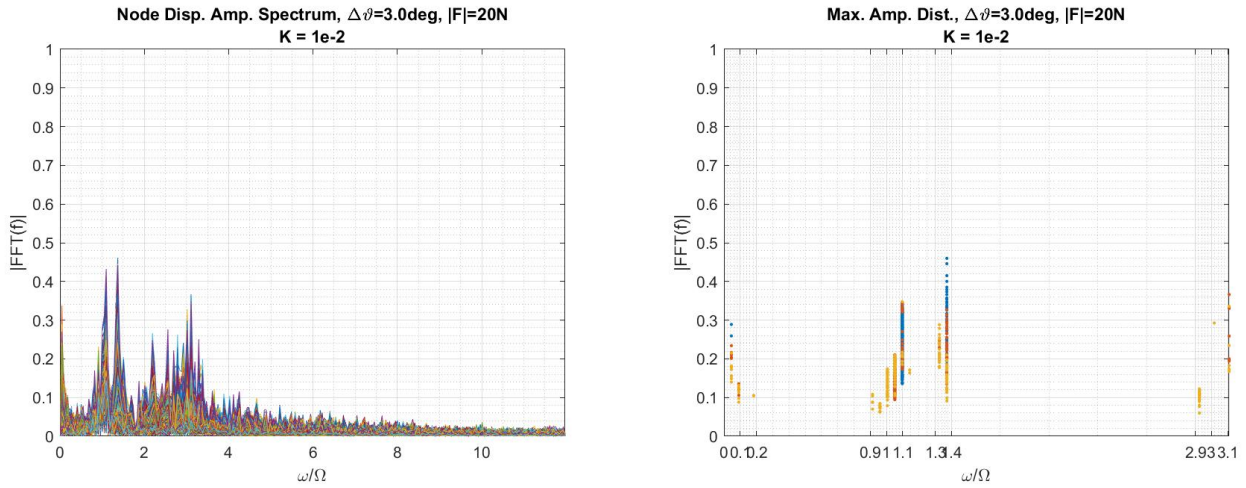Figure 63: Frequency analysis by means of FFT for $K = 1 \times 10^{-2}$.

The vibrations continue with the trend observed until this point, concentrating around $\hat{\omega} = 1$ while the input thrusting augments. Comparing with the previous case and taking into account the performance of the reorientation maneuver, it is seen that higher vibrations arising on the membrane lead to a lower response to the control input. Also, higher excitation frequencies affect more negatively the change of the spin axis.

5.4 Insights

In Section 4.2, the results for a control system based on thrusting impulses on the hub were displayed,

It can be seen how in that first control method the performance is lower than the theoretical increment in inclination. In Figure 30, the pitch angle of the hub is shown to oscillate at a higher amplitude than the third case considered in the tip-mass thrusting, which was the most unfavorable one.

In Figure 29, however, the roll angle of the sail is kept around zero, which is more desirable than the variations occurring in all tip-mass thrusting cases. However, when considering body thrusters, the implementation of the impulse was set such that the torque generated always pointed to the positive

direction of the X-axis (non-inertial). In the latest simulations done, the direction is not fixed anymore in order to give a more realistic approach, so not getting a unidirectional torque and obtaining undesired components which give a high roll angle is to be expected. However, the control algorithm should be improved in the future so as to prevent that.

In the following table, the maneuver time required for all cases has been collected:

Table 4: Maneuver Comparison

Maneuver Time for $K = K\_bend$				
Simulation	**t [s]**	**Pitch [deg]**	$\lvert Roll \rvert$ **[deg]**	$\lvert \omega_{x,y} \rvert$
0.5 deg, 5 N	5482.5	$>= 45$	< 15	< 0.3
1.5 deg, 10 N	1930	$>= 45$	< 25	< 0.6
3.0 deg, 20 N	1147.5	$>= 45$	< 35	< 0.12
Body Th. 20 N	6327.5	< 29	< 8	< 0.12

Maneuver Time for $K = 1 \times e - 2$				
Simulation	**t [s]**	**Pitch [deg]**	$\lvert Roll \rvert$ **[deg]**	$\lvert \omega_{x,y} \rvert$
0.5 deg, 5 N	5570	$>= 45$	< 17	< 0.5
1.5 deg, 10 N	2532.5	$>= 45$	< 45	< 0.7
3.0 deg, 20 N	1250	$>= 45$	< 35	< 0.12
Body Th. 20 N	6327.5	< 34	< 7	< 0.12

As seen in Table 4, even using a high thrusting, the control through body thrusters acquires the lowest angle in the longest time as well as causing the biggest nutation in the hub. The torque generated in the in-body thrusting case is around 0.8 of the $\Delta\theta = 0.5$ deg and $\lvert F \rvert = 5$ case, so is expected for it to take more time. However, a force of 20 N is still required, which is translated in a higher fuel consumption to perform the same maneuver in a slower and by far worse, in terms of performance, way. It should be added also that despite tip-mass thrusting performs the same regardless of the bending stiffness for the first two forces considered, when using body-thrusting, the sail attitude is affected up to a high extent depending on the bending parameter, being that undesired considering it is unknown.

In conclusion, a control system able to change the sail attitude successfully regardless of its out-of-plane stiffness has been found. Still, some problems as the nutation arising and the presence of an undesired roll angle are still to be solved by implementing a more robust control algorithm and an active nutation control logic.

Finally, the out-of-plane vibration of the particles along the sail is considered. Differently from the previous report, applying a force directly on the membrane excites higher vibration modes. At lower forced inputs, for the higher bending stiffness case, no mode can be excited at a significant amplitude. However, as the applied force grows in magnitude, most of the modes of the sail get excited at the forced frequency, in this case, $\hat{\omega} = 1$.

Big differences between the higher bending and the cantilever approximation cases have been found when doing the frequency analysis. Contrary from Section 4.3, the excitation of different circumferential nodes in every case has been observed. Besides, the higher the vibrations arising, the worse the performance. It also seems that higher circumferential nodes have a major contribution regarding the negative effects in the reorientation.

6 Roll Control

In Section 5, the new control system by means of thrusters present in the tip masses was observed to perform in a much better way than the in-body thrusting. However, the apparition of an undesired roll angle of great magnitude and the high detriment of its performance when incrementing the thrusting input are important flaws of the tip-mass thrusting that should be corrected. Therefore, in this section, an improved control algorithm will be proposed so as to solve the aforementioned problems.

6.1 Control Algorithm

Here below, the algorithm for the new control implemented is displayed. A detailed explanation of the Algorithm 2 is included afterwards.

Algorithm 2: Rhumb-Line Maneuver with Roll Control

Input: inertial sun vector, initial attitude
Output: final attitude
  Initialisation :
  while $t <$*simulation time* **do**
    Calculate sun vector in satellite coordinates
    if (*y-coord sun vector switches sign*) **and** (*x-coord < 0*) **then**
      Sun-pulse occurs $\implies$ *Pulse Flag* ON, $cnt = 0$, $n_{th} = 0$
      Calculate Δt, *mean* ϕ_b, t_0
      if $|mean\ \phi_b| > 0.1\pi/180$ **then**
        $t_0 \leftarrow t_{in}$
      end if
      if $|mean\ \phi_b| > \Delta\theta$ **then**
        set Δt per thruster
      end if
      reset *mean* $\phi_b = 0$
    end if
    LOOP Process
    if ($t = t_0$) **and** $n_{th} < 3$ **then**
      $\implies$ *Pulse Flag* ON, $cnt = 0$, $n_{th} + +$
      set t_0
    end if
    if (*Pulse Flag*) **and** ($cnt < \Delta t$) **then**
      Thruster On, $cnt = cnt + \delta t$
    end if
    Dynamics Calculation
    return New Attitude $\implies$ **get** ϕ_b
    if ($cnt \geq \Delta t$) **then**
      Thruster Off, *Pulse Flag* OFF
    end if
    $t = t + \delta t$
  end while

One of the main limitations to overcome for the control design was the available inputs. The actual known data are the angular velocity components of the main body and its attitude. Of course, the design characteristics of the sail are also known. However, apart from the commented available in-operation data and the sun sensor, the sail itself lacks sensors that could allow the calculation of the attitude of the membrane. Also, during the maneuver, not even the position of the mass tips would be determinable. That is why it is important to keep the hub's attitude as close as possible as the membrane one, and

therefore, to prevent it from oscillating heavily. The code, then, is kept simple without considering data that, despite would make a better control, would need of extra sensors.

The control system is to initialize at the detection of the first sun pulse. At that moment, thrusters are ready to activate during an interval Δt calculated from Equation 79, which requires of the inertia of the sail I_{ZZ}, its spin Ω and both the thrusting force F and the position of the tip-masses from the hub r_b. With exception of the spin rate, all parameters are taken from the characteristics of the sail, as the inertia and the position of the tip-masses at that instant are considered an unknown.

Knowing Ω, is possible to synchronize the time with the spin rate so as to know the angular position of the sail. Then, it is possible to set another thruster firing at a desired angular position without need for a sun pulse, that would occur at t_0:

$$t_0^0 = \frac{\pi/2}{\Omega} \tag{80}$$

As it can be inferred from Equation 80, there will be four thrusting inputs per period T every $T/4$ so as the satellite frame axis to overlap with the inertial frame ones. All four thrusters are to fire during Δt activating either the F_{+z} or F_{-z} nozzle, depending on their angular position at that instant. The thrusters placed on the first and second quadrants of the E_I are to fire upwards, while the other two are to fire downwards. That way, a torque M_x is generated, which will make the pitch θ angle of the sail to vary. The position of the thrusters, although unknown, can be determined from the spin rate and the time since the solar pulse.

At every thrusting, t_0 is recalculated by updating the spin rate for a better precision. Also, after the fourth thrusting the next one will be given again by the sun pulse, not by a chronometer.

During the period, the roll angle of the hub ϕ_b is to be recorded so as to calculate its mean value at the next sun pulse. That way, there is enough data available to start the roll control system. It is important to mention that the mean value over a period is used so as to compensate for the oscillations on this parameter.

If the mean value of ϕ_b is kept between -0.1 and $0.1°$, t_0 is recalculated again as in 80. However, if it was outside of the interval, a t_in would be added.

Considering Equation 57 and a thruster to be fired at $45°$, the difference in roll obtained with and without the t_{in} contribution is:

$$\begin{aligned}
\Delta\phi^n|_{thruster} &= \phi^n|_{t_0} - \phi^n|_{t_0 \pm t_{in}} \\
&= \left.\frac{M_y \Delta t}{I_{zz}\Omega}\right|_{t_0} - \left.\frac{M_y \Delta t}{I_{zz}\Omega}\right|_{t_0 \pm t_{in}} \\
&= \frac{r_b F_z^n \Delta t}{I_{zz}\Omega}(sin(\pi/4) - sin(\pi/4 \pm t_{in}\Omega))
\end{aligned} \tag{81}$$

Considering $t_{in}\Omega << 1$ and developing the trigonometric identities:

$$\Delta\phi^n|_{thruster} = \frac{r_b F_z^n \Delta t}{I_{zz}\Omega}(cos(\pi/4)(\pm t_{in}\Omega)) \tag{82}$$

t_{in} is, then, calculated as it follows:

$$t_{in} = sign(\phi_b|_T)\frac{|\Delta\phi^n|I_{zz}}{r_b|F_z|\Delta t cos(\pi/4)} \tag{83}$$

where $|\Delta\phi^n|$ is the angle to compensate by a single thruster at one thruster input. In this particular control algorithm, its value is $0.1°$ over a period to divide within three thrusting inputs with four thrusters firing at each.

Also, the control allows the Δt or firing time of every thruster to be readjusted if the absolute value of the mean of the ϕ_b exceeds that of the $\Delta\theta$ considered for the maneuver. If $\phi_b > \Delta\theta$, thrusters on the first and third quadrants will see their Δt multiplied by a factor 1.25, while for the thrusters on the remaining quadrants the factor will be 0.75. The very same case but exchanging the factors is to happen for $\phi_b < \Delta\theta$. This will allow correcting the $\Delta\phi$ over one period.

6.2 Bending Moment Analysis during Rhumb-Line Maneuver

Differently from the previous sections, an extra case has been studied and added for the result analysis. In [28], it was proven that a minimum weight of 5 kg for the tip-masses is required so as to deploy completely the 40 m span membrane of OKEANOS. However, up to 10 kg no limitations for its weight were found. An increased tip-mass weight increases the inertia of the sail. In addition, the centrifugal force has a main role in keeping the membrane flat. Therefore, a higher tip-mass weight is believed to lower the vibrations arising in the membrane, which would lead to a high performance in the reorientation maneuver. Also, more weight in the tip-masses can be translated into more fuel storage capability. Thus, in addition to the standard configuration as in Table 2, simulations for a tip-mass weight of 10 kg have also been done and the results obtained will be included along the first ones.

6.2.1 $\Delta\theta = 0.5$ deg and $|F| = 5$ N Simulation Results

As it has been done in Section 5.2, first the sail and body angles for each bending constant considered are presented for both tip-mass configurations mentioned above:
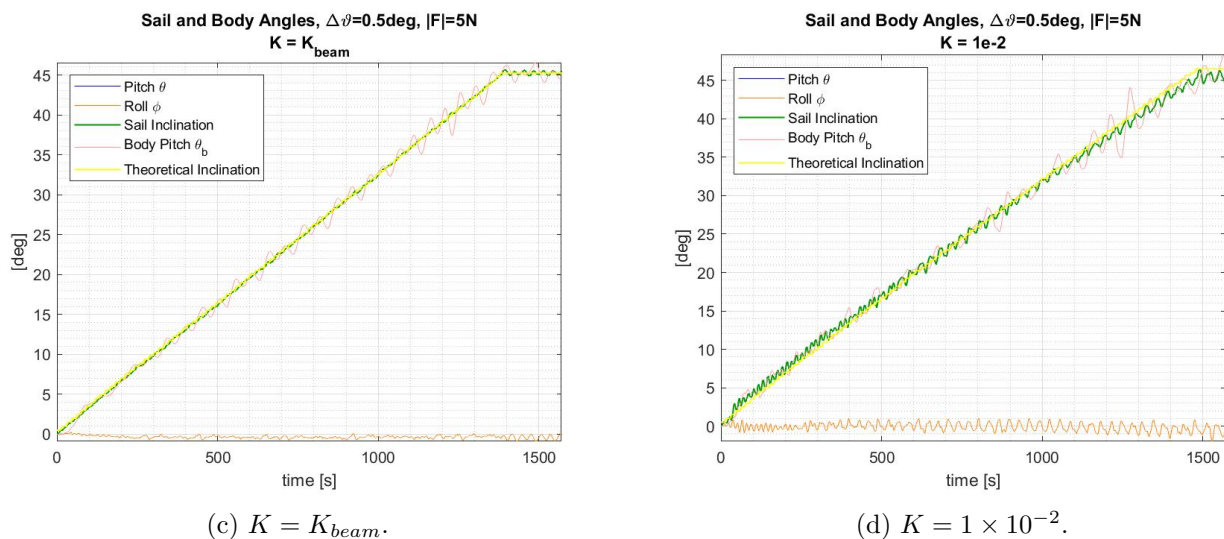

(c) $K = K_{beam}$. (d) $K = 1 \times 10^{-2}$.

Figure 64: Body Pitch, Sail Inclination, Pitch and Roll for a tip-mass weight of 5 kg.

Figure 64 supposes a significant improvement when comparing it with Figure 40 and Figure 41. For $K = K_{beam}$, the oscillations on both pitch and sail inclination angles have disappeared and their values overlap together with the theoretical inclination. As for the pitch, although some oscillations remain, their magnitude has been reduced more than by a factor of three. The main improvement, however, is present in the roll angle, which keeps values near zero over all the simulation time. By observing the graph on the right, the $K = 1 \times 10^{-2}$ case, the same can be said. However, the oscillatory behaviour appears a bit stronger in all the angles considered.

When increasing the weight of the tip mass, as it can be seen in Figure 65, the remnants of the oscillations disappear even for the pitch angle of the hub, the sail, then, behaving almost as a rigid body for this maneuver.
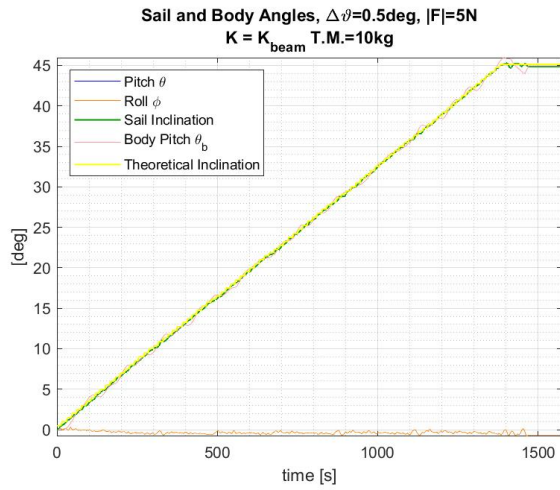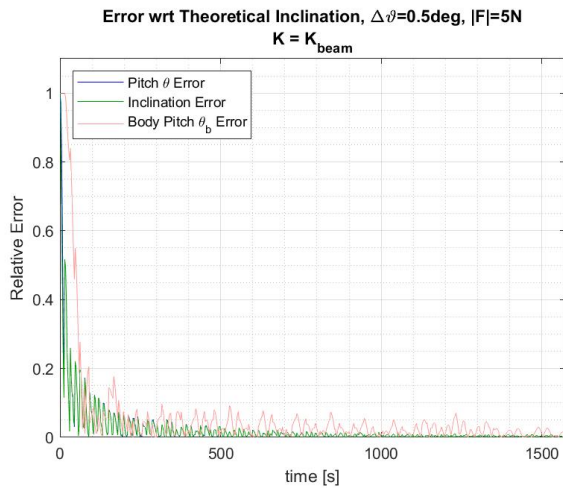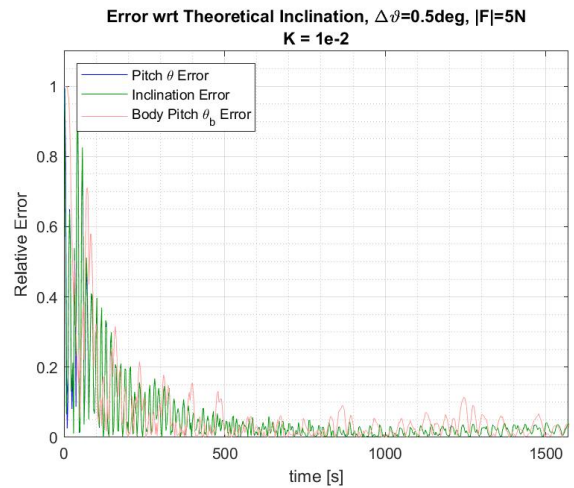
(a) $K = K_{beam}$.
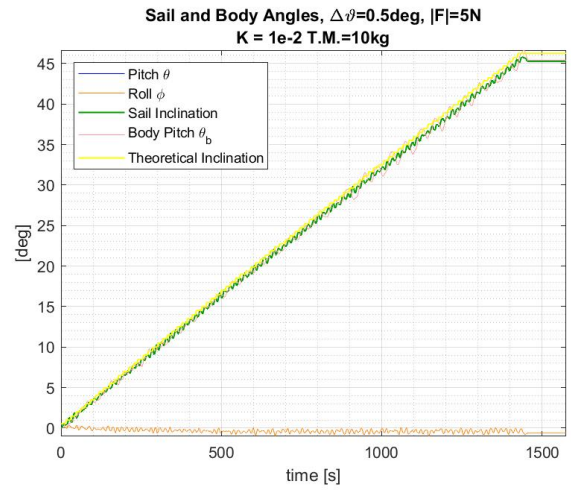
(b) $K = 1 \times 10^{-2}$.

Figure 65: Body Pitch, Sail Inclination, Pitch and Roll for a tip-mass weight of 10 kg.

Now, the error with respect to the theoretical values will be displayed:
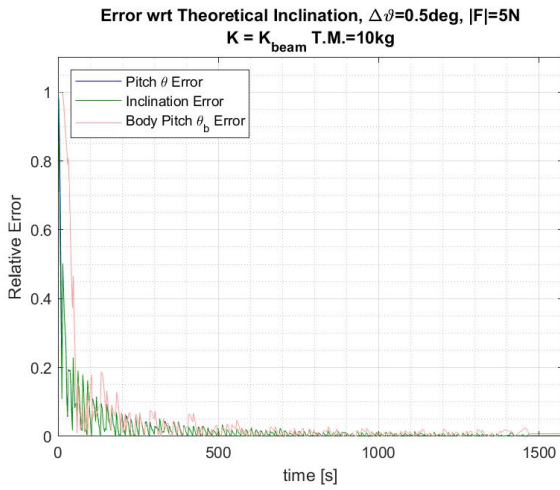

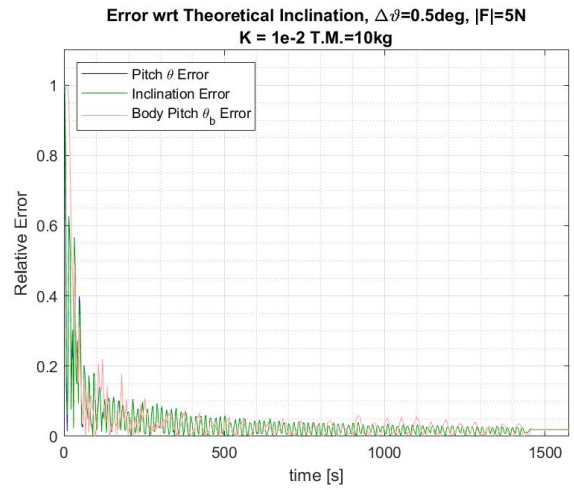(a) $K = K_{beam}$.

(b) $K = 1 \times 10^{-2}$.

Figure 66: Relative error between theoretical and expected pitch angle, and inclination of the sail for a tip-mass weight of 5 kg.

While using the conventional Rhumb-Line Maneuver, the error values were kept, from the middle of the maneuver onwards, below 5%, 10% and 20% for the inclination, sail pitch and body pitch angles, respectively, considering a bending parameter $K = K_{beam}$; and below 10%, 15% and 30% for $K = 1 \times 10^{-2}$. With the application of the roll control method, in contrast, the error decreases quickly reaching values as low as $0 - 1\%$ for both sail angles and 5% for the body pitch at just 1/3 of the simulation time for $K = K_{beam}$; and a similar decrease is seen in the $K = 1 \times 10^{-2}$ case, with errors below 5% for all angles considered, although there are some peaks for the body hub that reach up to 10% sporadically.

In Figure 65, it was already observed an improvement in the performance when increasing the tip-mass weight. In Figure 67, that improvement is consolidated when seeing that errors for all angles, even for the pitch angle of the hub, remain between 0 and 2% through the most part of the simulation.
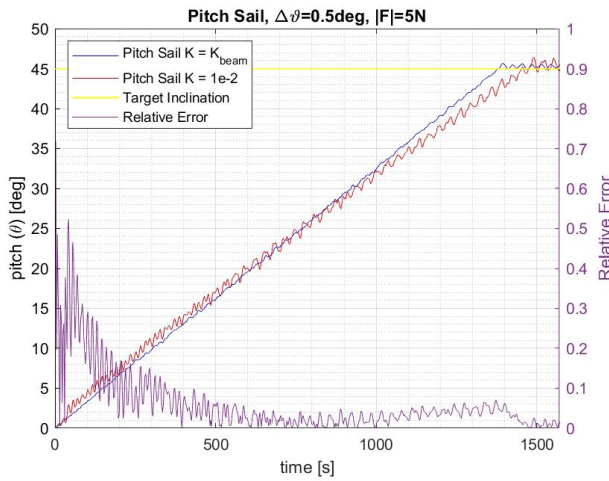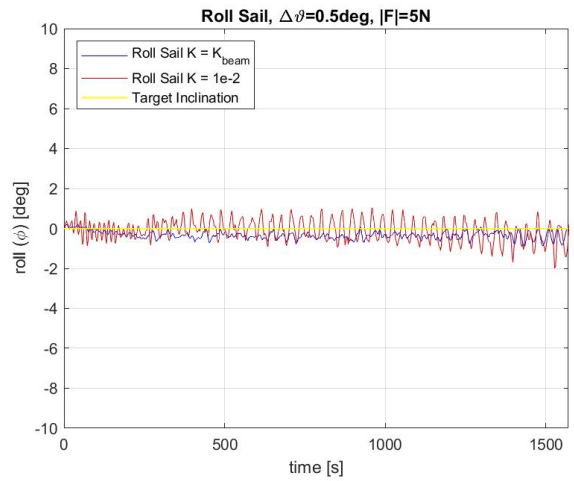
(a) $K = K_{beam}$.

(b) $K = 1 \times 10^{-2}$.

Figure 67: Relative error between theoretical and expected pitch angle, and inclination of the sail for a tip-mass weight of 10 kg.

In the following figures, results for the different bending stiffness will be compared one with another.
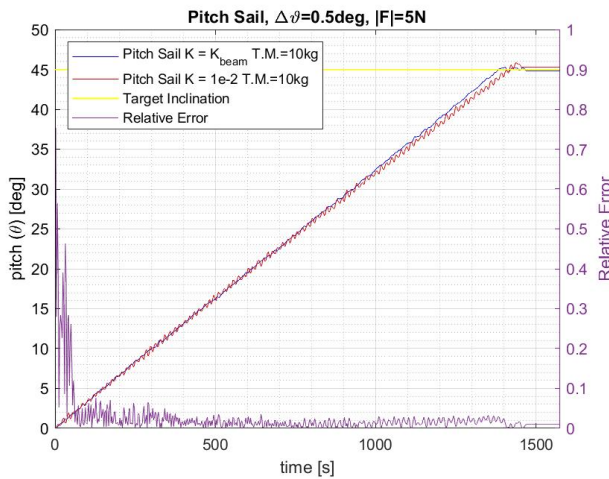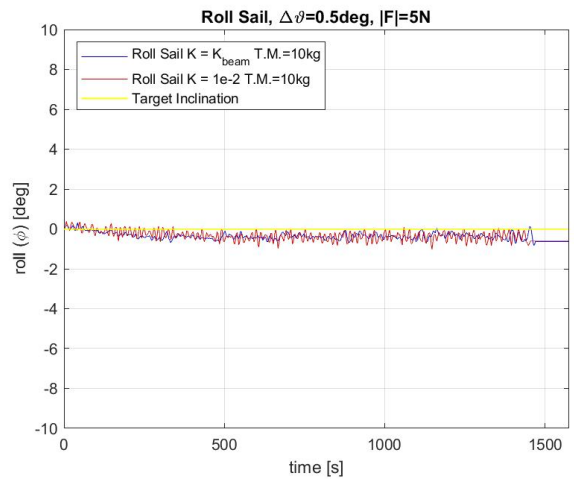

(a) Pitch angle.

(b) Roll angle.

Figure 68: Comparison between the pitch and roll for tip-mass of 5 kg.

(a) Pitch angle.

(b) Roll angle.

Figure 69: Comparison between the pitch and roll for tip-mass of 10 kg.

Figures 68 and 69 show up to which extend the bending stiffness affects the attitude of the sail during the axis reorientation. Before the roll control implementation, in Figure 43 a relative error of about 10% was observed during the last stages of the simulation, while in the middle it was placed around 20%. That error was caused mainly by the differences in the roll angle depending on the bending parameter.

As it can be seen in the b) plots, with roll control being active the roll angle is kept between 1 and $-1°$ in the most unfavorable case (Figure 68, $K = 1 \times 10^{-2}$). Without significant differences in this angle, the divergence between pitch angles is found to be below 5% during most part of the simulation for a conventional tip-mass weight. When increasing that weight up to 10 kg, differences get as low as 2%.

Therefore, with the implemented control, the attitude does not depend anymore on the bending of the sail when a thrusting input of 5 N is applied over the membrane.

6.2.1.1 Nutation

The following figures present the recording of the nutation of the hub for the improved control method applied to the present cases:
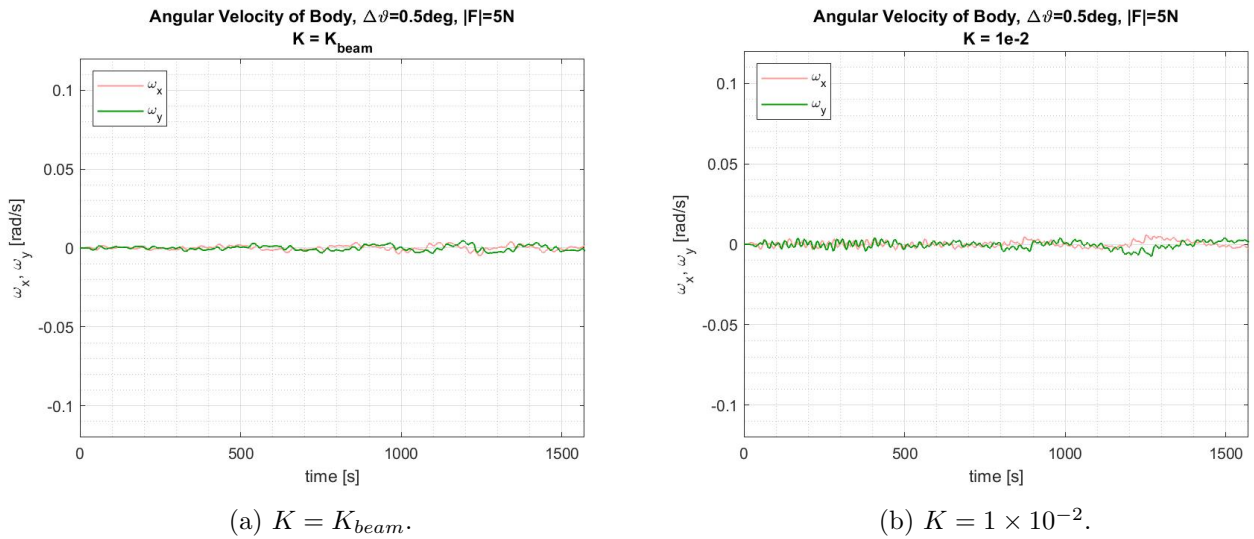

(a) $K = K_{beam}$.

(b) $K = 1 \times 10^{-2}$.

Figure 70: ω_x and ω_y of the hub, tip-mass weight of 5 kg.

(a) $K = K_{beam}$.

(b) $K = 1 \times 10^{-2}$.
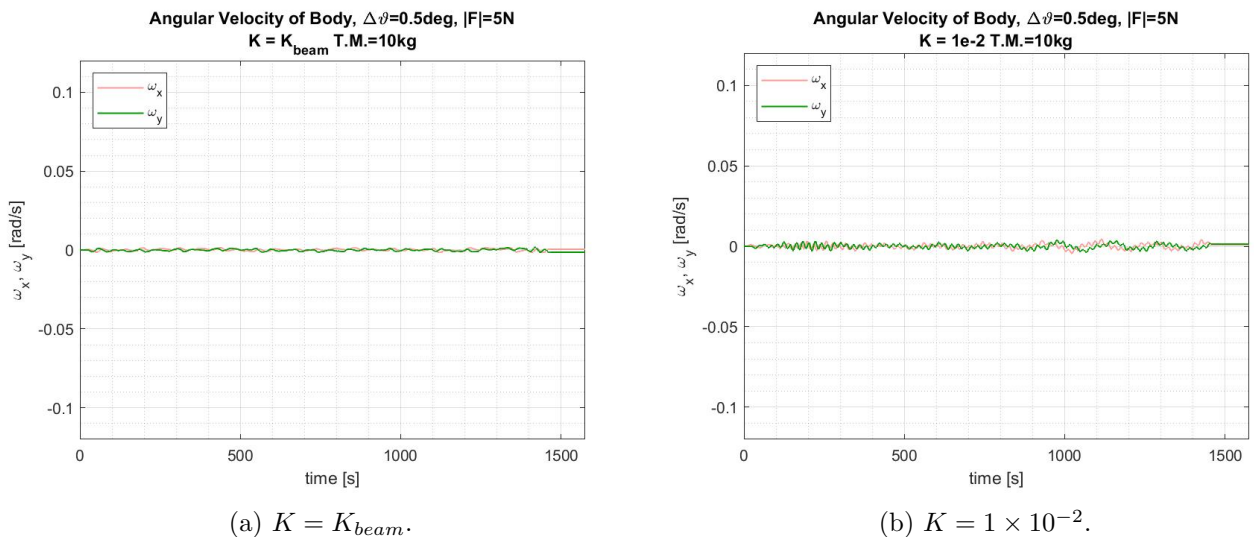
In Section 5.2, for a $\Delta\theta = 0.5$ deg and $|F| = 5$ N, the angular velocity of the hub went up to a magnitude of 0.03 rad/s and 0.05 rad/s for both bending stiffnesses considered. Now, the magnitude of the angular velocity components remains close to zero in the four cases, so the nutational motion is no longer present.

The same results will be presented below for higher thruster inputs, so as to see if the improved control method performs correctly also under those circumstances.

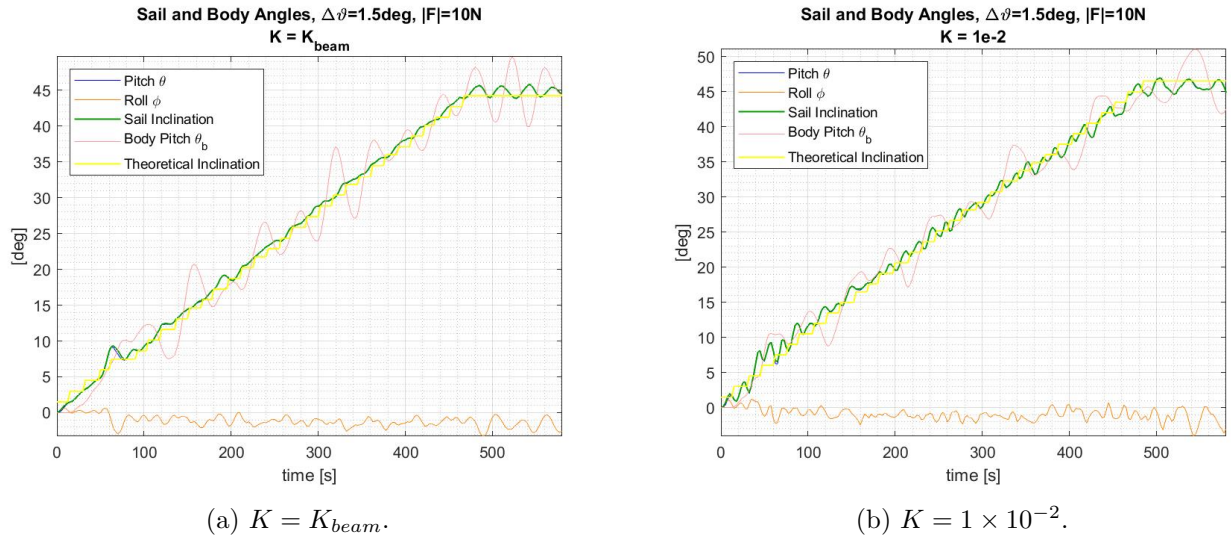### 6.2.2 $\Delta\theta = 1.5$ deg and $|F| = 10$ N Simulation Results

(a) $K = K_{beam}$.

(b) $K = 1 \times 10^{-2}$.

Figure 72: Body Pitch, Sail Inclination, Pitch and Roll for a tip-mass weight of 5 kg.

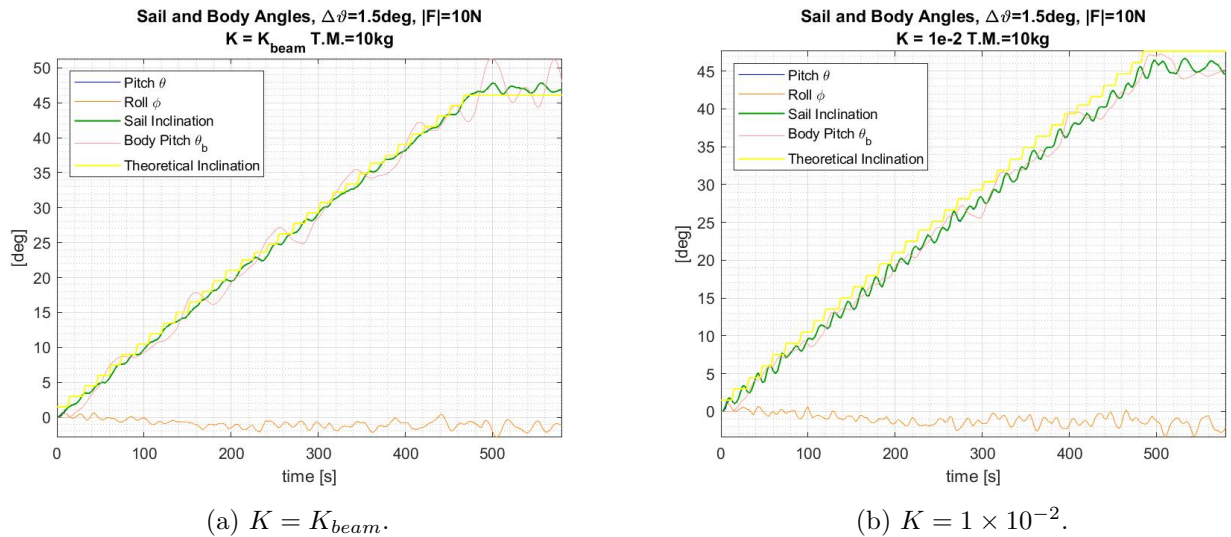
(a) $K = K_{beam}$.

(b) $K = 1 \times 10^{-2}$.

Figure 73: Body Pitch, Sail Inclination, Pitch and Roll for a tip-mass weight of 10 kg.

Contrary to what was observed in Figures 46 and 47, the roll angle is kept under control, so the inclination of the sail and the pitch angle have the same value. The oscillations of the body pitch angle get slightly higher for the conventional $K = K_{beam}$ case, although not even close to the ones in Figure 46, where the variation between minimum and maximum was of about $30°$. The magnitude of the

oscillations, as it happened in the previous section, almost disappear when doubling the weight of the tip-mass.

As for the performance of the maneuver, it can be seen that the angles are found over the yellow line or the expected value according to Equation 57. Next, the performance is analyzed further in Figures 74 and 75:

(a) $K = K_{beam}$.
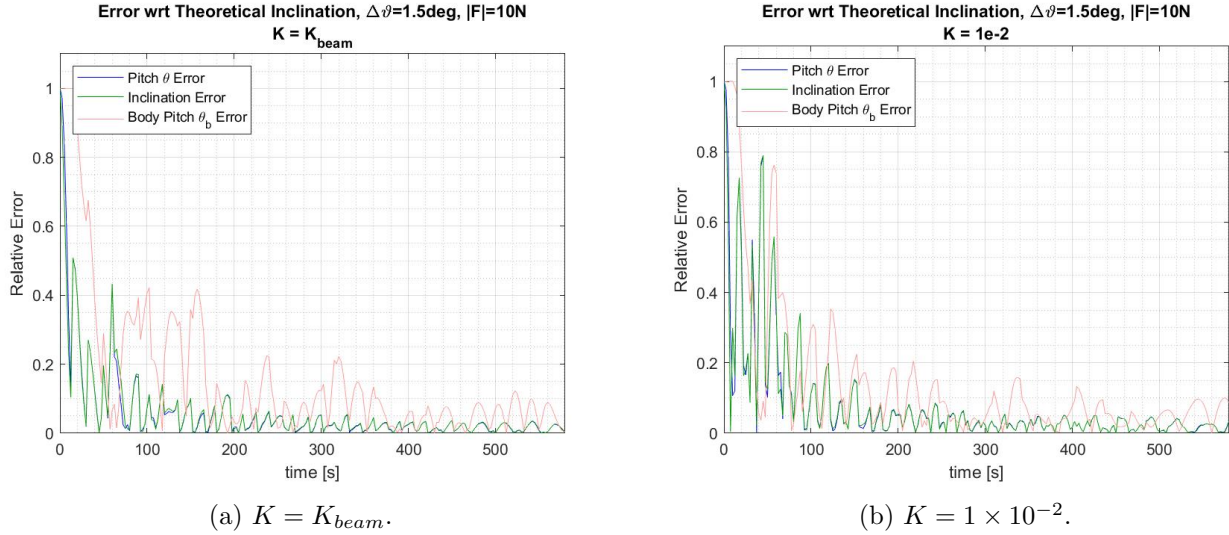
(b) $K = 1 \times 10^{-2}$.

Figure 74: Relative error between theoretical and expected pitch angle, and inclination of the sail for a tip-mass weight of 5 kg.

(a) $K = K_{beam}$.
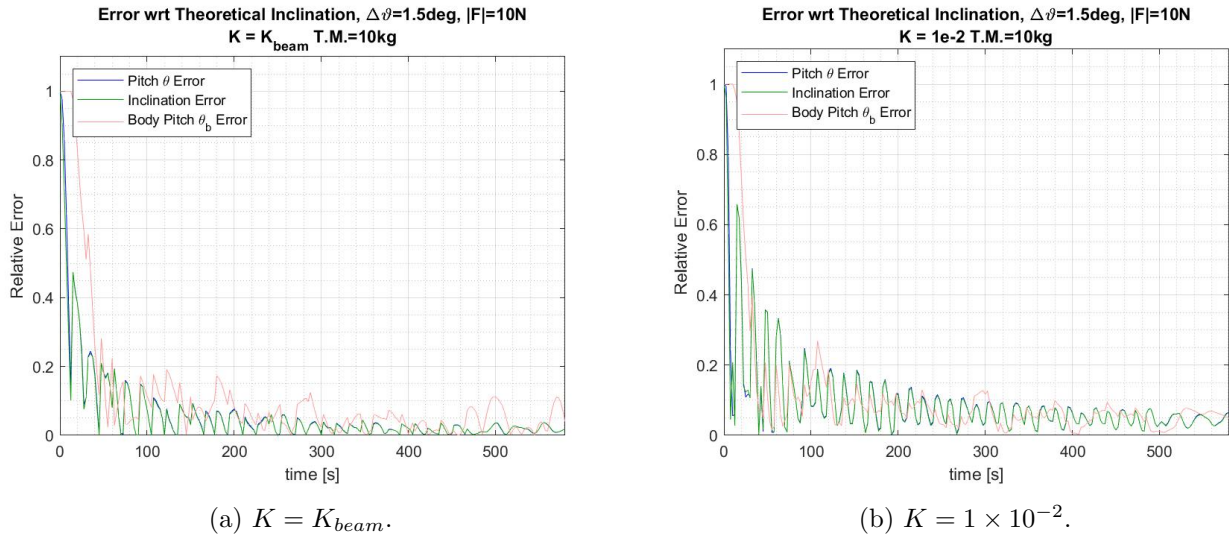
(b) $K = 1 \times 10^{-2}$.

Figure 75: Relative error between theoretical and expected pitch angle, and inclination of the sail for a tip-mass weight of 10 kg.

A performance that in Section 5.2 carried an error 20% as its best ($30 - 40\%$ when considering only the pitch angle of the sail instead of both pitch and inclination angles), after the application of the roll control came below 5% regardless of the bending parameter for about the last 2/3 of the total time of the simulation. The error for the pitch angle of the body also went down, from $60 - 80\%$ to 10% for a conventional tip-mass weight of 5 kg, which supposes a significant improvement. When increasing its weight, the hub's pitch error gets as low as the one of the angles of the membrane.

As before, pitch and roll angles of the sail are to be compared separately for the different bending constants that have been taken into account:
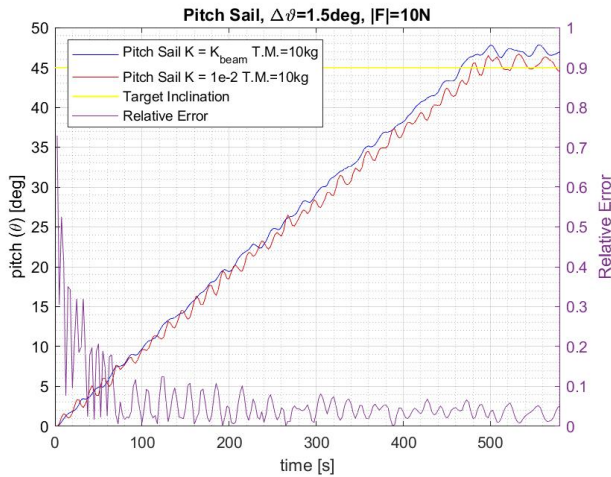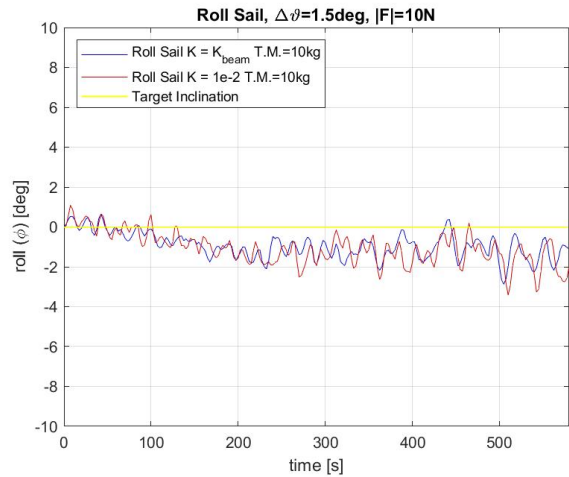
61
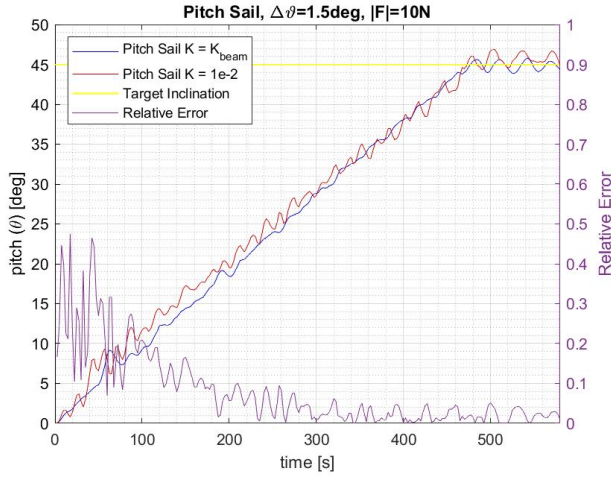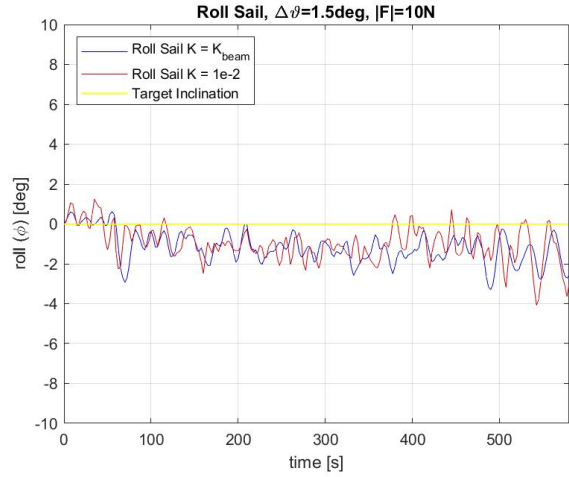
(a) Pitch angle.   (b) Roll angle.

Figure 76: Comparison between the pitch and roll for tip-mass of 5 kg.

(a) Pitch angle.   (b) Roll angle.

Figure 77: Comparison between the pitch and roll for tip-mass of 10 kg.

Prior to the improvement of the control method, the roll angle reached values of $-40°$ for the $K = 1 \times 10^{-2}$ case. The correction in the roll angle, that now gets to $-4°$ in the worst recorded value and that is found between 0 and $-2°$ during almost all the simulation, is the most remarkable feature of the present plots when compared to the previously obtained ones in Section 5.2.

The differences due to considering different rigidities on the sail are also lowered from a 30% of relative error in Figure 49 to 4% in Figures 76 and 77. The main difference obtained from the tip-mass weight value variation was observed to be in the oscillations of the pitch angle of the hub, and therefore here both Figures 76 and 77 present similar results. A reduction on the magnitude of the roll angle is obtained, nonetheless.

6.2.2.1   Nutation

As mentioned in the paragraph above, the increase on the weight of the tip-mass was translated into a reduction of the oscillations of the pitch angle of the hub. This reduction can be corroborated when comparing Figures 78 and 79, where the angular velocity decreases from a magnitude slightly above 0.01 to values between 0 and 0.005 rad/s.

Even the higher oscillations recorded are far smaller than the ones from the previous Rhumb-Line Maneuver algorithm, whose peaks reached as high as 0.07 rad/s.
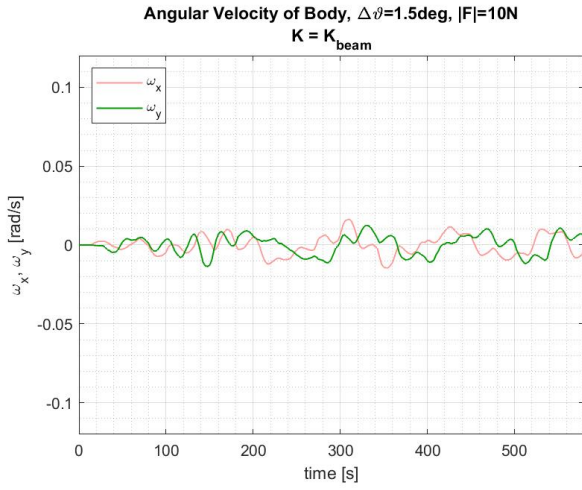
(a) $K = K_{beam}$.
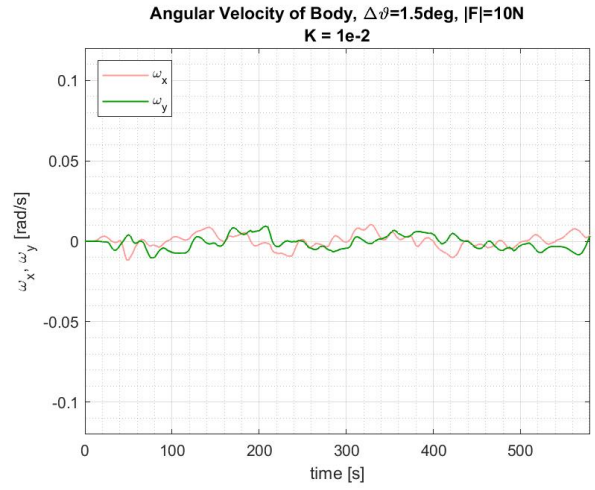
(b) $K = 1 \times 10^{-2}$.

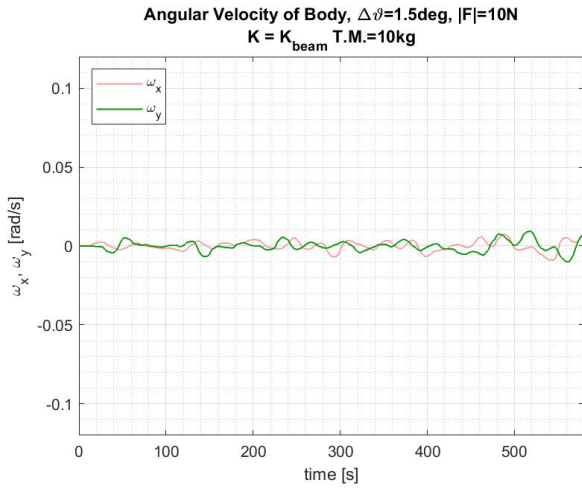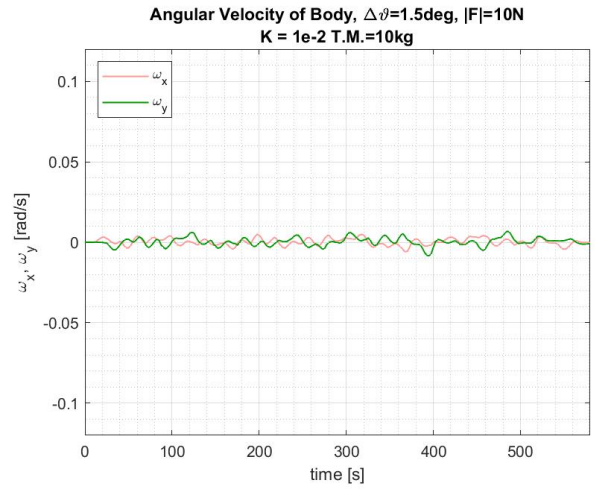Figure 78: ω_x and ω_y of the hub, tip-mass weight of 5 kg.

(a) $K = K_{beam}$.
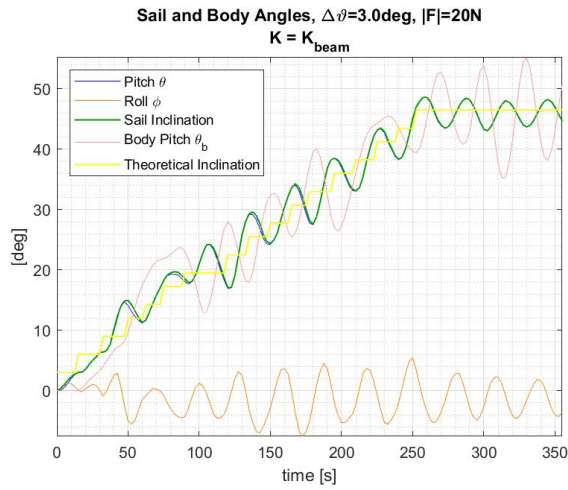
(b) $K = 1 \times 10^{-2}$.

Figure 79: ω_x and ω_y of the hub, tip-mass weight of 10 kg.

6.2.3 $\varDelta\theta = 3.0$ deg and $|F| = 30$ N Simulation Results

Finally, the last case is studied. In Section 5.2, for a $\varDelta\theta = 3.0$ deg and $|F| = 20$ N, the oscillations over the three angles considered augmented, with a peak to peak distance of around 20° for the sail angles and up to 40° for the spacecraft's body ones. Besides the oscillations, the performance of the maneuver fell although the roll angle obtained was not as great as for the $\varDelta\theta = 1.5$ deg and $|F| = 10$ N simulation.

With the active roll control, although greater oscillations of the angles measured when comparing them to the previous two thrusting cases are obtained, the performance of the maneuver keeps up with the ideal one for the $K = K_{beam}$ and slightly below it for $K = 1 \times 10^{-2}$. However, its detriment is, by all means, insignificant in comparison with what was obtained in Section 5.2.

When considering a greater tip-mass, the oscillations diminish for all the bending cases and angles presented but for the hub's pitch angle of the lesser bending case, that remains approximately the same. The performance of the maneuver for the more rigid membrane also improves.
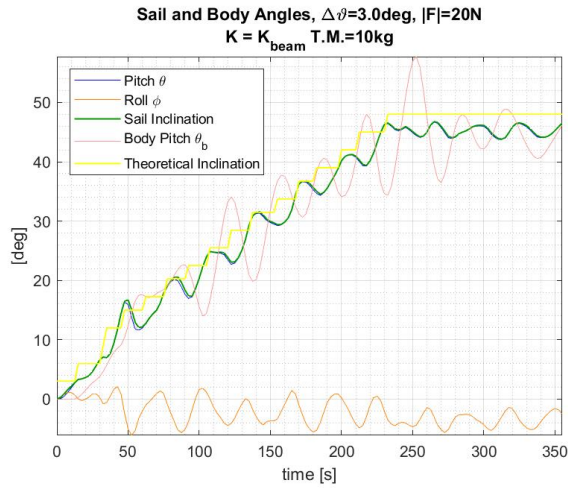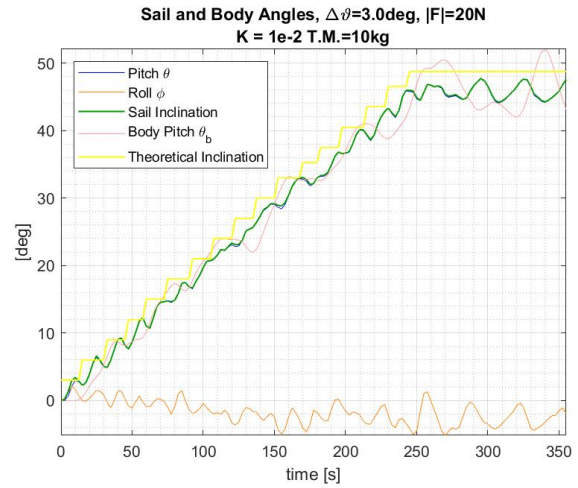
(a) $K = K_{beam}$.
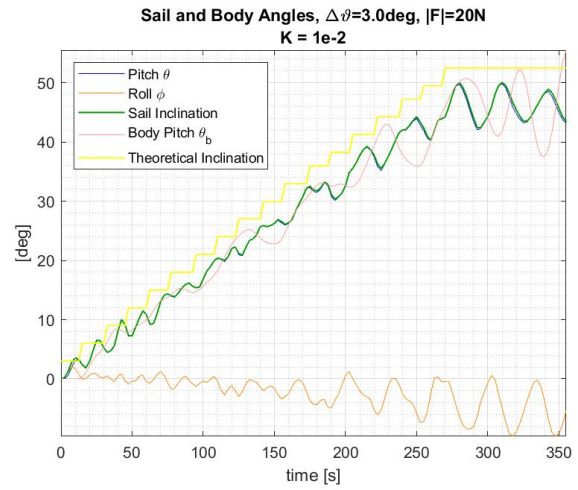
(b) $K = 1 \times 10^{-2}$.

Figure 80: Body Pitch, Sail Inclination, Pitch and Roll for a tip-mass weight of 5 kg.

(a) $K = K_{beam}$.

(b) $K = 1 \times 10^{-2}$.

Figure 81: Body Pitch, Sail Inclination, Pitch and Roll for a tip-mass weight of 10 kg.

The actual error with respect to the theoretical inclination of the sail is displayed in Figures 82 and 83.

Despite the drop in performance observed, the error for the sail and hub angles is $5 - 10\%$, $15 - 20\%$ and $10 - 20\%$, $10 - 25\%$ for each of the graphs in Figure 80, respectively. As it could be inferred from the figures above, the more rigid case performs the worst, as a higher bending stiffness leads to higher vibrations as it will be shown in the frequency analysis.

However, without the improved roll control method these values were an overwhelming 50% and 80% error for the sail and hub angles, respectively.

Once the tip-mass weight is doubled, despite the error of the $K = 1 \times 10^{-2}$ is reduced until it reaches the same magnitude as the error observed for the sail angles when a $K = K_{beam}$ is considered, it does not lead to significant improvements for the former rigidity case.
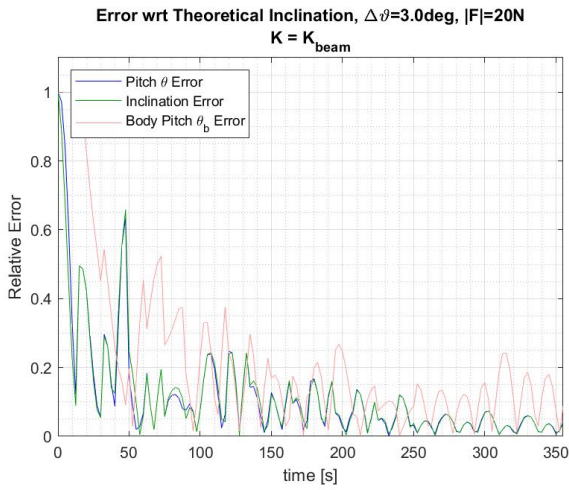
(a) $K = K_{beam}$.
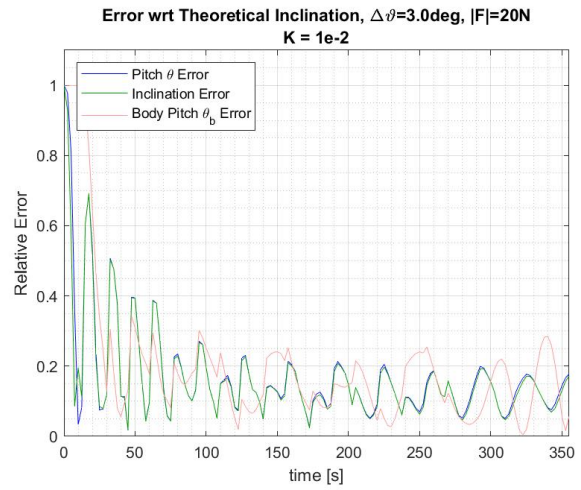
(b) $K = 1 \times 10^{-2}$.

Figure 82: Relative error between theoretical and expected pitch angle, and inclination of the sail for a tip-mass weight of 5 kg.

(a) $K = K_{beam}$.

(b) $K = 1 \times 10^{-2}$.

Figure 83: Relative error between theoretical and expected pitch angle, and inclination of the sail for a tip-mass weight of 10 kg.

Now, the sail angles are to be plotted separately:

(a) Pitch angle.
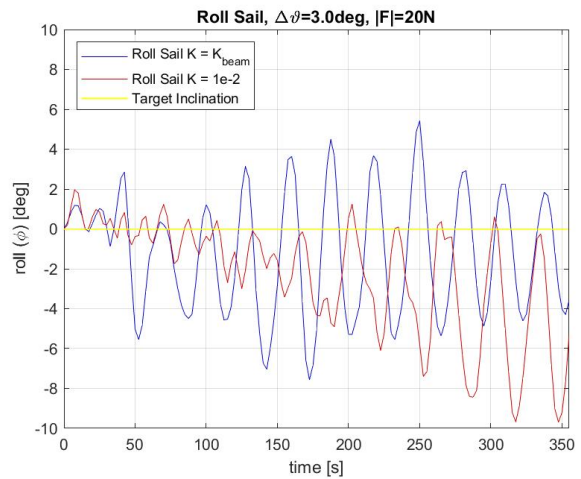
(b) Roll angle.

Figure 84: Comparison between the pitch and roll for tip-mass of 5 kg.
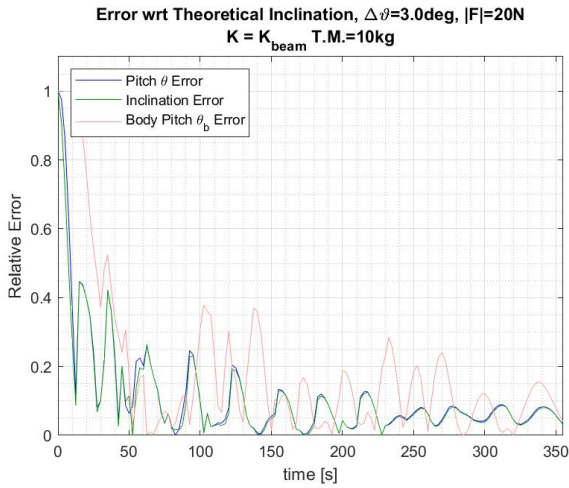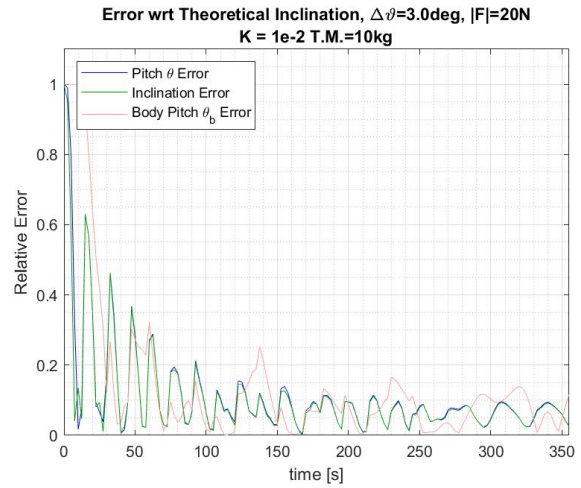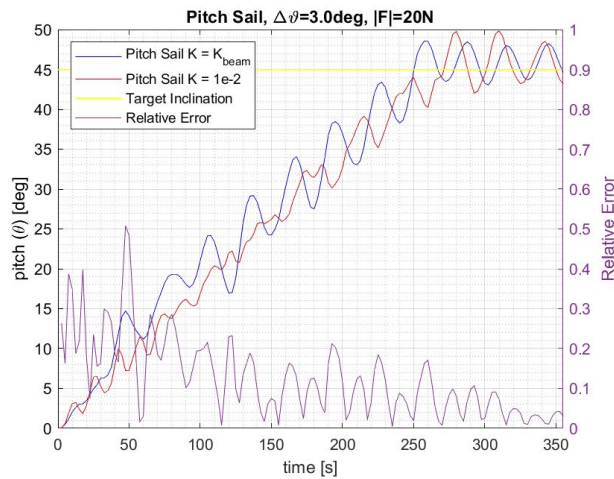

(a) Pitch angle.

(b) Roll angle.
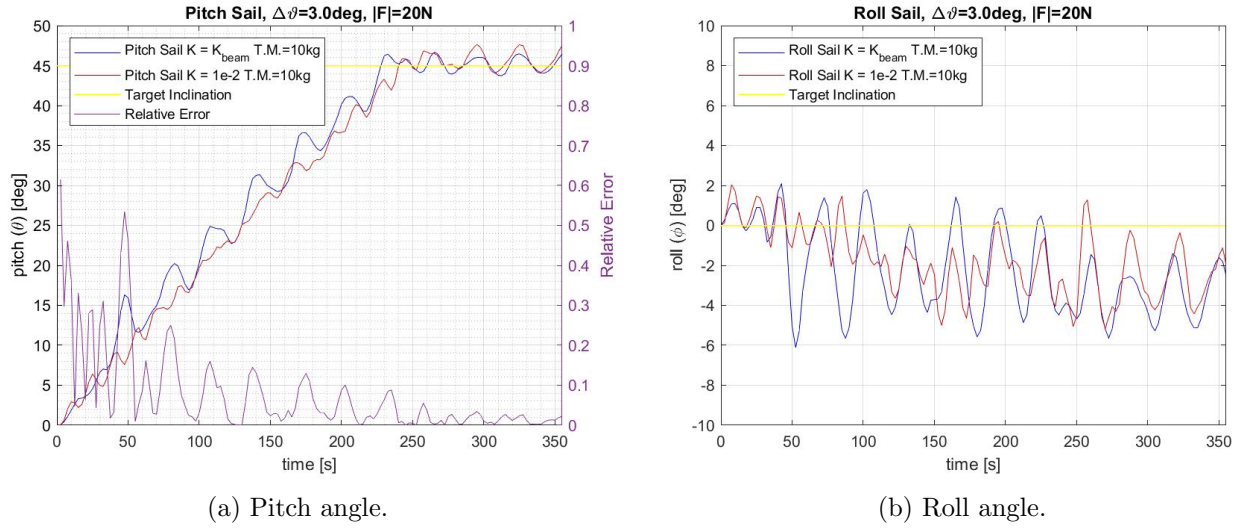
Figure 85: Comparison between the pitch and roll for tip-mass of 10 kg.

The difference in the pitch angle of the sail depending on the bending character of the membrane oscillates between zero and 20%. However, as it can be appreciated in the left plot of Figure 84, both values overlap through the maneuver. The high oscillations, however, when not in phase lead to higher differences between values. When increasing the tip-mass, though, the overlapping is still effective, and the reduction of the oscillations makes the difference in the pitch angle to diminish.

The roll angle, as the input force became stronger, presents a rougher graph. Specially for the higher bending parameter case, its value is seen to diverge when approaching the end of the simulation, getting to magnitudes as high as 10°. That behaviour is corrected with a tip-mass of 10 kg, for which the oscillations of the value are decreased for both cases and their plots match up to a greater extent.

6.2.3.1 Nutation

Before proceeding to the frequency analysis, the corresponding graphs for the nutational motion of the hub of the sail are presented below:

(a) $K = K_{beam}$.

(b) $K = 1 \times 10^{-2}$.

Figure 86: ω_x and ω_y of the hub, tip-mass weight of 5 kg.

(a) $K = K_{beam}$.

(b) $K = 1 \times 10^{-2}$.
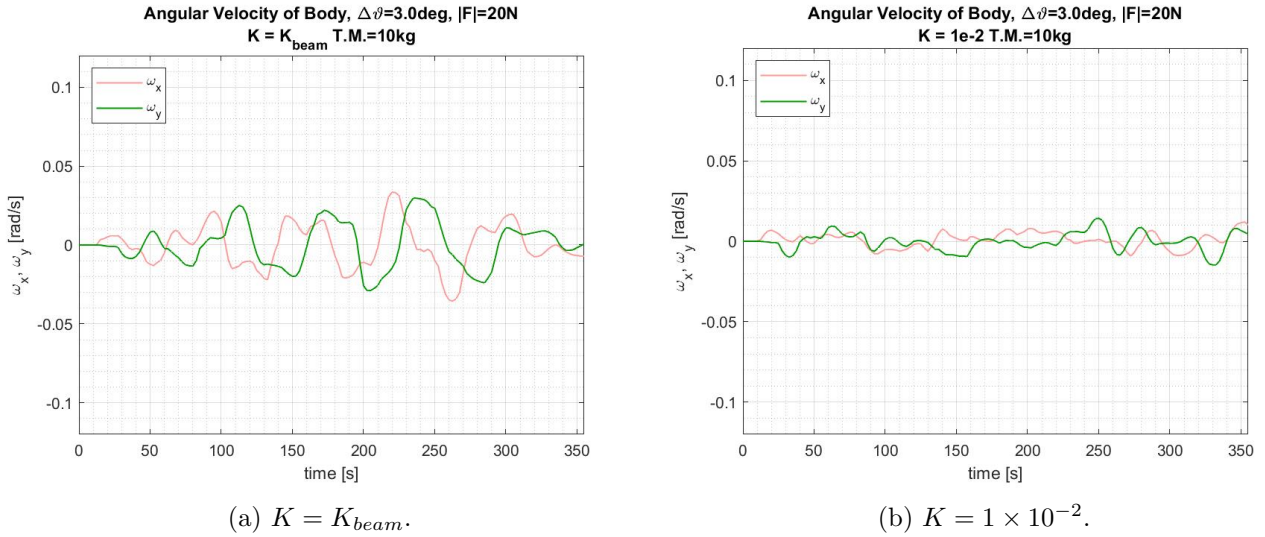
Figure 87: ω_x and ω_y of the hub, tip-mass weight of 10 kg.

From Figure 80, the angular velocity of the hub for the $K = K_{beam}$ simulation could have been inferred to present an oscillatory behaviour from the evolution of the pitch angle along the maneuver. Nonetheless, the maximum value presented in magnitude is of 0.04 rad/s, more than half below the corresponding ones when applying the first Rhumb-Line Maneuver algorithm. The much lower oscillations 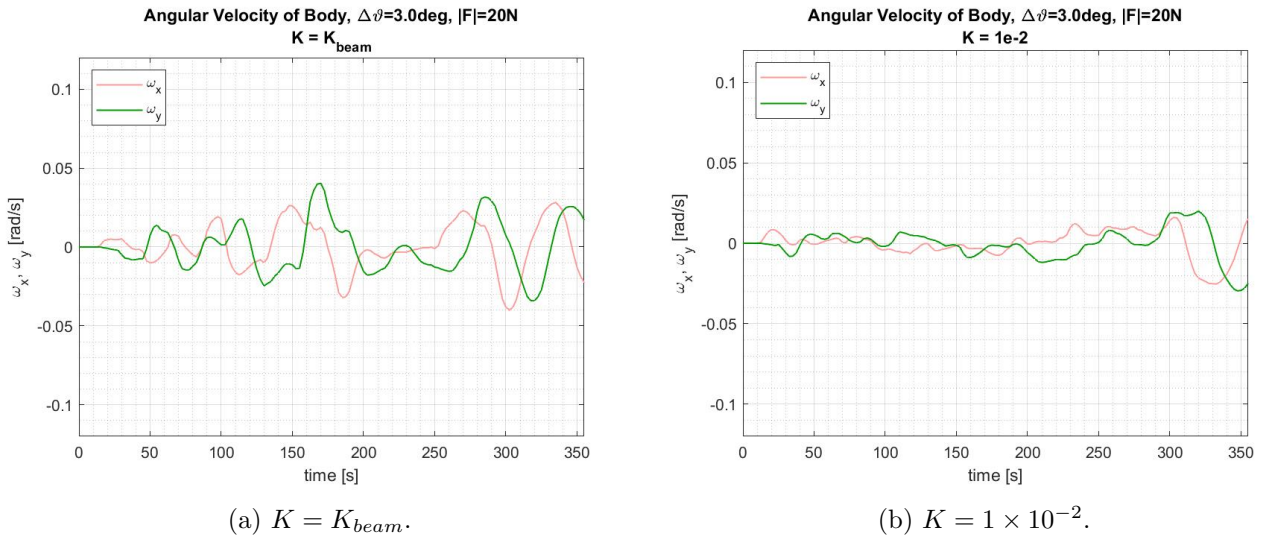of the pitch angle for $K = 1 \times 10^{-2}$ see themselves translated into low angular velocity values in these graphs.

As well as it happened in all the previous cases studied, doubling the tip-mass weight lowers the nutation of the hub. Despite that, oscillations on its value are still high for the non-rigid membrane case.

6.3 Frequency analysis on the response of the membrane due to tip-mass thrusting

In Section , a particular analysis for the results of every thrusting input was added after the respective figures showing the frequency spectrum of the out-of-plane motion of the particles constituting the membrane. However, the behaviour of the membrane in the frequency domain for the simulations present in this section do not present significant changes when incrementing the thruster's force except for the amplitude. Therefore, so as to avoid repetition, the FFT spectrum graphs will be presented together below so as the reader to be able to appreciate them, and will be analysed also altogether after their display.

(a) $K = K_{beam}$.

(b) $K = 1 \times 10^{-2}$.

Figure 88: Frequency analysis for $\Delta\theta = 0.5$ deg and $|F| = 5$ N; tip-mass 5 kg.

(a) $K = K_{beam}$.
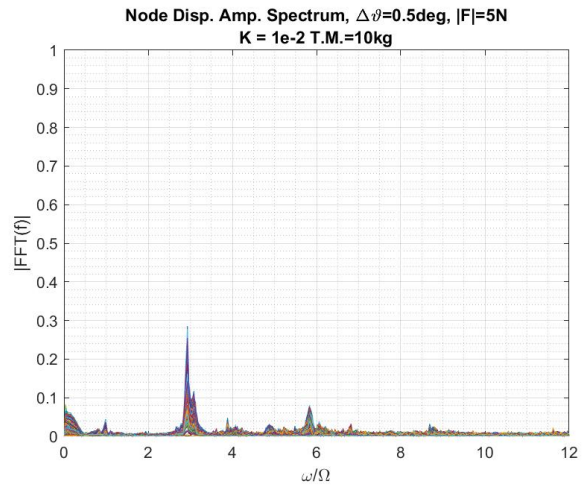
(b) $K = 1 \times 10^{-2}$.

Figure 89: Frequency analysis for $\Delta\theta = 0.5$ deg and $|F| = 5$ N; tip-mass 10 kg.
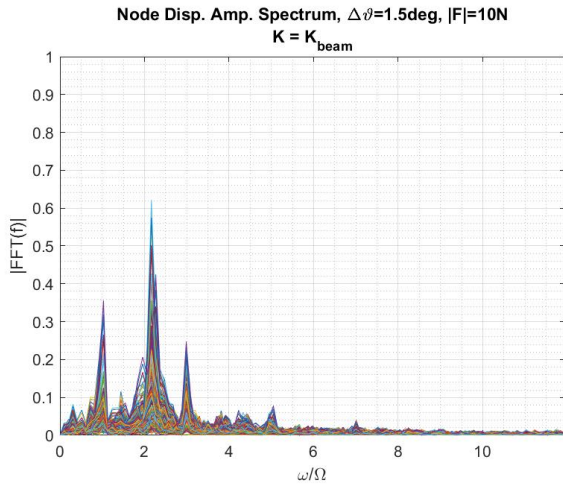
(a) $K = K_{beam}$.
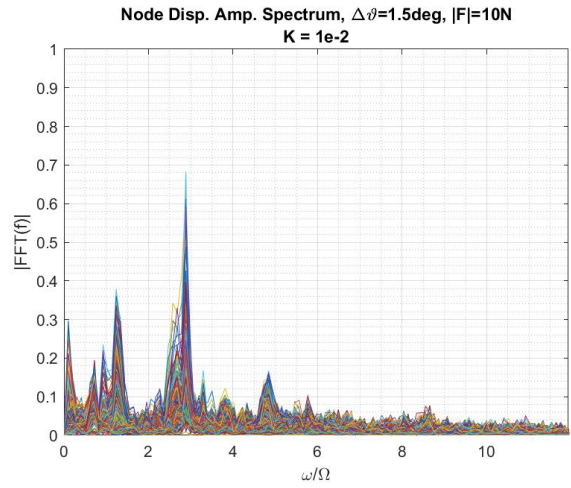
(b) $K = 1 \times 10^{-2}$.

Figure 90: Frequency analysis for $\Delta\theta = 1.5$ deg and $|F| = 10$ N; tip-mass 5 kg.
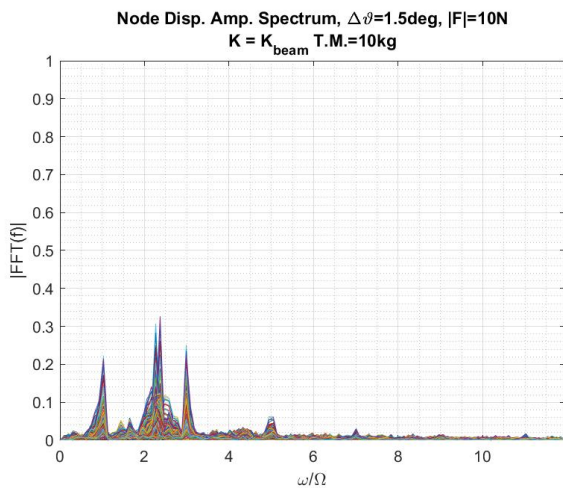
(a) $K = K_{beam}$.
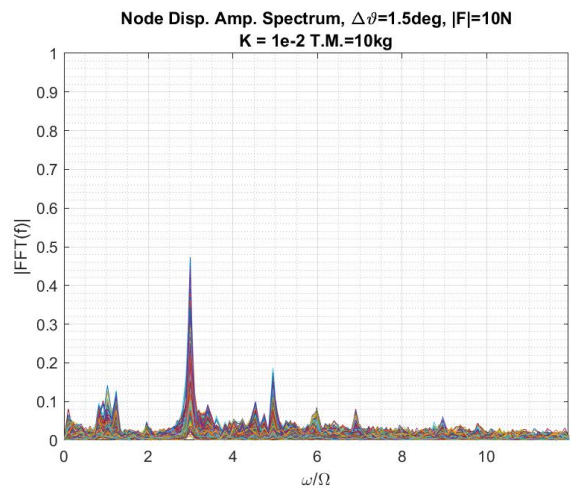
(b) $K = 1 \times 10^{-2}$.

Figure 91: Frequency analysis for $\Delta\theta = 1.5$ deg and $|F| = 10$ N; tip-mass 10 kg.

(a) $K = K_{beam}$.

(b) $K = 1 \times 10^{-2}$.
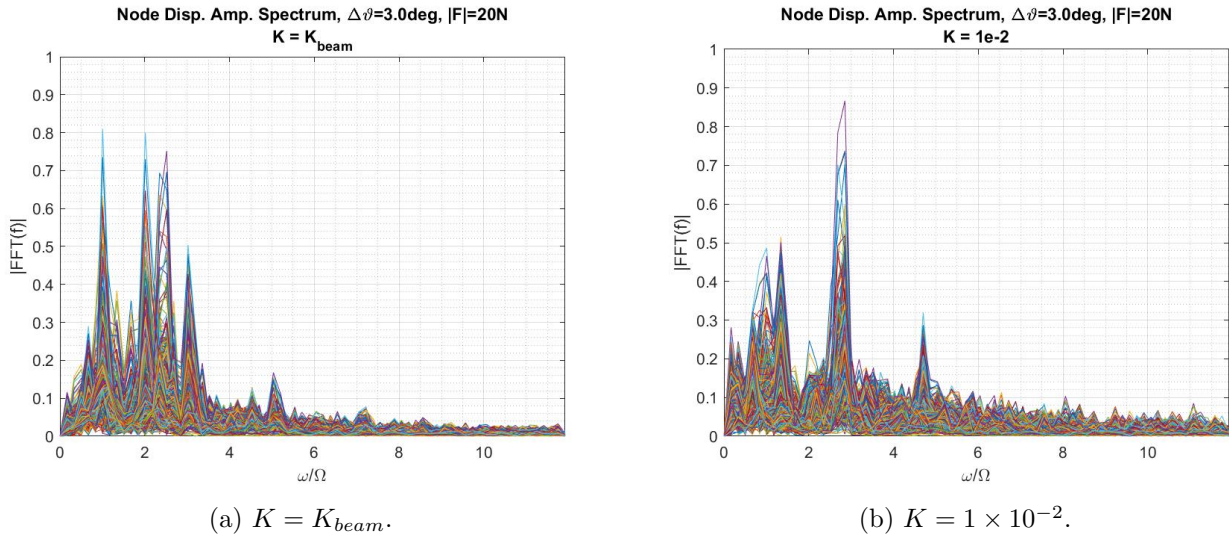
Figure 92: Frequency analysis for $\Delta\theta = 3.0$ deg and $|F| = 20$ N; tip-mass 5 kg.

(a) $K = K_{beam}$.

(b) $K = 1 \times 10^{-2}$.

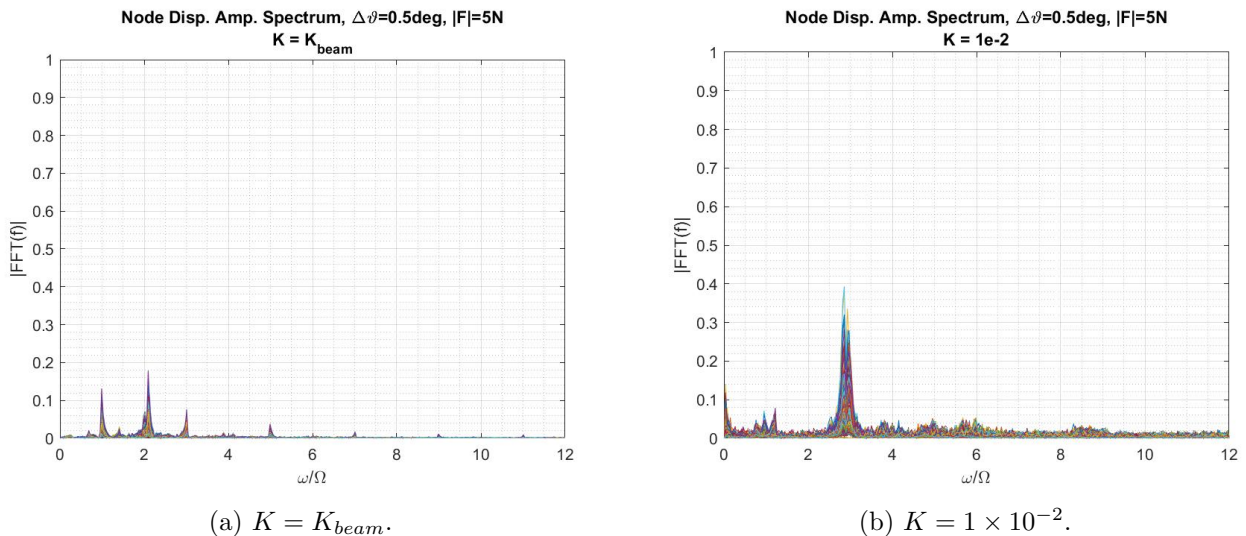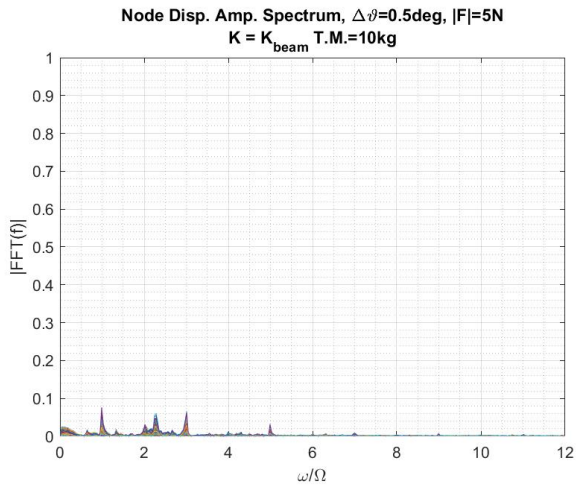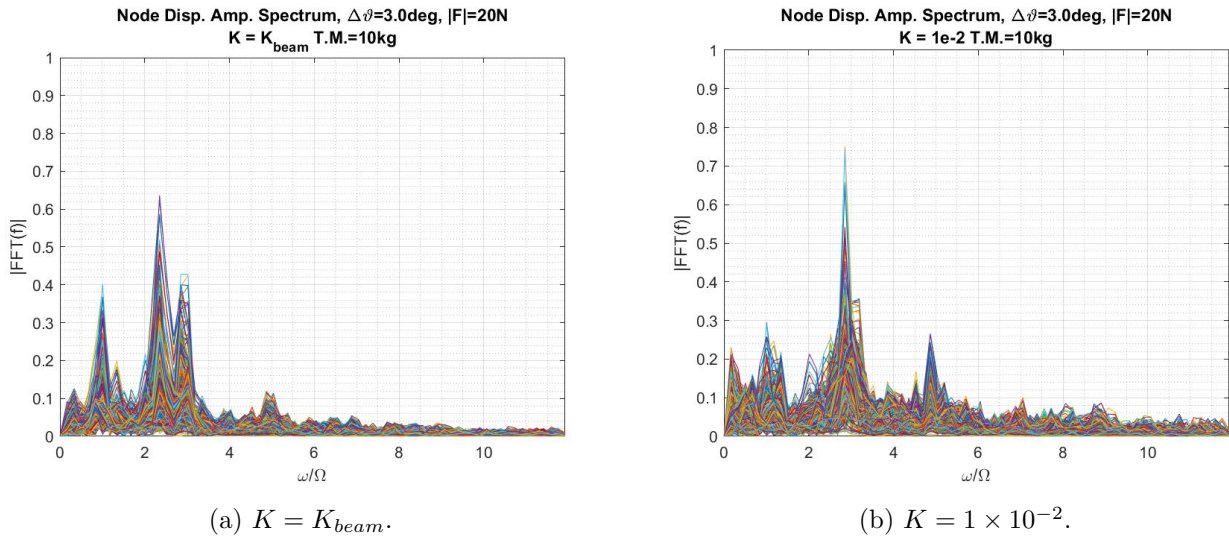Figure 93: Frequency analysis for $\Delta\theta = 3.0$ deg and $|F| = 20$ N; tip-mass 10 kg.

As stated before, regardless of the input force, in terms of frequency all figures present the same behaviour depending on the bending stiffness considered.

For a bending constant given from the cantilever approximation, $K = K_{beam}$, the excited frequencies are those corresponding to $\hat{\omega} = 1$, 2 and 3 which, considering $n = 1$ in Equation 78, are those modes excited for a circumferential order $\nu' = 1$, 3, 5, respectively. The dominant peak out of these three is the one at $\hat{\omega} = 2$, with $\hat{\omega} = 1$ gaining relevance as the input force increases.

As for $K = 1 \times 10^{-2}$, the excited frequencies are $\hat{\omega} = 1$, 3, and the peak at 2 does not appear. As the input force becomes larger, higher order frequencies are excited, and a peak at $\hat{\omega} = 5$ makes its apparition.

The differences in frequency distribution when increasing the bending stiffness of the sail up to the extent that the aspect of the membrane changes (Figure 24) can be explained when considering the

studies presented in [29]. Although the approximation for linear strains is considered in its derivation of the equation of motion, the effect of bending stiffness is taken into account. The study on the normal frequencies of a spinning disk using the derived equations show that in that case certain modes of vibration get cut off.

Regardless of the bending stiffness and the input force, the effect of increasing the weight of the tip-mass always results in both a reduction of the amplitude of the vibrations and a higher definition on the excited peaks.

6.4 Insights

In the following table, Table 5, some parameters of interest for the analysis of the reorientation maneuver are displayed for the simulations carried out. Here, *W/o* stands for *Without Active Roll Control*, that is, the maneuver as presented in the previous section, Section 5. ARC_5 and ARC_{10} stand for *Active Nutation Control* and the parameters correspond to those obtained in this section, that meaning after the implementation of the roll control in the previous algorithm, Algorithm 1. The subindex stands for the weight of the tip-mass.

Table 5: Maneuver Comparison

$$K = K_{bend}$$

	Sail's Pitch Error			$|\phi|$ **[deg]**			$|\omega_{x,y}|$ [rad/s]		
Simulation	**W/o**	ARC_5	ARC_{10}	**W/o**	ARC_5	ARC_{10}	**W/o**	ARC_5	ARC_{10}
0.5 deg, 5 N	≈ 0.05	≈ 0.0	≈ 0.0	<15	<0.5	<0.5	< 0.3	< 0.005	0
1.5 deg, 10 N	≈ 0.3	≈ 0.05	≈ 0.025	< 25	<3	<2	< 0.6	< 0.02	<0.01
3.0 deg, 20 N	≈ 0.5	≈ 0.1	≈ 0.1	< 35	<8	<6	< 0.12	< 0.04	<0.03

$$K = 1 \times e - 2$$

	Sail's Pitch Error			$|\phi|$ **[deg]**			$|\omega_{x,y}|$ [rad/s]		
Simulation	**W/o**	ARC_5	ARC_{10}	**W/o**	ARC_5	ARC_{10}	**W/o**	ARC_5	ARC_{10}
0.5 deg, 5 N	≈ 0.1	≈ 0.02	≈ 0.01	<17	<2	<0.5	< 0.5	< 0.01	<0.005
1.5 deg, 10 N	≈ 0.4	≈ 0.05	≈ 0.05	< 45	<4	<3	< 0.7	< 0.01	<0.005
3.0 deg, 20 N	≈ 0.5	≈ 0.15	≈ 0.07	< 35	<10	<5	< 0.12	< 0.03	<0.015

By using the tip thrusting system in Section 5, several improvements with respect to the in-body thrusting system were found, like an almost rigid body-like performance of the maneuver for low thrusting forces, a reduction in the nutation of the hub and a response of the membrane that was affected by the difference in bending stiffness up to a much lower extent. However, several problems like the apparition of a high undesired roll angle or the plummeting of all the advantages described above when increasing the thrusting input were important flaws of the new control system proposed.

Nonetheless, with the implementation of an active roll control in the maneuver's algorithm, the drawbacks listed above have been overcome. The performance of the maneuver, even with high thrusting forces, remains good. On top of that, the roll angle obtained has been reduced up to a factor 10 in the best case, and the hub motion, even in the worst case analysis, is smoother and presents lower oscillations that the best of the cases in Section 5. Last but, by no means, least, the sail's attitude has been observed not to vary (a difference of about 10% was recorded in the worst case considered) regardless of the difference in the bending stiffness, which differed one from the other by three orders of magnitude. That fact is specially important because, as it has kept being said in the document, it is not possible to determine the value of the bending stiffness on ground, so a control system capable of perform the same independently from such parameter is necessary in order to predict the motion of the sail once in operation. Increasing the weight of the tip-masses was seen to further improve the behaviour of the sail in all the considerations cited above.

7   Conclusion

In this document, the effects of the bending stiffness on the solar sail to be used for the mission OKEANOS during an attitude control method for changing its spin axis have been studied. The data obtained from the IKAROS mission revealed that its membrane presented a higher rigidity than predicted, leading to divergences with respect to the expected attitude of the sail. That, together with the fact that OKEANOS will have more devices on its membrane that would increase its stiffness, led to add a correction factor for the torsion spring constant present in the creases of the sail. Since the bending stiffness of the membrane remains as an unknown, that factor was made to vary during all the simulations up to a value with which its behavior was no longer seen as completely flexible, found for $K = 1 \times e - 2$.

In Section 4, the results for the reorientation by Rhumb-Line Maneuver done using the in-body thrusting system of the sail where presented. The pitch angle of the whole sail was indeed changed effectively after the simulation, although its performance was lower than what was expected theoretically. Also, the hub-membrane coupling led the nutation caused from the thrusting to diverge.

Regarding the bending stiffness, when varying the rigidity of the sail, attitude changes followed. It was observed that the higher the bending parameter, the better the performance of the sail. Analyzing the out-of-plane motion of the particles constituting the sail in the frequency domain, it could be seen that the improvement in performance resulted from the lowering of the vibrations arising as the rigidity increased. The vibration modes excited corresponded to the frequency of the input force, although some deviation existed between the flexible and more rigid sail models.

So as to avoid the instability introduced by the connection between the body of the spacecraft and the sail itself, a new control system is introduced in Section 5: tip-mass thrusting. After the simulations, it is found that, like it happens with conventional reaction control systems, the higher the force magnitude and the impulse time, the lower the stability of the system. Divergence, however, was not obtained anymore. Nonetheless, even for the less favorable of the cases, the performance obtained was better than the in-body thruster system considered until now. Despite that being a remarkable fact, what truly makes the difference between systems is the response of the sail depending of the bending stiffness parameter. Whereas in the in-body case such parameter determined greatly the maneuver performance, the tip-mass one permits undergoing an attitude maneuver with the same response from the sail regardless of it presenting a higher rigidity provided that the thrusting input is kept low. When increasing it, despite the inclination of the sail with respect to the inertial z-axis presents little variations, the Euler angles vary amongst the higher and lower bending cases because of the apparition of an undesired roll angle.

The application of the input forces directly over the membrane also allows a more detailed study on the vibrations depending on the bending stiffness. Difference frequencies are seen to be excited for different bending moments. For low rigidity cases, the frequencies described by the non-bending equation of motion hold, whereas when the sail turns rigid enough, the excited modes vary, getting excitation on higher order modes while skipping others. Higher circumferential mode excitation, together with stronger oscillations of the particles, diminish the efficacy of the reorientation maneuver.

Finally, in Section 6, the algorithm is improved by means of a roll control synchronized with the spin of the hub. The simulations done show the maneuver performance to meet the theoretical value even in the maximum thrusting case out of the ones considered, and both the roll angle and the nutation that in previous cases arose in the hub are kept close to zero. More importantly, with the newly implemented control the attitude of the sail does not vary with the rigidity. In addition, it is found that increasing the weight of the tip-masses improves the results obtained in a further way.

Since bending stiffness plays an important role in the sail dynamics, the inability to determine its value represents a threat for the OKEANOS mission, specially when performing operations that require of great precision, such as the release of the lander. The control presented in the last section of the document offers an axis reorientation system the performance of which does not depend anymore on the

stiffness of the sail.

As for the frequency analysis, a difference on the modes excited was found depending on the bending stiffness, so if such modes were measured it would be possible to determine the bending character of the membrane from them. Also, a relationship between the amplitude of the frequency and the performance on the maneuver can be established: the higher the amplitude and, therefore, the higher the vibrations, the lower the performance. As future work, a study on the natural frequencies and oscillation modes parting from the complete equation of motion of the sail should be developed thoroughly. Also, as a reduction on the vibrations has a direct repercussion on the performance of the reorientation maneuver, adding on membrane devices such as piezoelectric actuators for vibration reduction and control of the oscillation modes shall be considered.

References

[1] J. Kawaguchi et al. "Science and Exploration in the Solar Power Sail OKEANOS Mission to a Jupiter Trojan Asteroid," pp. 9–10, 2018.

[2] O. Mori, J. Matsumoto, T. Chujo, H. Kato, and T. Saiki, "Navigation to Jovian Trojan Asteroid using Solar Power Sail-craft and Underground Sampling using Lander," 2017.

[3] Y. Tsuda "An Attitude Control Strategy for Spinning Solar Sails," 2004.

[4] Y. Takao "Active Shape Control of Spinning Membrane Space Structures and its Application to Solar Sailing", 2018.

[5] T. Nakano, O. Mori and J. Kawaguchi, "Stability of Spinning Solar Sail-craft Containing a Huge Membrane," AIAA Guid., Navig. Control Conference, 2005.

[6] N. Okuizumi and T. Yamamoto, "Centrifugal Deployment of Membrane with Spiral Folding: Experiment and Simulation, " Journal of Space Engineering, Vol.2, No.1, pp.41-50, 2009.

[7] A. Muta, S. Matunaga and N. Okuizumi," High Vacuum Experiment of Spinning Deployment using Scaled-down Model for Solar Sail,"IAC-10-C2.5.4, 61st International Astronautical Congress, Prague, Czech Republic, 2010

[8] Kang, S. and Im, S., "Finite element analysis of dynamic response of wrinkling membranes," Computer Methods in Applied Mechanics and Engineering, Vol.173, pp.227-240, 1999.

[9] Miyazaki, Y. and Kodama, T., "Formulation and Interpretation of the Equation of Motion on the Basis of the Energy-Momentum Method," Journal of Multi-body Dynamics, Vol.218, pp.1-7, 2004.

[10] Miyazaki, Y., Sakamoto, H., Shirasawa, Y., Mori, O., Sawada, H., Yamazaki, M. and IKAROS Demonstration Team: Finite Element Analysis of Deployment of Sail Membrane of IKAROS, 28th International Symposium on Space Technology and Science, 2011, 2011-o-4-06v.

[11] Y. Tsuda "Improved Multi-Particle Model for Dynamics Analysis of Arbitrary-Shaped Thin Flexible Structure," 2004.

[12] Y. Shirasawa, O. Mori, H. Sawada, Y. Chishiki, K. Kitamura, and J. Kawaguchi, "A Study on Membrane Dynamics and Deformation of Solar Power Sail Demonstrator 'IKAROS,'" 53rd AIAA/ASME/ASCE/AHS/ASC Structures, Structural Dynamics Conference, pp. 1–11, 2012.

[13] N. Okuizumi and T. Yamamoto, "Centrifugal Deployment of Membrane with Spiral Folding: Experiment and Simulation, " Journal of Space Engineering, Vol.2, No.1, pp.41-50, 2009.

[14] A. Muta, S. Matunaga and N. Okuizumi," High Vacuum Experiment of Spinning Deployment using Scaled-down Model for Solar Sail,"IAC-10-C2.5.4, 61st International Astronautical Congress, Prague, Czech Republic, 2010

[15] O. Mori et al. "Adjusting the Membrane Model using the Multi-Particle Method via Vibration Experiments in a Vacuum Chamber," vol. 11, pp. 27–31, 2013.

[16] Y. Shirasawa, "Study on Motion Analysis of Large Space Film Surface Structure by using Multi Particle Method.", 2012.

[17] I. Ryota, Y. Morita, "Observation of Asymmetric Centrifuge Deployment of Space Membrane Structures by Using Multi Particle Method.", 2014.

[18] K. Shintaku, "Study on Film Surface Behavior of Spin Type Solar Sail," Tokyo Institute of Technology Master Thesis, 2013.

[19] M. Hasome, O. Mori et al. "Refining Membrane Model via Multi-Particle Method combined with Vibration Experiment in Vacuum Chamber.", 2013.

[20] Shirasawa, Y., Mori, O., Miyazaki, Y., Sakamoto, H., Hasome, M., Okuizumi, N., Sawada, H., Matunaga, S., Furuya, H. and Kawaguchi, J. : Evaluation of Membrane Dynamics of IKAROS Based on Flight Result and Simulation Using Multi-Particle Model, Aerospace Technology Japan, 2012.

[21] N. Okuizumi and T. Yamamoto, "Experiments and Simulations of Centrifugal Deployments of Membranes Stowed with Spiral Folding," 2009.

[22] J. C. Van Der Ha, "Models for Rhumb-Line Attitude Maneuvers and Error Propagation Effects," J. Guid. Control. Dyn., vol. 29, no. 6, pp. 1384–1394, 2006.

[23] R. Raus and Y. Gao, "Review and analysis of single-thruster attitude control techniques for spinning spacecraft," August 2015.

[24] N. Baddour, "A revisit of spinning disk models. Linear transverse vibrations," 2000.

[25] S. Timoshenko and J. N. Goodier, "Theory of Elasticity." McGraw-Hill Book Company, New York, 1951.

[26] H Lamb and R.V. Southwell, "The vibrations of a spinning disk." Proceedings of the Royal Society Of London, Series A, 99272-280. 1921.

[27] T. Chujo and J. Kawaguchi, "Evaluation of transient response of spinning solar sail with flexible membrane by eigenfunction analysis and continuum analysis," Acta Astronaut., vol. 127, pp. 542–552, 2016.

[28] R. Kato, "The Deployment Behavior Analysis of Solar Power Sail Using Multi-particle Method," 2018.

[29] N. Baddour, "A Modelling and Vibration Analysis of Spinning Disks," 2001.